A UNIFYING ALLOSTERIC ACTIVATION MODEL FOR cGAS ACTIVITY AND SIGNALING

by
Richard M. Hooy

A dissertation submitted to Johns Hopkins University in conformity with the requirements for the degree of Doctor of Philosophy.

Baltimore, Maryland
February 2019

Abstract

Human cyclic GMP-AMP synthase (cGAS) contributes to the cellular stress response by detecting cytosolic double-stranded (ds)DNA and initiating defensive signaling programs. dsDNA binding induces cGAS dimerization and activation, which enables it convert ATP and GTP into the second messenger, cyclic GMP-AMP (cGAMP). cGAMP binds the downstream signaling adaptor Stimulator of Interferon Genes (STING) which triggers upregulation of stress response genes. cGAS/STING signaling results in variable cellular outcomes depending on cell type, dsDNA stimulus, signal strength and the duration for which the signaling axis is active. Moreover, dysregulated cGAS/STING signaling contributes to disease. Thus, understanding how cGAS activity is regulated is key to determining how cellular stress dictates cell fate and organismal health.

Although cGAS can be activated by any length of dsDNA *in vitro*, cGAS discriminates against short dsDNAs in cells. This discrepancy is thought to arise from dsDNA-length dependent binding and is predicated on the notion that cGAS forms ladder-like arrays on parallel strands of DNA duplexes. Although cGAS binding affinity is dependent on dsDNA length, the 'ladder' model fails to explain why short dsDNA activates cGAS *in vitro.* Moreover, the model disregards any role that substrate may play in the allosteric activation mechanism, nor how cGAS concentration affects dsDNA-length dependent activities. For these reasons, I used recombinant, human cGAS protein and *in vitro* biochemical and biophysical tools to develop a comprehensive model that explains how cGAS activity is regulated. The model defines how substrate binding, cGAS self-association and dsDNA binding are thermodynamically linked to cGAS activity and provides a rationale for why dsDNA length discretion is context-dependent. The full-length enzyme operates within the same allosteric network as the catalytic domain alone, with the exception that the N-terminal domain assists in cGAS auto- and ligand-induced dimerization. Finally, using the model as a guide, I determined how divalent manganese contributes to cGAS dsDNA sensing.

The model defines how cGAS is intrinsically regulated and provides a rationale for how inflammation potentiates cGAS's role in autoimmunity. Moreover, the model serves as a platform to delineate how extrinsic factors, such as post-translation modifications, affect cGAS activity.

Advisor: Dr. Jungsan Sohn

Reader: Dr. Scott Bailey

Acknowledgements

First and foremost, I would like to thank my parents, Bob and Sue Hooy. Their encouragement and support made me the successful, happy and fulfilled person that I am today.

I owe my success as a scientist to many tremendous mentors.

Dr. Gregory Weiss, at UC Irvine, gave me the opportunity as an undergraduate to discover the excitement of research. In his lab, I was taught by one of the most patient and nurturing mentors, Dr. Rosemarie Vithayathil. She not only showed me how to do research, but how to effectively teach someone in the process.

My Ph.D. mentor, Dr. Jungsan Sohn, has told me on multiple occasions that he sees many of the same qualities in me as he saw in himself at my age. Such are the things that motivate me to continue my pursuit of independent research. J and I grew as scientists during my time in his lab. We experienced hardship and frustration, but also pure excitement and success. He trained me to think and write like a scientist and taught me to value scientific rigor. Such are the things that will make me successful. Such are the things that I will never forget, nor will I hesitate to disseminate this philosophy unto others. I could not have asked for a better Ph.D. mentor.

Thanks to my lab mates. Mariusz was gracious enough to perform most of the negative-stain electron microscopy experiments, Dr. Seamus Morrone mentored me during my first few years in the lab, and Zach Mazanek lent a hand when needed. Thanks for all of the discussions.

I would like to thank my friends and family. Thank you for your undying support.

Last, but not least, I would like to thank Hannah Little. With your love, I can do anything. Thank you.

Table of Contents

Chapter 1

Introduction

Stress

To survive and prosper, cells must accomplish three main objectives: acquire nutrients, replicate and respond appropriately to stress. Nutrients supply the energy for cellular activities, while replication ensures continuation of the cell's lineage. Why then, is stress so important? Broadly defined, stress is anything that perturbs cellular homeostasis, and as such, impinges on a cell's life constantly. Cells are in perpetual pursuit of maintaining homeostasis. As a result, stress significantly contributes to the decision of when to divide and how to use energy.

Cellular stress comes in many forms. Direct, physical contact can damage essential protective barriers, such as the cell wall, or any compartment that sequesters molecules to specific locales. Cells also experience perturbations in temperature and pressure, which inherently tests the fortitude and resilience of biological macromolecules and cellular sub- and super-structures. At the chemical level, cells are challenged on a regular basis by bouts of nutrient starvation, radiation, and microbial attacks, and, error in cellular processes like replication and protein folding can lead to serious issues. In all such cases, the cell can detect events that perturb homeostasis and enact a programmed response that leads to resolution.

The immune system exemplifies stress detection and resolution. When a pathogen is detected, cells not only produce pro-inflammatory molecules that recruit immune cells to this site of stress, but they also produce anti-viral effectors that can either detect pathogens or directly inhibit them. Immune cell activation also coordinates maturation of the adaptive immune response of which prepares the entire organism for repeat stress offenses. Importantly, this concerted response hinges on accurate perception of stress by molecular sentinels of the innate immune system. These Pattern

Recognition Receptor, PRRs, are a sub-set of structurally and functionally diverse, germline-encoded proteins and enzymes, that share the common goal of identifying molecules associated with stress and then initiating appropriate stress responses.

Knowing the difference between self and nonself

Distinguishing normal, host molecules (self) from particles contributed by 'outside' sources (non-self; stress) is paramount to initiating the correct stress response. Phenomenologically, non-self can be defined in several ways. First, molecules can be chemically distinct from those typically created by the host cell. The bacterial cell wall is composed of many orthogonal compounds, such as peptidoglycan and lipopolysaccharide, that are readily detected by PRRs. Non-self can also be synthesized by the host. During replication, RNA viruses recruit polymerases that duplicate the viral genome, and in so doing, create 5'-termini baring a triphosphate moiety; RNA molecules synthesized by the host are modified to remove this key molecular signature. Host-derived proteins can also constitute non-self if the proteins encode non-host sequences, folds or activities such as virulence factors. Proteins that are modified by microbes or the host itself as a result of infection can create molecular signatures, unique to stressful events. Lastly, mislocalization of native chemicals is also a signature of non-self. Genomic, host DNA can escape the nucleus and mitochondria as a result of DNA damage or infection, which triggers PRRs to initiate inflammatory responses. Of the many stress signatures, nonself nucleic acids are arguably the trickiest to sense, given the abundance of host nucleic acids in the cell.

The immunostimulatory nature of nucleic acids

The primary role of DNA is to store genetic information, while RNA is generally considered to be a conduit for translating the genetic code into protein. DNA is typically double-stranded and restricted to the nucleus and mitochondria, while RNA is present in the nucleus and cytosol as single-stranded segments. Despite their ubiquitous presence and conserved roles in information storage and propagation, DNA and RNA have long been known to stimulate the immune system when introduced into eukaryotic cells (Stetson and Medzhitov 2006; Yan and Chen 2012; Gantier and Williams 2007). Forced entry of dsDNA and dsRNA into mammalian cells results in a burst of pro-inflammatory molecules, including type-I interferons, the primary drivers of antiviral immunity. Considerable progress has been made to not only determine which proteins are involved in this innate immune response, but also what molecular signatures each sensor detects.

Sources of cytosolic dsDNA

Cytosolic dsDNA is an obvious danger signal. Viruses, microbes and tumor cells are the primary source of *exogenous* dsDNA (Xu et al. 2017; Ablasser and Gulen 2016). The cell's own dsDNA can also be a source of danger signal. While the cell is careful to sequester dsDNA within the nucleus and mitochondria to keep it protected and localized, DNA damage (Hartlova et al. 2015), genome instability (Mackenzie et al. 2017; Harding et al. 2017), and organelle failure (West et al. 2015; Yuan et al. 2017) can introduce host dsDNA into the cytosol.

Regulatory strategies used by cytosolic dsDNA sensors

Stress sensor activation is regulated primarily by two main processes: templated-oligomerization and/or allosteric regulation of enzymatic activity. The two main classes of cytosolic dsDNA sensors exemplify these strategies.

Aim2-like receptors, ALRs. Prototypical ALR family members are composed of an N-terminal pyrin death domain (PYD), a central linker, and a C-terminal HIN domain(s) (HIN: hematopoietic interferon-inducible nuclear protein with a 200 amino acid repeat). Activation is achieved by dsDNA-templated oligomerization. The HIN domains associate with dsDNA in a sequence-independent manner. Proximal binding of multiple ALRs increases the probability of PYD ring formation (nucleation) and subsequent oligomerization (Morrone et al. 2015; Matyszewski, Morrone, and Sohn 2018). The PYD oligomer then seeds oligomerization of the downstream signaling adaptor protein (Fernandes-Alnemri et al. 2009; Hornung et al. 2009). This strategy creates a filtering mechanism dictated by dsDNA length that can be demonstrated both in vitro and in cells. dsDNA length-dependence ensures that ALR activation is only achieved under conditions of stress, such as during viral or microbial infection which can coincide with the presence of long genomic dsDNA.

Cyclic GMP-AMP synthase, cGAS. cGAS is a nucleotidyl transferase (NTase) that couples ligand binding to catalytic activity (Sun et al. 2013). Upon dsDNA binding, cGAS produces a cyclic dinucleotide, cyclic GMP-AMP (GAMP), from ATP and GTP, which serves as a second messenger in its stress signaling pathway. cGAMP is unique from the products of other NTases, like polymerases and oligoadenylate synthase (OAS), in that it is cyclized and has mixed phosphodiester linkages, 2'-GMP-5'-AMP and 3'-AMP-5'-GMP (Ablasser et al. 2013; Diner et al. 2013; Zhang et al. 2013). cGAS activity also relies on templated, self-association, although the mechanism for how this contributes to self vs nonself discrimination has evolved considerably over the past several years.

Allostery and dsDNA length-dependent activation of cGAS

Regulation of cGAS enzymatic activity at the individual protein level is shared between cGAS and its close, dsRNA sensing relative, OAS; double-stranded nucleic acids allosterically promote conformational changes that stabilize the active, catalytic state. Multiple, atomic-resolution structures of cGAS revealed how dsDNA potentiates catalysis. Key conformational changes are observed upon dsDNA binding. At the dsDNA binding site, the so-called "spine helix" alters is structure, resulting in an elongated, contiguous helix. dsDNA binding also appears to force a short stretch of amino acids near the active site, the activation loop, to become ordered as a mean to reduce steric clash with the bound dsDNA. Both conformational changes are responsible for properly orienting acidic residues within the active site that align divalent cations for the catalysis of nucleotidyl transfer (Kato et al. 2013; Civril et al. 2013; Kranzusch et al. 2013; Shu, Li, and Li 2014; Zhou et al. 2018).

Although, in principle, monomeric cGAS should be sufficient for dsDNA-induced activity, self-association is critical for cGAS activity. Evidence for this first came from crystal structures of cGAS. Of the 38 structures solved of mouse, pig and human cGAS, all have captured cGAS in the dimeric state, regardless of bound ligands. Importantly, this was far from crystallographic artifact. Mutational studies showed that dsDNA binding affinity and activity were severely compromised if dimerization was impeded, and that the cGAS-mediated immune response was virtually incapacitated for dimerization-null mutants (Li et al. 2013; Zhang et al. 2014). Again, structures of cGAS bound to dsDNA hinted at the reason. cGAS forms a 2:2 complex with short dsDNA (2 cGAS molecules per 2 molecules of dsDNA) within the crystal lattice. Biophysical characterization of mouse cGAS in solution determined that mouse cGAS has minimal auto-dimerization capacity ($K_{dimer} >> 100\mu M$), but dsDNA can drive dimerization in a dsDNA length- and sequence-independent manner, providing the causal link between cGAS dimerization and activity.

However, recent literature contests the idea that dsDNA length is not important for cGAS signaling. Two, independent groups discovered that cGAS activity is dsDNA length-dependent in cells and in vitro (Andreeva et al. 2017; Luecke et al. 2017b). A structure of mouse cGAS bound to longer dsDNA (39 base-pair) indicated that cGAS dimers could propagate along parallel duplexes like rungs on a ladder (Andreeva et al. 2017). The authors provided evidence to suggest that dsDNA length dictated the probability of cGAS dimerization and ladder formation. The implications of this were that cGAS (functional) binding affinity would be cooperative and dsDNA length-dependent, which the authors showed by ITC and a new activity assay. Moreover, because dimerization was known to be required for activity, laddering could explain why dsDNA length correlated with cGAS activity. Although the model revealed important relationships between dsDNA length, binding affinity and cGAS activity, it fell short of accurately explaining how dsDNA length-dependence could be context specific. A more-sound, biophysical and biochemical approach would be required to better understand the allosteric nature of cGAS activation (see chapter 3).

Pleiotropic outcomes from cGAS activation

In 2013, cyclic GMP-AMP synthase (cGAS) was identified to be the major initiator of anti-viral and pro-inflammatory signaling in response to cytosolic DNA (Sun et al. 2013). This, and multiple studies thereafter, led to the aggregate conclusion that cGAS plays an essential, protective role during infection by DNA viruses, some RNA viruses, and many species of bacteria (Watson et al. 2015; Collins et al. 2015; Gao, Wu, et al. 2013; Hansen et al. 2014; Lam and Falck-Pedersen 2014). Subsequent studies also identified that cGAS contributes to stress responses spurred by DNA damage (Li and Chen 2018), missegregation of chromosomal DNA during cell division (Mackenzie et al. 2017; Harding et al. 2017), and mitochondrial malfunction (West et al. 2015; Sun et al. 2017; West and Shadel 2017). Thus, cGAS signaling broadly impacts numerous cellular processes.

Conventionally, cGAS signals through stimulator of interferon genes (STING), a resident ER transmembrane protein (Ablasser et al. 2013; Diner et al. 2013; Zhang et al. 2013). cGAMP binding to STING promotes conformational changes within the dimeric, cytosol-facing domain, enacting the recruitment of kinases and other factors that lead to transcriptional activation and synthesis of pro-inflammatory molecules including chemokines and type-I interferons (IFN-I) via transcription factors interferon regulatory factor 3 (IRF3) and NFκB (Abe et al. 2013; Stetson and Medzhitov 2006; van Boxel-Dezaire, Rani, and Stark 2006; Ishikawa, Ma, and Barber 2009). IFN-Is are potent inducers of the anti-viral stress response and signal in an autocrine and paracrine fashion. Chemokines recruit immune cells to the site of cellular stress. The immune cells mitigate the spread of stress to other cells and prime T- and B-cells of the adaptive immune system for activation. This link between innate immunity (cGAS/STING) and adaptive immunity (T-cell activation) is of considerable importance. A hallmark of cancer cells is increased genomic instability and DNA damage. These processes produce cytosolic dsDNA that cGAS can detect (Zhang et al. 2015; Li et al. 2016; Mackenzie et al. 2017; Wang, Hu, et al. 2017; Li and Chen

2018). However, some tumors down-regulate cGAS signaling (Wu et al. 2017), which is thought to enable these malignant cells to avoid detection by mature immune cells.

Although cGAS activity is intrinsically controlled by dsDNA length, the consequence of its signaling can vary dramatically. This is in part due to the pleiotropic effects of IRF3/NFκB activation and IFN-I signaling. Unlike the dsDNA sensing pathway of AIM2 which results in interleukin production and pyroptotic cell death (Fernandes-Alnemri et al. 2009; Hornung et al. 2009), a binary process, cGAS signaling can lead to outcomes that vary from autophagy (Watson et al. 2015; Prabakaran et al. 2018; Lei et al. 2018), anti-viral states (Sun et al. 2013), senescence (Gluck et al. 2017; Yang et al. 2017; Li and Chen 2018) and cell death (Gulen et al. 2017; Gaidt et al. 2017; Brault et al. 2018). The cellular response is correlated with cell-type, and the amount and time-for-which cGAMP presides in the cell (Gulen et al. 2017). Hence, prolonged activity due to slow clearance of dsDNA (Ablasser et al. 2014; Gregg, Sarkar, and Shoemaker 2018), inadequate degradation of cGAMP (Li et al. 2014), or lack of feedback regulation on cGAS or STING can dramatically affect the outcome of stress (Chen, Sun, and Chen 2016; Luo and Shu 2018). The implications of this are best exemplified by auto-immune diseases, whereby sustained levels of pro-inflammatory molecules hyper-sensitize the innate and adaptive immune system, leading to dysregulated activity of the host’s immune system against its own tissues (Ablasser and Gulen 2016; Li, Wilson, and Kiss-Toth 2017).

The goal of this thesis work was to establish a unifying allosteric activation model for cGAS. The model should describe how dsDNA length dictates cGAS activity levels, why dsDNA length-dependence can vary with reaction context, and how cGAS signaling is attenuated. The model should also provide a robust framework for testing and understanding how extrinsic factors such as post-translational modifications, metals, co-sensors, inhibitors and other nucleic acids affect cGAS activity. Lastly, the model should inform observations made from cells and organisms and make predictions about how cGAS activity contributes to cell fate decisions and disease.

The project began with, and would not have been possible without, the implementation of a novel cGAS activity assay that monitors the production of byproduct during cGAS catalysis (Chapter 2). Using this activity assay, in tandem with numerous biophysical techniques, I revealed the coupled relationships between cGAS activity, its oligomeric state and its allosteric regulators, ATP/GTP and dsDNA (Chapter 3). Using the allosteric model as a guide, I began to unravel the unique and surprising ways in which manganese affects cGAS activity (Chapter 4). Findings from this work contribute broadly to our understanding of allostery, enzyme-mediated catalysis, protein self-association, stress sensing, signal transduction, cancer and (auto)immunity.

References

Abe, T., A. Harashima, T. Xia, H. Konno, K. Konno, A. Morales, J. Ahn, D. Gutman, and G. N. Barber. 2013. 'STING recognition of cytoplasmic DNA instigates cellular defense', *Mol Cell*, 50: 5-15.

Ablasser, A., M. Goldeck, T. Cavlar, T. Deimling, G. Witte, I. Rohl, K. P. Hopfner, J. Ludwig, and V. Hornung. 2013. 'cGAS produces a 2'-5'-linked cyclic dinucleotide second messenger that activates STING', *Nature*, 498: 380-4.

Ablasser, A., and M. F. Gulen. 2016. 'The role of cGAS in innate immunity and beyond', *J Mol Med (Berl)*, 94: 1085-93.

Ablasser, A., I. Hemmerling, J. L. Schmid-Burgk, R. Behrendt, A. Roers, and V. Hornung. 2014. 'TREX1 deficiency triggers cell-autonomous immunity in a cGAS-dependent manner', *J Immunol*, 192: 5993-7.

Andreeva, L., B. Hiller, D. Kostrewa, C. Lassig, C. C. de Oliveira Mann, D. Jan Drexler, A. Maiser, M. Gaidt, H. Leonhardt, V. Hornung, and K. P. Hopfner. 2017. 'cGAS senses long and HMGB/TFAM-bound U-turn DNA by forming protein-DNA ladders', *Nature*, 549: 394-98.

Brault, M., T. M. Olsen, J. Martinez, D. B. Stetson, and A. Oberst. 2018. 'Intracellular Nucleic Acid Sensing Triggers Necroptosis through Synergistic Type I IFN and TNF Signaling', *J Immunol*, 200: 2748-56.

Chen, Q., L. Sun, and Z. J. Chen. 2016. 'Regulation and function of the cGAS-STING pathway of cytosolic DNA sensing', *Nat Immunol*, 17: 1142-9.

Civril, F., T. Deimling, C. C. de Oliveira Mann, A. Ablasser, M. Moldt, G. Witte, V. Hornung, and K. P. Hopfner. 2013. 'Structural mechanism of cytosolic DNA sensing by cGAS', *Nature*, 498: 332-7.

Collins, A. C., H. Cai, T. Li, L. H. Franco, X. D. Li, V. R. Nair, C. R. Scharn, C. E. Stamm, B. Levine, Z. J. Chen, and M. U. Shiloh. 2015. 'Cyclic GMP-AMP Synthase Is an Innate Immune DNA Sensor for Mycobacterium tuberculosis', *Cell Host Microbe*, 17: 820-8.

Diner, E. J., D. L. Burdette, S. C. Wilson, K. M. Monroe, C. A. Kellenberger, M. Hyodo, Y. Hayakawa, M. C. Hammond, and R. E. Vance. 2013. 'The innate immune DNA sensor cGAS produces a noncanonical cyclic dinucleotide that activates human STING', *Cell Rep*, 3: 1355-61.

Fernandes-Alnemri, T., J. W. Yu, P. Datta, J. Wu, and E. S. Alnemri. 2009. 'AIM2 activates the inflammasome and cell death in response to cytoplasmic DNA', *Nature*, 458: 509-13.

Gaidt, M. M., T. S. Ebert, D. Chauhan, K. Ramshorn, F. Pinci, S. Zuber, F. O'Duill, J. L. Schmid-Burgk, F. Hoss, R. Buhmann, G. Wittmann, E. Latz, M. Subklewe, and V. Hornung. 2017. 'The DNA Inflammasome in Human Myeloid Cells Is Initiated by a STING-Cell Death Program Upstream of NLRP3', *Cell*, 171: 1110-24 e18.

Gantier, M. P., and B. R. Williams. 2007. 'The response of mammalian cells to double-stranded RNA', *Cytokine Growth Factor Rev*, 18: 363-71.

Gao, D., J. Wu, Y. T. Wu, F. Du, C. Aroh, N. Yan, L. Sun, and Z. J. Chen. 2013. 'Cyclic GMP-AMP synthase is an innate immune sensor of HIV and other retroviruses', *Science*, 341: 903-6.

Gluck, S., B. Guey, M. F. Gulen, K. Wolter, T. W. Kang, N. A. Schmacke, A. Bridgeman, J. Rehwinkel, L. Zender, and A. Ablasser. 2017. 'Innate immune sensing of cytosolic chromatin fragments through cGAS promotes senescence', *Nat Cell Biol*, 19: 1061-70.

Gregg, R. W., S. N. Sarkar, and J. E. Shoemaker. 2018. 'Mathematical modeling of the cGAS pathway reveals robustness of DNA sensing to TREX1 feedback', *J Theor Biol*, 462: 148-57.

Gulen, M. F., U. Koch, S. M. Haag, F. Schuler, L. Apetoh, A. Villunger, F. Radtke, and A. Ablasser. 2017. 'Signalling strength determines proapoptotic functions of STING', *Nat Commun*, 8: 427.

Hansen, K., T. Prabakaran, A. Laustsen, S. E. Jorgensen, S. H. Rahbaek, S. B. Jensen, R. Nielsen, J. H. Leber, T. Decker, K. A. Horan, M. R. Jakobsen, and S. R. Paludan. 2014. 'Listeria monocytogenes induces IFNbeta expression through an IFI16-, cGAS- and STING-dependent pathway', *EMBO J*, 33: 1654-66.

Harding, S. M., J. L. Benci, J. Irianto, D. E. Discher, A. J. Minn, and R. A. Greenberg. 2017. 'Mitotic progression following DNA damage enables pattern recognition within micronuclei', *Nature*, 548: 466-70.

Hartlova, A., S. F. Erttmann, F. A. Raffi, A. M. Schmalz, U. Resch, S. Anugula, S. Lienenklaus, L. M. Nilsson, A. Kroger, J. A. Nilsson, T. Ek, S. Weiss, and N. O. Gekara. 2015. 'DNA damage primes the type I interferon system via the cytosolic DNA sensor STING to promote anti-microbial innate immunity', *Immunity*, 42: 332-43.

Hornung, V., A. Ablasser, M. Charrel-Dennis, F. Bauernfeind, G. Horvath, D. R. Caffrey, E. Latz, and K. A. Fitzgerald. 2009. 'AIM2 recognizes cytosolic dsDNA and forms a caspase-1-activating inflammasome with ASC', *Nature*, 458: 514-8.

Ishikawa, H., Z. Ma, and G. N. Barber. 2009. 'STING regulates intracellular DNA-mediated, type I interferon-dependent innate immunity', *Nature*, 461: 788-92.

Kato, K., R. Ishii, E. Goto, R. Ishitani, F. Tokunaga, and O. Nureki. 2013. 'Structural and functional analyses of DNA-sensing and immune activation by human cGAS', *PLoS One*, 8: e76983.

Kranzusch, P. J., A. S. Lee, J. M. Berger, and J. A. Doudna. 2013. 'Structure of human cGAS reveals a conserved family of second-messenger enzymes in innate immunity', *Cell Rep*, 3: 1362-8.

Lam, E., and E. Falck-Pedersen. 2014. 'Unabated adenovirus replication following activation of the cGAS/STING-dependent antiviral response in human cells', *J Virol*, 88: 14426-39.

Lei, Z., M. Deng, Z. Yi, Q. Sun, R. A. Shapiro, H. Xu, T. Li, P. A. Loughran, J. E. Griepentrog, H. Huang, M. J. Scott, F. Huang, and T. R. Billiar. 2018. 'cGAS-mediated autophagy protects the liver from ischemia-reperfusion injury independently of STING', *Am J Physiol Gastrointest Liver Physiol*, 314: G655-G67.

Li, L., Q. Yin, P. Kuss, Z. Maliga, J. L. Millan, H. Wu, and T. J. Mitchison. 2014. 'Hydrolysis of 2'3'-cGAMP by ENPP1 and design of nonhydrolyzable analogs', *Nat Chem Biol*, 10: 1043-8.

Li, T., and Z. J. Chen. 2018. 'The cGAS-cGAMP-STING pathway connects DNA damage to inflammation, senescence, and cancer', *J Exp Med*, 215: 1287-99.

Li, T., H. Cheng, H. Yuan, Q. Xu, C. Shu, Y. Zhang, P. Xu, J. Tan, Y. Rui, P. Li, and X. Tan. 2016. 'Antitumor Activity of cGAMP via Stimulation of cGAS-cGAMP-STING-IRF3 Mediated Innate Immune Response', *Sci Rep*, 6: 19049.

Li, X., C. Shu, G. Yi, C. T. Chaton, C. L. Shelton, J. Diao, X. Zuo, C. C. Kao, A. B. Herr, and P. Li. 2013. 'Cyclic GMP-AMP synthase is activated by double-stranded DNA-induced oligomerization', *Immunity*, 39: 1019-31.

Li, Y., H. L. Wilson, and E. Kiss-Toth. 2017. 'Regulating STING in health and disease', *J Inflamm (Lond)*, 14: 11.

Luecke, S., A. Holleufer, M. H. Christensen, K. L. Jonsson, G. A. Boni, L. K. Sorensen, M. Johannsen, M. R. Jakobsen, R. Hartmann, and S. R. Paludan. 2017. 'cGAS is activated by DNA in a length-dependent manner', *EMBO Rep*, 18: 1707-15.

Luo, W. W., and H. B. Shu. 2018. 'Delicate regulation of the cGAS-MITA-mediated innate immune response', *Cell Mol Immunol*, 15: 666-75.

Mackenzie, K. J., P. Carroll, C. A. Martin, O. Murina, A. Fluteau, D. J. Simpson, N. Olova, H. Sutcliffe, J. K. Rainger, A. Leitch, R. T. Osborn, A. P. Wheeler, M. Nowotny, N. Gilbert, T. Chandra, M. A. M. Reijns, and A. P. Jackson. 2017. 'cGAS surveillance of micronuclei links genome instability to innate immunity', *Nature*, 548: 461-65.

Matyszewski, M., S. R. Morrone, and J. Sohn. 2018. 'Digital signaling network drives the assembly of the AIM2-ASC inflammasome', *Proc Natl Acad Sci U S A*.

Morrone, S. R., M. Matyszewski, X. Yu, M. Delannoy, E. H. Egelman, and J. Sohn. 2015. 'Assembly-driven activation of the AIM2 foreign-dsDNA sensor provides a polymerization template for downstream ASC', *Nat Commun*, 6: 7827.

Prabakaran, T., C. Bodda, C. Krapp, B. C. Zhang, M. H. Christensen, C. Sun, L. Reinert, Y. Cai, S. B. Jensen, M. K. Skouboe, J. R. Nyengaard, C. B. Thompson, R. J. Lebbink, G. C. Sen, G. van Loo, R. Nielsen, M. Komatsu, L. N. Nejsum, M. R. Jakobsen, M. Gyrd-Hansen, and S. R. Paludan. 2018. 'Attenuation of cGAS-STING signaling is mediated by a p62/SQSTM1-dependent autophagy pathway activated by TBK1', *EMBO J*, 37.

Shu, C., X. Li, and P. Li. 2014. 'The mechanism of double-stranded DNA sensing through the cGAS-STING pathway', *Cytokine Growth Factor Rev*, 25: 641-8.

Stetson, D. B., and R. Medzhitov. 2006. 'Recognition of cytosolic DNA activates an IRF3-dependent innate immune response', *Immunity*, 24: 93-103.

Sun, B., K. B. Sundstrom, J. J. Chew, P. Bist, E. S. Gan, H. C. Tan, K. C. Goh, T. Chawla, C. K. Tang, and E. E. Ooi. 2017. 'Dengue virus activates cGAS through the release of mitochondrial DNA', *Sci Rep*, 7: 3594.

Sun, L., J. Wu, F. Du, X. Chen, and Z. J. Chen. 2013. 'Cyclic GMP-AMP synthase is a cytosolic DNA sensor that activates the type I interferon pathway', *Science*, 339: 786-91.

van Boxel-Dezaire, A. H., M. R. Rani, and G. R. Stark. 2006. 'Complex modulation of cell type-specific signaling in response to type I interferons', *Immunity*, 25: 361-72.

Wang, H., S. Hu, X. Chen, H. Shi, C. Chen, L. Sun, and Z. J. Chen. 2017. 'cGAS is essential for the antitumor effect of immune checkpoint blockade', *Proc Natl Acad Sci U S A*, 114: 1637-42.

Watson, R. O., S. L. Bell, D. A. MacDuff, J. M. Kimmey, E. J. Diner, J. Olivas, R. E. Vance, C. L. Stallings, H. W. Virgin, and J. S. Cox. 2015. 'The Cytosolic Sensor cGAS Detects Mycobacterium tuberculosis DNA to Induce Type I Interferons and Activate Autophagy', *Cell Host Microbe*, 17: 811-19.

West, A. P., W. Khoury-Hanold, M. Staron, M. C. Tal, C. M. Pineda, S. M. Lang, M. Bestwick, B. A. Duguay, N. Raimundo, D. A. MacDuff, S. M. Kaech, J. R. Smiley, R. E. Means, A. Iwasaki, and G. S. Shadel. 2015. 'Mitochondrial DNA stress primes the antiviral innate immune response', *Nature*, 520: 553-7.

West, A. P., and G. S. Shadel. 2017. 'Mitochondrial DNA in innate immune responses and inflammatory pathology', *Nat Rev Immunol*, 17: 363-75.

Wu, M. Z., W. C. Cheng, S. F. Chen, S. Nieh, C. O'Connor, C. L. Liu, W. W. Tsai, C. J. Wu, L. Martin, Y. S. Lin, K. J. Wu, L. F. Lu, and J. C. Izpisua Belmonte. 2017. 'miR-25/93 mediates hypoxia-induced immunosuppression by repressing cGAS', *Nat Cell Biol*, 19: 1286-96.

Xu, M. M., Y. Pu, D. Han, Y. Shi, X. Cao, H. Liang, X. Chen, X. D. Li, L. Deng, Z. J. Chen, R. R. Weichselbaum, and Y. X. Fu. 2017. 'Dendritic Cells but Not Macrophages Sense Tumor Mitochondrial DNA for Cross-priming through Signal Regulatory Protein alpha Signaling', *Immunity*, 47: 363-73 e5.

Yan, N., and Z. J. Chen. 2012. 'Intrinsic antiviral immunity', *Nat Immunol*, 13: 214-22.

Yang, H., H. Wang, J. Ren, Q. Chen, and Z. J. Chen. 2017. 'cGAS is essential for cellular senescence', *Proc Natl Acad Sci U S A*, 114: E4612-E20.

Yuan, L., Y. Mao, W. Luo, W. Wu, H. Xu, X. L. Wang, and Y. H. Shen. 2017. 'Palmitic acid dysregulates the Hippo-YAP pathway and inhibits angiogenesis by inducing mitochondrial damage and activating the cytosolic DNA sensor cGAS-STING-IRF3 signaling mechanism', *J Biol Chem*, 292: 15002-15.

Zhang, H., K. Tang, Y. Zhang, R. Ma, J. Ma, Y. Li, S. Luo, X. Liang, T. Ji, Z. Gu, J. Lu, W. He, X. Cao, Y. Wan, and B. Huang. 2015. 'Cell-free tumor microparticle vaccines stimulate dendritic cells via cGAS/STING signaling', *Cancer Immunol Res*, 3: 196-205.

Zhang, X., H. Shi, J. Wu, X. Zhang, L. Sun, C. Chen, and Z. J. Chen. 2013. 'Cyclic GMP-AMP containing mixed phosphodiester linkages is an endogenous high-affinity ligand for STING', *Mol Cell*, 51: 226-35.

Zhang, X., J. Wu, F. Du, H. Xu, L. Sun, Z. Chen, C. A. Brautigam, X. Zhang, and Z. J. Chen. 2014. 'The cytosolic DNA sensor cGAS forms an oligomeric complex with DNA and undergoes switch-like conformational changes in the activation loop', *Cell Rep*, 6: 421-30.

Zhou, W., A. T. Whiteley, C. C. de Oliveira Mann, B. R. Morehouse, R. P. Nowak, E. S. Fischer, N. S. Gray, J. J. Mekalanos, and P. J. Kranzusch. 2018. 'Structure of the Human cGAS-DNA Complex Reveals Enhanced Control of Immune Surveillance', *Cell*, 174: 300-11 e11.

Chapter 2

A pyrophosphatase-coupled assay to monitor the NTase activity of cGAS

Introduction

Cyclic GMP-AMP synthase (cGAS), a pattern recognition receptor of the innate immune system, induces the expression of type-I interferon (IFN-I) genes by binding cytosolic double-stranded (ds)DNA and synthesizing the unique second messenger, cyclic GMP-AMP (cGAMP), from ATP and GTP (Sun et al. 2013). cGAMP binds and activates stimulator of interferon genes (STING) (Ablasser et al. 2013; Zhang et al. 2013; Gao, Ascano, et al. 2013), which recruits and activates Tank-binding kinase 1 (TBK1) leading to activation of transcription factors, IRF3 and NF-□B (Ishikawa, Ma, and Barber 2009). The IFN-I response has variable outcomes and depends heavily on the strength of cGAS signaling (Vanpouille-Box et al. 2018; Li and Chen 2018; Gulen et al. 2017). Hence, knowing how cGAS activity is regulated at the molecular level, has the potential to inform observations made at the cell, tissue and organism level.

Numerous methods have been developed to track cGAS activity (Bose et al. 2016; Vincent et al. 2017; Hall, Brault, et al. 2017; Wang, Sooreshjani, et al. 2018; Ablasser et al. 2013; Liu et al. 2017; Andreeva et al. 2017). Most methods rely on the ability to directly measure cGAMP, the biological signaling molecule. However, in theory, an equally reliable proxy for nucleotidyl transferase (NTase) activity is the production of pyrophosphate, the by-product of cGAMP synthesis. Indeed, pyrophosphate detection has been employed to study numerous systems including NTases (Lloyd et al. 1995; Chang et al. 1984; Cestari and Stuart 2013; Seamon and Stivers 2015; Yi et al. 2011; McMillan, Hepowit, and Maupin-Furlow 2016). Pyrophosphate, itself, is seldom measured directly, rather its degradation product, inorganic phosphate, is quantified. Pyrophosphate is relatively stable under physiological conditions, but its degradation into inorganic phosphate is accelerated under low pH, by divalent cations and/or by enzymes that specifically catalyze the hydrolysis of pyrophosphates, e.g. pyrophosphatases (Stockbridge and Wolfenden 2011). Enzyme-mediated hydrolysis of pyrophosphate is far superior to chemical alternatives as evidenced by the 10^6-fold faster hydrolysis rate produced by pyrophosphatases. The high efficiency of pyrophosphatases is particularly critical for ensuring accurate rate measurement of target enzymes.

The specific measurement of cGAS NTase activity employs the coupled hydrolysis of pyrophosphate by *E.* coli pyrophosphatase (Figure 1A). Reactions are quenched with divalent cation chelators, such as EDTA, and the phosphate concentration is determined colorimetrically by measuring the absorbance of malachite green- phosphomolybdate complexes (Baykov, Evtushenko, and Avaeva 1988). Absolute values of phosphate are determined by comparing enzyme reactions to an internal, inorganic phosphate standard curve. This strategy has multiple advantages over direct detection of cGAMP. Phosphate detection is relatively cheap and relies mainly on a plate reader equipped with a UV-vis detector. The assay is also essentially label-free, which relieves restrictions on substrate concentration and substrate identity, and is scalable for high-throughput applications (Cestari and Stuart 2013; Seamon and Stivers 2015). Importantly, the assay lends itself to conventional steady-state enzymatic measurements with minimal hindrances, enabling accurate and rigorous measurement of cGAS enzymatic properties. Lastly, given the relatively slow turnover of cGAS (Vincent et al. 2017; Zhou et al. 2018), phosphate detection provides the benefit of immediate signal amplification per turnover event due to two phosphates being produced per catalytic event.

This chapter details how to successfully implement the PP$_i$ase-coupled NTase activity assay for monitoring cGAS activity *in vitro*.

Materials

ATP

GTP

Sodium molybdate

Malachite Green

Triton x-100

Luria Media

Chloramphenicol

E. coli pyrophosphatase

Lysis Buffer - 25mM Tris HCl pH 7.5, 1mM DTT, 5% glycerol, 500mM NaCl, PMSF, lysozyme, benzamidine, DNaseI

Wash Buffer - 25mM Tris HCl pH 7.5, 1mM DTT, 5% glycerol, 500mM NaCl

Amylose Elution Buffer - 25mM Tris HCl pH 7.5, 1mM DTT, 5% glycerol, 500mM NaCl, 10mM maltose

TEV Dialysis Buffer - 25mM Tris HCl pH 7.5, 125mM NaCl, 10mM β-ME

Heparin Buffer - 25mM Tris HCl pH 7.5, 1mM DTT, 5% glycerol, 300mM NaCl

Gel filtration buffer - 25mM Tris HCl pH 7.5, 1mM DTT, 5% glycerol, 300mM NaCl

Storage Buffer - 25mM Tris HCl pH 7.5, 1mM DTT, 20% glycerol, 300mM NaCl

Reaction Buffer – 25mM Tris Acetate pH 7.4, 125mM potassium acetate pH 7.4, 0.5mM Tcep pH 7.4, 5mM magnesium chloride, 5% glycerol

2x Quench Buffer - 25mM Tris Acetate pH 7.4, 125mM potassium acetate pH 7.4, 0.5mM Tcep pH 7.4, 25mM EDTA pH 8, 5% glycerol

Nucleotide stocks

Hydrate ATP and GTP separately in deionized water (ddH_20) supplemented with 20mM HEPES buffer pH 7.4. Target concentrations are 100mM for ATP and 50mM for GTP. Adjust the pH to ~7-8 using concentrated sodium hydroxide. It is best to do this quickly to avoid hydrolysis of either NTP. Measure the concentration of each nucleotide spectrophotometrically. λ_{max} (ATP) = 259nm, $\varepsilon = 15{,}400\ M^{-1}\ cm^{-1}$; λ_{max} (GTP) = 252nm, $\varepsilon = 13{,}700\ M^{-1}\ cm^{-1}$.

Optional: Divalent metal cations can be added to the nucleotide stocks but should be done so prior to pH adjustment. Metals are typically equimolar or in 10% molar excess.

Preparation of recombinant cGAS

This protocol is adapted from (Kranzusch et al. 2013). Clone the full-length, human cGAS sequence into a pET28b vector (Novagen) in-frame with an N-terminal 6xHis-MBP-tag and a TEV protease cleavage site. Transform *E. coli* BL21 Rosetta 2 cells with the plasmid and plate on agar supplemented with Kanamycin and Chloramphenicol. Inoculate a starter culture supplemented with antibiotics with a single clone and grow overnight at 37°C. Inoculate Luria Broth media supplemented with antibiotics with 1:100 overnight culture and grow at 37°C until an OD_{600} of

0.6-0.8. Chill the culture at 4°C for 90 minutes prior to adding 200 µM IPTG. Grow the cells at 16°C overnight. Pellet the cells and store at -80°C. For protein purification, resuspend cells in lysis buffer and lyse by sonication. Clarify the lysate by centrifugation. Apply the clarified lysate to amylose resin, and wash with 4CV of Wash Buffer before eluting with Amylose Elution Buffer. Add TEV protease to the eluted fractions and dialyze overnight at 4°C in TEV Dialysis Buffer. Adjust the dialysate to 5% glycerol and 300mM NaCl. Apply the dialysate to heparin resin (GE Healthcare), and wash with Heparin Wash Buffer. Flash elute the protein in Heparin Wash Buffer supplemented to 800mM NaCl. Apply the eluted fractions to a Superdex 200 16/60 ($cGAS^{FL}$) in Gel Filtration Buffer. Combine the monomer and dimer peaks and apply to amylose resin to remove residual, uncleaved protein. Adjust the flow through to 20% glycerol and concentrate the protein to 50uM. Aliquot, freeze and store the protein at -80°C

Malachite Green Solution (MGS)

0.4 grams of malachite green, 300mls ddH_20, 60mls of concentrated sulfuric acid.

Color Development Solution

200µl 7.5% (w/v) sodium molybdate (ddH_20), 16µl Triton x-100, 800µl MGS

Phosphate Stock

Hydrate sodium phosphate monobasic in ddH_20. Calibrate the phosphate concentration using a commercial stock of aqueous phosphate and the protocol described here for quantifying phosphate.

Preparation of *E. coli* pyrophosphatase

See (Seamon and Stivers 2015) for full details.

Method

1. Prepare a 10x stock of nucleotides. Combine reaction buffer, ATP, GTP and 2 molar equivalents of divalent cation. Metal stocks are typically 1-2M. Mix thoroughly. Note: Additional metal is only required if the nucleotide stocks were not hydrated with metal.

2. Reaction set-up. Combine reaction buffer, 10-200nM PP_iase, $cGAS^{FL}$ and dsDNA to cGAS reaction tubes. Repeat this for control reactions but substitute cGAS with reaction buffer. Add 10x nucleotide(s) to initiate the reaction. Note: The reaction series should be time-matched. Start a timer and initiate a new reaction with nucleotides every 10-15 seconds.

3. Quenching. Add 20µl of 2x Quench Buffer to the appropriate number of wells on the 384-well assay plate. For each time point, remove 20µl of each reaction and add it to the appropriate well. Use the same interval from Step 2 to ensure each reaction runs for the same time.

4. Phosphate standards. In the assay plate, prepare 20µl volumes of 90uM, 60uM, 30uM and 15uM inorganic phosphate diluted in reaction buffer. Add 20µl of 2x Quench Buffer to each.

5. Color development. Prepare the Color Development Solution when all time points have been collected. Add 10µl of Color Development Solution to each well. Set the plate on a nutating shaker at room temperature.

6. Scan the absorbance of each well between 610nm and 650nm in 2nm steps. Calculate the maximum absorbance value for each well. Using the slope of phosphate standard curve, determine the concentration of phosphate in each well. Subtract the phosphate concentration of control reactions from the corresponding cGAS reaction. Calculate the rate of phosphate production by fitting the phosphate concentration over time to a line. Divide this number by two to account for

each pyrophosphate produced. Normalize the reactions by the concentration of $cGAS^{FL}$ to obtain apparent rates of PP_i production min^{-1} $cGAS^{-1}$.

Notes:

1. Conceptually, any homolog of pyrophosphatase can be used in this assay. However, not all homologs share the same catalytic efficiency towards pyrophosphate and may exude differences in activity depending on buffer composition, especially with respect to divalent cation identity and concentration (Kunitz 1962; Zyryanov, Lahti, and Baykov 2005; Halonen et al. 2002). *E. coli* pyrophosphatase is an efficient enzyme under the conditions used here and is simple to purify; high yields of commercial-grade enzyme can be purified from *E. coli* without a chromatographic purification step (Seamon and Stivers 2015). Hence, it was deemed suitable for this purpose.
2. The concentration of pyrophosphatase in the reaction is dictated by the rate of PPi production by the target enzyme. Ensure PPiase is not rate-limiting by measuring catalytic rates of PPi hydrolysis under the desired reaction conditions (Figure 1B). The rate of PPi hydrolysis should be >> faster than the rate of PPi production by the target enzyme.
3. The main disadvantage of this assay is its discontinuous nature. This makes kinetic measurements rather tedious. One alternative strategy is to combine this PP_iase-coupled assay with the real-time, spectrophotometric assay that couples the conversion of MesG (λ_{max}=330nm) and inorganic phosphate to the free base moiety (λ_{max}=360nm) and 1-phosphate-ribose via the enzyme, PNP (Upson et al. 1996; Lloyd et al. 1995). Appropriate considerations should be made to ensure the additional coupling enzymes and reagents do not interfere with cGAS or PP_iase, and that the coupling step is not rate-limiting.

4. This assay is amenable for both 96-well and 384-well formats. High-throughput applications, e.g. small-molecule discovery efforts, are feasible with the assay described here (Cestari and Stuart 2013; Seamon and Stivers 2015; Zhang, Chung, and Oldenburg 1999). Z' values for the 96-well and 384-well will vary heavily on the selected conditions, including substrate concentration, DNA length, DNA concentration and cGAS concentration.

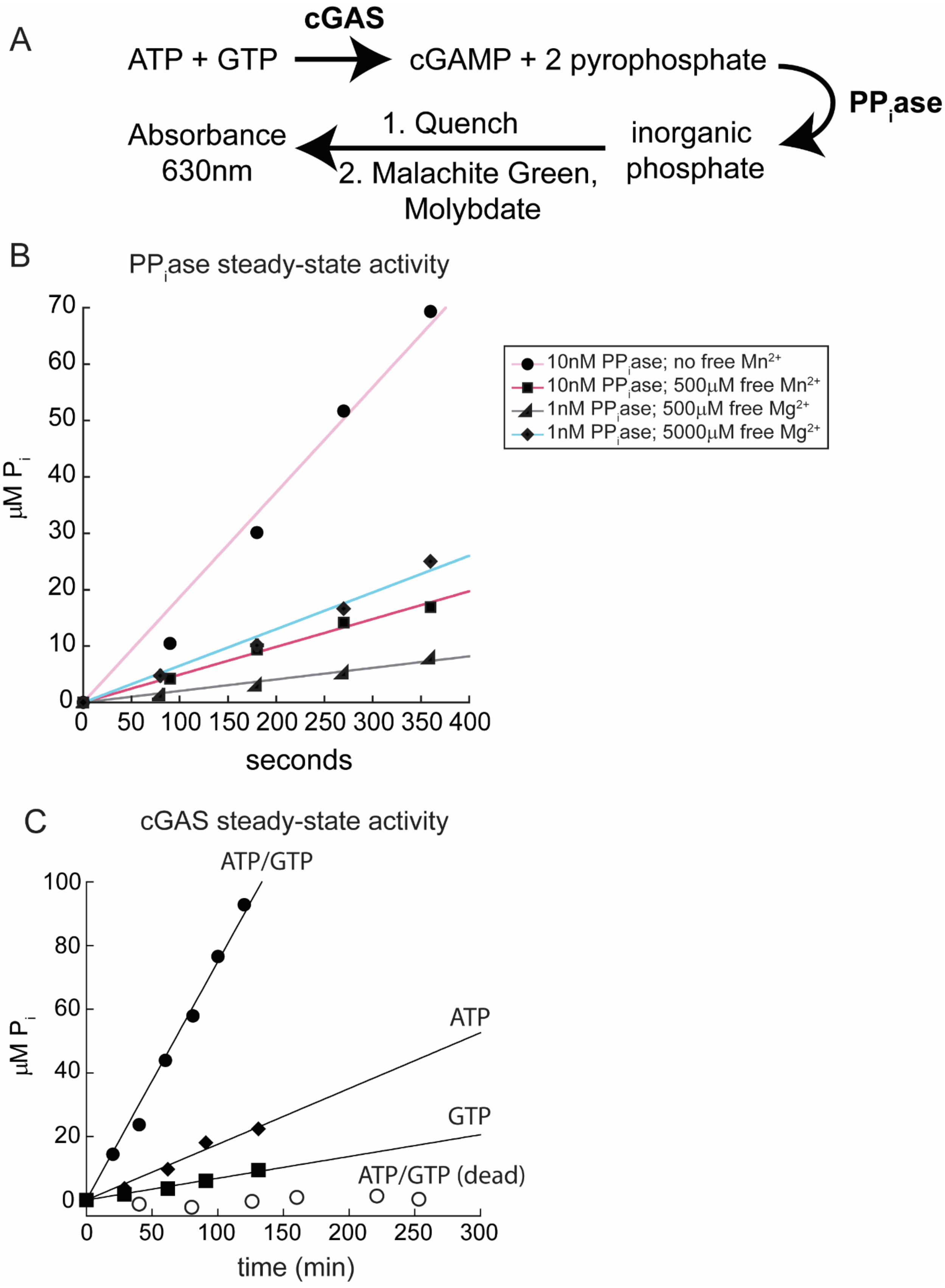
A
cGAS
ATP + GTP
cGAMP + 2 pyrophosphate
PP_iase
inorganic phosphate
1. Quench
2. Malachite Green, Molybdate
Absorbance 630nm
B
PP_iase steady-state activity
10nM PP_iase; no free Mn^{2+}
10nM PP_iase; 500μM free Mn^{2+}
1nM PP_iase; 500μM free Mg^{2+}
1nM PP_iase; 5000μM free Mg^{2+}
μM P_i
0
10
20
30
40
50
60
70
0
50
100
150
200
250
300
350
400
seconds
C
cGAS steady-state activity
ATP/GTP
ATP
GTP
ATP/GTP (dead)
μM P_i
0
20
40
60
80
100
0
50
100
150
200
250
300
time (min)

Figure 1.

A) Scheme of the pyrophosphatase-coupled activity assay.

B) Raw sample data of *E. coli* pyrophosphatase steady-state turnover of inorganic pyrophosphate in the presence of different concentrations of free divalent metal. Each reaction contained 80μM pyrophosphate pre-mixed with one molar equivalent of Mn^{2+} (pink and red) or Mg^{2+} (dark and light blue).

C) Raw sample data of cGAS (125nM) steady state activity in the presence of different substrates and dsDNA. 'dead' - catalytically inert cGAS variant with the mutations E225A/D227A.

References

Ablasser, A., M. Goldeck, T. Cavlar, T. Deimling, G. Witte, I. Rohl, K. P. Hopfner, J. Ludwig, and V. Hornung. 2013. 'cGAS produces a 2'-5'-linked cyclic dinucleotide second messenger that activates STING', *Nature*, 498: 380-4.

Andreeva, L., B. Hiller, D. Kostrewa, C. Lassig, C. C. de Oliveira Mann, D. Jan Drexler, A. Maiser, M. Gaidt, H. Leonhardt, V. Hornung, and K. P. Hopfner. 2017. 'cGAS senses long and HMGB/TFAM-bound U-turn DNA by forming protein-DNA ladders', *Nature*, 549: 394-98.

Baykov, A. A., O. A. Evtushenko, and S. M. Avaeva. 1988. 'A malachite green procedure for orthophosphate determination and its use in alkaline phosphatase-based enzyme immunoassay', *Anal Biochem*, 171: 266-70.

Bose, D., Y. Su, A. Marcus, D. H. Raulet, and M. C. Hammond. 2016. 'An RNA-Based Fluorescent Biosensor for High-Throughput Analysis of the cGAS-cGAMP-STING Pathway', *Cell Chem Biol*, 23: 1539-49.

Cestari, I., and K. Stuart. 2013. 'A spectrophotometric assay for quantitative measurement of aminoacyl-tRNA synthetase activity', *J Biomol Screen*, 18: 490-7.

Chang, G. G., F. Pan, Y. H. Lin, and H. Y. Wang. 1984. 'Continuous spectrophotometric assay for aminoacyl-tRNA synthetases', *Anal Biochem*, 142: 369-72.

Gao, P., M. Ascano, Y. Wu, W. Barchet, B. L. Gaffney, T. Zillinger, A. A. Serganov, Y. Liu, R. A. Jones, G. Hartmann, T. Tuschl, and D. J. Patel. 2013. 'Cyclic [G(2',5')pA(3',5')p] is the metazoan second messenger produced by DNA-activated cyclic GMP-AMP synthase', *Cell*, 153: 1094-107.

Gulen, M. F., U. Koch, S. M. Haag, F. Schuler, L. Apetoh, A. Villunger, F. Radtke, and A. Ablasser. 2017. 'Signalling strength determines proapoptotic functions of STING', *Nat Commun*, 8: 427.

Hall, J., A. Brault, F. Vincent, S. Weng, H. Wang, D. Dumlao, A. Aulabaugh, D. Aivazian, D. Castro, M. Chen, J. Culp, K. Dower, J. Gardner, S. Hawrylik, D. Golenbock, D. Hepworth, M. Horn, L. Jones, P. Jones, E. Latz, J. Li, L. L. Lin, W. Lin, D. Lin, F. Lovering, N. Niljanskul, R. Nistler, B. Pierce, O. Plotnikova, D. Schmitt, S. Shanker, J. Smith, W. Snyder, T. Subashi, J. Trujillo, E. Tyminski, G. Wang, J. Wong, B. Lefker, L. Dakin, and K. Leach. 2017. 'Discovery of PF-06928215 as a high affinity inhibitor of cGAS enabled by a novel fluorescence polarization assay', *PLoS One*, 12: e0184843.

Halonen, P., A. A. Baykov, A. Goldman, R. Lahti, and B. S. Cooperman. 2002. 'Single-turnover kinetics of Saccharomyces cerevisiae inorganic pyrophosphatase', *Biochemistry*, 41: 12025-31.

Ishikawa, H., Z. Ma, and G. N. Barber. 2009. 'STING regulates intracellular DNA-mediated, type I interferon-dependent innate immunity', *Nature*, 461: 788-92.

Kranzusch, P. J., A. S. Lee, J. M. Berger, and J. A. Doudna. 2013. 'Structure of human cGAS reveals a conserved family of second-messenger enzymes in innate immunity', *Cell Rep*, 3: 1362-8.

Kunitz, M. 1962. 'Hydrolysis of adenosine triphosphate by crystalline yeast pyrophosphatase. Effect of zinc and magnesium ions', *J Gen Physiol*, 45(4)Pt 2: 31-46.

Li, T., and Z. J. Chen. 2018. 'The cGAS-cGAMP-STING pathway connects DNA damage to inflammation, senescence, and cancer', *J Exp Med*.

Liu, B., L. Tang, X. Zhang, J. Ma, M. Sehgal, J. Cheng, X. Zhang, Y. Zhou, Y. Du, J. Kulp, J. T. Guo, and J. Chang. 2017. 'A cell-based high throughput screening assay for the discovery of cGAS-STING pathway agonists', *Antiviral Res*, 147: 37-46.

Lloyd, A. J., H. U. Thomann, M. Ibba, and D. Soll. 1995. 'A broadly applicable continuous spectrophotometric assay for measuring aminoacyl-tRNA synthetase activity', *Nucleic Acids Res*, 23: 2886-92.

McMillan, L. J., N. L. Hepowit, and J. A. Maupin-Furlow. 2016. 'Archaeal Inorganic Pyrophosphatase Displays Robust Activity under High-Salt Conditions and in Organic Solvents', *Appl Environ Microbiol*, 82: 538-48.

Seamon, K. J., and J. T. Stivers. 2015. 'A High-Throughput Enzyme-Coupled Assay for SAMHD1 dNTPase', *J Biomol Screen*, 20: 801-9.

Stockbridge, R. B., and R. Wolfenden. 2011. 'Enhancement of the rate of pyrophosphate hydrolysis by nonenzymatic catalysts and by inorganic pyrophosphatase', *J Biol Chem*, 286: 18538-46.

Sun, L., J. Wu, F. Du, X. Chen, and Z. J. Chen. 2013. 'Cyclic GMP-AMP synthase is a cytosolic DNA sensor that activates the type I interferon pathway', *Science*, 339: 786-91.

Upson, R. H., R. P. Haugland, M. N. Malekzadeh, and R. P. Haugland. 1996. 'A spectrophotometric method to measure enzymatic activity in reactions that generate inorganic pyrophosphate', *Anal Biochem*, 243: 41-5.

Vanpouille-Box, C., S. Demaria, S. C. Formenti, and L. Galluzzi. 2018. 'Cytosolic DNA Sensing in Organismal Tumor Control', *Cancer Cell*, 34: 361-78.

Vincent, J., C. Adura, P. Gao, A. Luz, L. Lama, Y. Asano, R. Okamoto, T. Imaeda, J. Aida, K. Rothamel, T. Gogakos, J. Steinberg, S. Reasoner, K. Aso, T. Tuschl, D. J. Patel, J. F. Glickman, and M. Ascano. 2017. 'Small molecule inhibition of cGAS reduces interferon expression in primary macrophages from autoimmune mice', *Nat Commun*, 8: 750.

Wang, M., M. A. Sooreshjani, C. Mikek, C. Opoku-Temeng, and H. O. Sintim. 2018. 'Suramin potently inhibits cGAMP synthase, cGAS, in THP1 cells to modulate IFN-beta levels', *Future Med Chem*, 10: 1301-17.

Yi, L., M. S. Velasquez, T. P. Holler, and R. W. Woodard. 2011. 'A simple assay for 3-deoxy-d-manno-octulosonate cytidylyltransferase and its use as a pathway screen', *Anal Biochem*, 416: 152-8.

Zhang, J. H., T. D. Chung, and K. R. Oldenburg. 1999. 'A Simple Statistical Parameter for Use in Evaluation and Validation of High Throughput Screening Assays', *J Biomol Screen*, 4: 67-73.

Zhang, X., H. Shi, J. Wu, X. Zhang, L. Sun, C. Chen, and Z. J. Chen. 2013. 'Cyclic GMP-AMP containing mixed phosphodiester linkages is an endogenous high-affinity ligand for STING', *Mol Cell*, 51: 226-35.

Zhou, W., A. T. Whiteley, C. C. de Oliveira Mann, B. R. Morehouse, R. P. Nowak, E. S. Fischer, N. S. Gray, J. J. Mekalanos, and P. J. Kranzusch. 2018. 'Structure of the Human cGAS-DNA Complex Reveals Enhanced Control of Immune Surveillance', *Cell*, 174: 300-11 e11.

Zyryanov, A. B., R. Lahti, and A. A. Baykov. 2005. 'Inhibition of family II pyrophosphatases by analogs of pyrophosphate and phosphate', *Biochemistry (Mosc)*, 70: 908-12.

Chapter 3

The allosteric activation of cGAS underpins its dynamic signaling landscape

Introduction

Whether arising endogenously or exogenously, double-stranded (ds)DNA in the cytoplasm of eukaryote cells indicates major problems (Chen, Sun, and Chen 2016; Paludan and Bowie 2013). For instance, genomic instability and damaged mitochondria introduce dsDNA into the cytoplasm (Chen, Sun, and Chen 2016; Denais et al. 2016; Paludan and Bowie 2013; West and Shadel 2017; Shen et al. 2015; Mackenzie et al. 2017), and nearby rampant necrosis or pyroptosis can lead dsDNA to the cytoplasm of neighboring cells (Abe et al. 2013; Ishii et al. 2001). Moreover, the invasion of pathogenic bacteria or viruses introduces foreign dsDNA into the host cytoplasm (Chen, Sun, and Chen 2016; Paludan and Bowie 2013).

In metazoans, cyclic GMP-AMP synthase (cGAS) plays a predominant role in initiating host innate immune responses against cytoplasmic dsDNA (Chen, Sun, and Chen 2016). Upon detecting cytoplasmic dsDNA, cGAS cyclizes ATP and GTP into [2'-5', 3'-5']-linked cGAMP (Gao, Ascano, et al. 2013), a unique host second-messenger for activating type-1 mediated stress-responses via Stimulator of Interferon Genes (STING). cGAS is integral not only to the host defense against all pathogens entailing DNA for replication (e.g. HIV, HSV, *L. monocytogenes*; (Hansen et al. 2014; Reinert et al. 2016; Gao, Wu, et al. 2013), but also to damaged organelles (West et al. 2015; Mackenzie et al. 2017). Moreover, cGAS plays a major role in regulating autoimmunity (e.g. Aicardi-Goutières syndrome and systemic lupus erythematosus (Pokatayev et al. 2016; Vincent et al. 2017; An et al. 2017; Gao et al. 2015)) and tumor formation and growth (Bai et al. 2017).

A signature of IFN-1 signaling is its variable outcomes, which include antiviral gene expression, cellular senescence, autophagy, and apoptosis (van Boxel-Dezaire, Rani, and Stark 2006; Li and Chen 2018; Liang et al. 2014; Li et al. 2016; Sun et al. 2013; Yang et al. 2017). cGAS contributes significantly to this complex signaling landscape, with its signal strength, signaling duration, and cellular contexts influencing the type of outcomes (Li and Chen 2018). For example, the outcome of the cGAS pathway depends on cell type (e.g. non-apoptotic macrophages vs. apoptotic T-cells (Gulen et al. 2017; Li et al. 2016; Tang et al. 2016; Larkin et al. 2017)), the amount of cGAMP (e.g. autophagy vs. apoptosis (Liang et al. 2014; Li et al. 2016; Tang et al. 2016; Gulen et al. 2017)), and the duration for which cells are stimulated with cGAMP (antiviral gene expression vs. apoptosis (Li et al. 2016; Tang et al. 2016; Gulen et al. 2017; Larkin et al. 2017)). The goal of the present study is to understand the molecular mechanisms by which cGAS drives such a dynamic signaling landscape.

Resting cGAS is thought to be an inactive monomer, and formation of a 2:2 dimer with dsDNA within the catalytic domain (human cGAS residue 157-522) is necessary for activation (2 cGAS molecules on 2 dsDNA duplexes (Li et al. 2013; Zhang et al. 2014)). cGAS recognizes dsDNA independent of sequence (Gao, Ascano, et al. 2013; Kranzusch et al. 2013; Li et al. 2013; Zhang et al. 2014), and it was initially proposed that any dsDNA long enough to support cGAS dimerization could activate the enzyme equally well (e.g. ~15 base-pairs, bps (Li et al. 2013; Zhang et al. 2014; Chen, Sun, and Chen 2016)). However, it was long known that dsDNA of at least 45 bp was required to elicit IFN-1 responses in cells (Stetson and Medzhitov 2006; Unterholzner et al. 2010; Chen, Sun, and Chen 2016). Indeed, two recent studies demonstrated that cGAS discriminates against short dsDNA (Andreeva et al. 2017; Luecke et al. 2017b). For instance, cGAS is minimally activated in cells by dsDNA shorter than 50 bps, and maximal activation requires dsDNA longer than 200 bps, with the length-dependence more pronounced at lower dsDNA concentrations (Andreeva et al. 2017; Luecke et al. 2017b). The dependence on dsDNA length is thought to arise because cGAS dimers linearly propagate along the length of two parallel dsDNA strands without making inter-dimer contacts, consequently generating a ladder-like complex that increases the overall stability via avidity (Andreeva et al. 2017). Together, it is believed that dsDNA length-based signal-to-noise filtration occurs at the binding/recognition stage (i.e. different K_Ds for different dsDNA lengths), but not at the signal transduction step (i.e. same $V_{\max}$ for different dsDNA lengths (Andreeva et al. 2017)).

Our understanding of the mechanisms by which cGAS is activated has evolved over the years, yet it remains unclear why two conflicting views on the role of dsDNA length have existed. Moreover, we noted that neither the previous (dsDNA length-independent) nor current (dsDNA length-dependent) activation model provides a robust framework for understanding how cGAS might be able to shape its diverse signaling landscape. First, the relationship between dsDNA binding and activation is poorly established. For instance, it remains to be tested whether the initial dsDNA recognition step alone sufficiently explains the dsDNA length-dependent activation of cGAS in cells. Second, the ladder model implies that dimerization efficiency continuously increases with dsDNA lengths (> 1000 bps), while the optimal cellular response peaks with any dsDNA longer than ~200 bps (Andreeva et al., 2017). Third, the ladder model is heavily based on structural and functional studies of the catalytic domain of cGAS (cGAS^{cat}). It was recently proposed that the N-domain of cGAS binds dsDNA and plays a crucial role in its cellular function (Tao et al. 2017; Wang, Ning, et al. 2017). Moreover, dsDNA binding by the N-domain is thought to enhance the activity of the monomeric enzyme, consequently lifting the dsDNA length restriction (Lee et al. 2017). Thus, it is not clear whether the ladder-like arrangement applies exclusively to cGAS^{cat}, or whether it is germane to the full-length protein (cGAS^{FL}). Finally, given that cGAS is the predominant sensor for cytoplasmic dsDNA (Chen, Sun, and Chen 2016), it is imperative for this enzyme to amplify and attenuate its signaling cascade in a switch-like manner to ensure proper host responses. How cGAS achieves this important task remains poorly understood.

We find here that human cGAS can auto-dimerize without dsDNA. dsDNA regulates this intrinsic monomer-dimer equilibrium not only in a cooperative, but also in a length-dependent manner. Unexpectedly, substrates (ATP/GTP) can pull cGAS into the dimeric state without dsDNA. Because ligand binding is coupled to dimerization, the length of dsDNA not only regulates binding and dimerization (signal recognition), but also the substrate binding and catalysis (signal transduction). Compared to cGAS^{cat}, cGAS^{FL} auto-dimerizes more readily and also couples binding of both substrate and dsDNA to dimerization more efficiently, revealing a new function of the N-domain in potentiating the dimerization of cGAS. Dimerization is essential for dsDNA-mediated activation of both cGAS^{FL} and cGAS^{cat}, and the dimers do not arrange in an ordered configuration on long dsDNA, suggesting the role of dsDNA length is to simply regulate the probability of dimerization. Importantly, shifting the monomer-dimer equilibrium via elevated enzyme and ATP/GTP concentrations in the absence of dsDNA does not override the requirement for dsDNA to activate cGAS. Instead, these other factors prime the enzyme to be activated even by short dsDNA, indicating that the dependence on duplex length can change according to cellular reaction context. Together, our results set forth a unifying activation model for cGAS in which the intrinsic monomer-dimer equilibrium poises the enzyme to dynamically turn its signaling pathway on or off in a switch-like fashion.

Results

Human cGAS^{cat} can dimerize without dsDNA

Human cGAS^{cat} (denoted as cGAS^{cat} hereafter) eluted as two peaks in size-exclusion chromatography (SEC) depending on protein concentration (Figure 1A). With decreasing protein concentrations, the two peaks progressively merged into the one with the lower apparent hydrodynamic radius (Figure 1A), suggesting that cGAS^{cat} is subject to an intrinsic monomer-dimer equilibrium without dsDNA (Figure 1-figure supplement 1). This was surprising, as previous studies showed that mouse cGAS^{cat} behaved as a monomer (Li et al. 2013); we speculate that mouse-cGAS^{cat} intrinsically dimerizes more weakly.

To further test the intrinsic dimerization capability of cGAS, we examined the oligomeric state using small-angle x-ray scattering (SAXS). SAXS revealed that the radius of gyration (R_g) and maximum diameter (D_{max}) for *apo*- cGAS^{cat} at all tested concentrations aligned better with those of dsDNA-bound mouse-cGAS^{cat} dimer (Figures 1C-D; (Li et al. 2013)). We analyzed the distrbution of monomeric and dimeric species using SAXS-estimated molecular weight (SAXS MoW2) and OLIGOMER in ATSAS (Figure 1D (Petoukhov and Svergun 2013; Petoukhov et al. 2012; Mylonas and Svergun 2007)). Here, the fraction of dimeric species was proportional to protein concentration, and the dimerization constant was estimated to be ~20 μM (Figure 1D). Together, we concluded that cGAS has an intrinsic, albeit weak, capacity to dimerize in the absence of ligands.

Figure 1

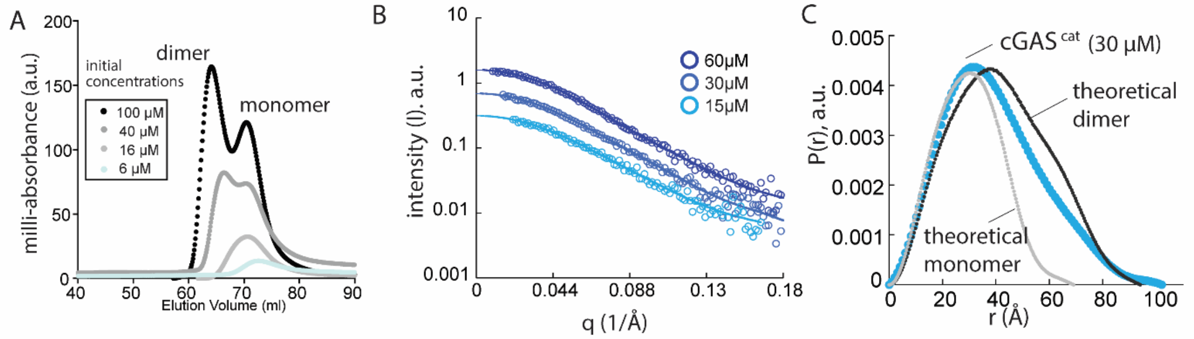

D

protein	method	[] (µM)	R_g (Å)$_{primus}$	D_{max}(Å) primus	$MW_{est,avg}$ (kDa)	% dimer
cGAS^{cat}	SAXS	60	31.1 ± 0.7	102	72 ± 4	68
cGAS^{cat}	SAXS	30	30.4 ± 2.5	102	69 ± 6	60
cGAS^{cat}	SAXS	15	28.4 ± 3.4	103	63 ± 4	48
theoretical						
mouse-cGAS^{cat}	crystal	monomer	22.6	64	42	0
mouse-cGAS^{cat}	crystal	dimer	32.0	86	84	100

* theoretical values generated based on the crystal structures (PDB ID: 4lez)
MW_{est},avg is the average MW estimate determined from datporod, MoW2 and OLIGOMER.

Figure 1. human wild-type cGAS^{cat} can dimerize on its own

(A) SEC (Superdex 200 16/600) profile of cGAS^{cat}.

(B) SAXS scattering profile of cGAS^{cat}.

(C) Pair-wise distance distribution functions of cGAS^{cat}. Theoretical P(r)s from mouse-cGAS^{cat} are shown for comparison (PDB ID: 4lez).

(D) Summary of SAXS experiments.

Figure 1 Supplements

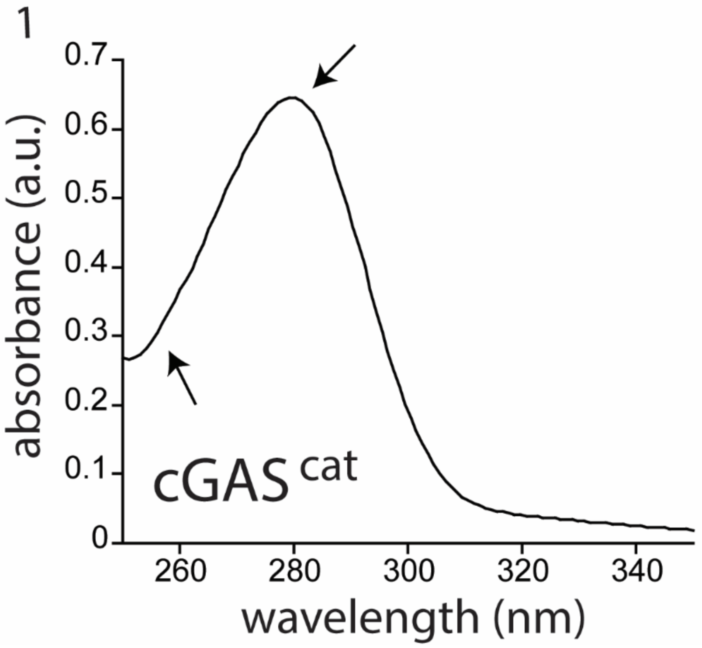

(Figure 1 figure supplement 1) Uv-vis absorbance profile of purified cGAS^{cat}. The predominant peak at 280 nm and the lack thereof at 260 nm consistently indicate no significant nucleic acid contamination.

cGAS behaves like a classic allosteric enzyme

In allosteric signaling enzymes, incoming signal (activator) and substrates either exclusively or preferentially bind to the active state and stabilize the corresponding conformation (Monod, Wyman, and Changeux 1965; Sohn, Grant, and Sauer 2007; Sohn and Sauer 2009; Koshland, Nemethy, and Filmer 1966). Such a coupling mechanism synchronizes conformational states with activity states, thereby allowing the enzymes to generate switch-like responses (Monod, Wyman, and Changeux 1965; Sohn, Grant, and Sauer 2007; Sohn and Sauer 2009; Koshland, Nemethy, and Filmer 1966). Importantly, preferential, but not exclusive ligand binding to the active state grades signaling output, as the distribution of active and inactive species is dictated by the relative binding affinity of different activators to either state (Sohn and Sauer 2009; Tsai and Nussinov 2014; Monod, Wyman, and Changeux 1965). Our observation that cGAS can dimerize on its own suggests a new framework for understanding its activation mechanism (Figure 2A). Here, *apo*-cGAS is placed in an intrinsic allosteric equilibrium where it is predominantly an inactive monomer under resting conditions. Overexpression (Ma et al. 2015), substrate binding, and cytoplasmic dsDNA synergistically activate cGAS by promoting dimerization. Furthermore, given that monomeric cGAS binds dsDNA (Andreeva et al. 2017; Li et al. 2013), it is possible that dsDNA length determines the fraction of active dimers (Figures 2B), thus underpinning the duplex length dependent cellular activity (Andreeva et al. 2017; Luecke et al. 2017b). Below, we describe a series of experiments to further test and develop this allosteric framework for understanding the activation of cGAS.

The cellular activity of cGAS is dsDNA length-dependent (Andreeva et al. 2017; Luecke et al. 2017b), as if the enzyme uses duplex length as a ruler to differentiate between signal and noise.

Currently, it is believed that this length-based noise filtration occurs only at the initial encounter step, with longer dsDNA invoking a ladder-like arrangement (Andreeva et al. 2017). However, all previous binding studies entailed raising cGAS concentration (Andreeva et al. 2017; Li et al. 2013), which intrinsically alters the dimer population. Thus, we re-examined the coupled relationship between dsDNA-binding and dimerization without altering the intrinsic dimerization equilibrium. First, using both direct and competition methods, we observed that cGAS^{cat} indeed binds dsDNA in a length-dependent manner (Figure 2-figure supplement 1A-B). Next, to directly monitor dimerization, we conjugated a FRET donor and acceptor peptide to two populations of cGAS^{cat} via sortaseA (FRET: Förster Resonance Energy Transfer; Figure 2-figure supplement 1C). The dimerization of a 1:1 mixture of donor- and acceptor-labeled cGAS^{cat} at physiologically relevant concentrations was then tracked by changes in FRET emission ratios between the donor and acceptor with increasing concentrations of dsDNA (Figure 2-figure supplement 1C; physiological concentrations of cGAS vary ~10-500 nM (Andreeva et al. 2017; Ma et al. 2015; Du and Chen 2018b)).

Increasing concentrations of 24-bp dsDNA did not induce significant changes in FRET ratios (Figure 2C), consistent with the previous report that such a short dsDNA binds cGAS but cannot induce dimerization (Andreeva et al. 2017). With longer dsDNA, we observed more robust changes in FRET signals (Figure 2C). Importantly, the half-maximal dsDNA concentrations necessary to induce the FRET signal (K_{FRET}) decreased with longer dsDNA, and the length dependence plateaued around ~ 300 bps (Figures 2C-D). The maximal change in FRET ratio also generally increased with longer dsDNA, suggesting the dimeric fraction increased with longer dsDNA (Figure 2C). The fitted Hill constants in these experiments were between 1.5 and 2, indicating that dsDNA-induced dimerization is a cooperative process (Figure 2E). Overall, our results confirm that dsDNA binding and dimerization are directly coupled, consistent with the idea that the intrinsic monomer-dimer equilibrium underpins dsDNA length discrimination by cGAS (Figures 2A-B).

It is thought that cGAS does not bind ATP/GTP in the absence of dsDNA, as the loops surrounding the active site would block substrate entry (Gao, Ascano, et al. 2013). However, cGAS can bind cGAMP in the absence of dsDNA, and multiple crystal structures indicate that the B-factors of loops surrounding the active site are 5- to 20-fold higher than the protein core, suggesting cGAS might be able to weakly interact with ATP/GTP even without dsDNA (e.g. PDB IDs: 4k8v, 4o69, and 4km5; (Gao, Ascano, et al. 2013; Kranzusch et al. 2013; Zhang et al. 2014)). Thus, we tested whether ATP/GTP and their nonhydrolyzable analogues (AMPcPP/GMPcPP) could induce dimerization. Here, substrates increased the FRET ratio, albeit to a lower extent than long dsDNA (Figure 2F), suggesting that substrates alone can pull $\mathrm{cGAS}^{\mathrm{cat}}$ into the dimeric state to some degree. The lower capacity of AMPcPP/GMPcPP to induce FRET changes is consistent with our observations that the analogues bind more weakly than ATP/GTP (K_i = 280 μM (Figure 2-figure supplement 1D) vs. K_M of ~100 for ATP/GTP with dsDNA, see Figure 3 below). Together, our results suggest that the fraction of active, dimeric cGAS would be partitioned according to the length of dsDNA and the availability of substrates (Figure 2A). Thus, our results support the notion that cGAS employs a strategy similar to classical allosteric enzymes to generate a graded output.

Figure 2

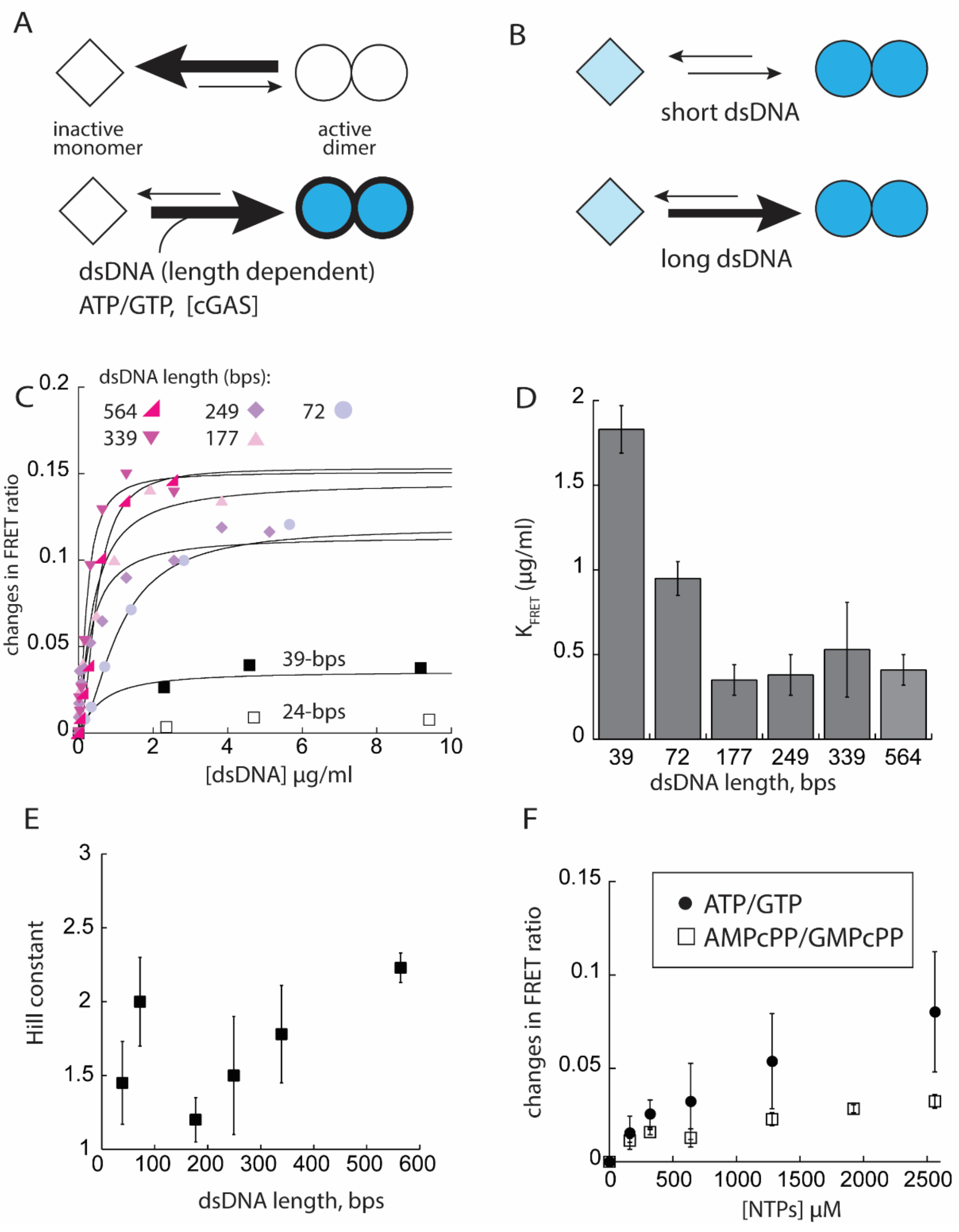

Figure 2. dsDNA cooperatively induces the dimerization of cGAS in a length dependent manner

(A) A scheme describing the allosteric framework of cGAS activation. Here, cGAS is subject to an intrinsic allosteric equilibrium with two major activity/conformational states, namely inactive monomer and active dimer. Resting cGAS is predominantly an inactive monomer (top). dsDNA (length-dependent) binding, increasing cGAS concentration, and substrate binding synergistically drive the allosteric equilibrium toward the active dimer.

(B) An allosteric model describing dsDNA length-dependent distribution of active dimers and inactive (basally active) monomers.

(C) Changes in the ratio between FRET donor emission (λ_{max}: 578 nm) and the acceptor emission (λ_{max}: 678 nm) of labeled cGAS^{cat} (20 nM each) at indicated dsDNA concentrations.

(D) A plot of dimerization efficiency (K_{FRET}) vs. dsDNA length ($n = 3$; ± SD).

(E) A plot of fitted Hill constants vs. dsDNA lengths ($n = 3$; ± SD).

(F) Changes in the ratio between the FRET donor/acceptor emission ratios of labeled cGAS^{cat} (20 nM each) at indicated NTP pair concentrations. ($n = 3$; ± SD).

Figure 2 Supplements 1

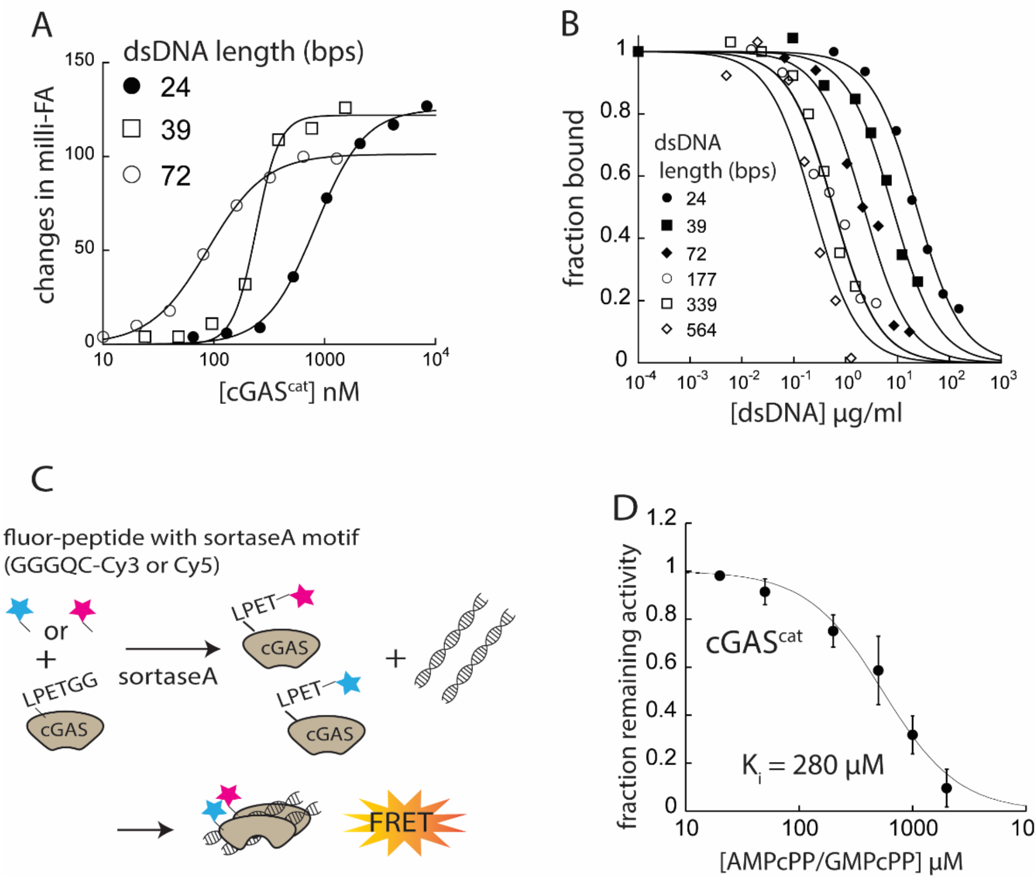

(Figure 2 figure supplement 1A) Binding of cGAS^{cat} to each FAM-labeled dsDNA (5 nM) was determined by FA. The lines are fits to a standard binding isotherm.

(Figure 2 figure supplement 1B) Competition binding assay using 72-bp FAM-dsDNA (5 nM) and cGAS^{cat} (80 nM; ~ K_D for 72-bp FAM-dsDNA) against various unlabeled dsDNA lengths; the lines are fits to a competition binding equation: $(1/(1+(\text{dsDNAcompetitor})/IC_{50})^{\text{Hill constant}})$. Fraction bound was calculated based on the changes in fluorescence anisotropy (FA) of 72-bp FAM-dsDNA.

(Figure 2 figure supplement 1C) Scheme for FRET-based dimerization assay.

(Figure 2 figure supplement 1D) Competition activity assay using 339-bp dsDNA (4 µg/ml) and cGAS^{cat} (50 nM) and 150 µM ATP/GTP against increasing concentrations of AMPcPP/GMPcPP;

the lines are fits to a competition binding equation: $(1/(1+(\text{competitor})/IC_{50})^{\text{Hill constant}})$. The Reported K_i was calculated using the Cheng-Prusoff equation ($K_i = IC_{50}/([1+([S]/K_M)])$.

A new quantitative assay for cGAS enzymatic activity

All published methods that quantitatively monitor the enzymatic activity of cGAS track cGAMP production, and are not ideal for mechanistic studies because they are low throughput or make it difficult to saturate the enzyme with substrates (e.g. TLC, HPLC-Mass-Spec, and fluorescently-labeled ATP/GTP; (Andreeva et al. 2017; Gao, Ascano, et al. 2013; Hall, Ralph, et al. 2017a; Vincent et al. 2017)). cGAS generates two inorganic pyrophosphates (PP_i) per cGAMP. Thus, we adapted a pyrophosphatase (PP_iase)-coupled assay to monitor cGAS activity (Figure 3A; (Seamon and Stivers 2015)). Using this assay, we found that $cGAS^{cat}$ produces PP_i most efficiently in the presence of a 1:1 mixture of ATP and GTP plus dsDNA (Figure 3B; > 90% of its NTase activity produces cGAMP when ATP and GTP are equimolar (Gao, Ascano, et al. 2013)). Moreover, no PP_i production was observed from an inactive cGAS variant (E225A-D227A-$cGAS^{cat}$ (Gao, Ascano, et al. 2013); Figure 3B), and the activity of PP_iase was not rate-limiting (Figure 3-figure supplement 1). Thus, we concluded that the PP_iase-coupled assay provides a robust method to quantitatively monitor the enzymatic activity of cGAS.

dsDNA length regulates the extent of activation

Our experiments thus far support an activation model in which dsDNA length determines the distribution between active dimers and inactive monomers (Figure 2A-B). This mechanism predicts that different dsDNA lengths would produce graded maximal signaling outputs (V_{max}) even at saturating concentrations of dsDNA (Sohn and Sauer 2009). In contrast, recent work suggests that the dsDNA length-dependent activity of cGAS arises solely at the signal recognition step (binding), and not at the signal transduction step (enzymatic step; (Andreeva et al. 2017)). However, the authors did not conduct their studies under steady-state conditions due to their use of fluorescently-labeled substrates (Andreeva et al. 2017). Because our coupled-assay eliminates this issue, we directly tested whether dsDNA length could regulate the enzymatic activity of cGAS. Here, we found that cGAS^{cat} has low basal activity without dsDNA (180 ± 30 $M^{-1}min^{-1}$), which can be increased by 50-fold with > 300 bp dsDNA (Figure 3C). dsDNA concentrations required to induce the half-maximal activity of cGAS^{cat} increased with shorter dsDNA (K_{act}; Figure 3C and Figure 3-figure supplement 2A-B), consistent with the previously observed length-dependent binding ((Andreeva et al. 2017). Importantly, the maximum dsDNA-induced activity (k_{max}) also decreased with shorter dsDNA (Figures 3C and Figure 3-figure supplement 2A and 2C), which is in contrast to the previous report proposing that the role of dsDNA length is limited to binding (Andreeva et al. 2017). Moreover, normalizing the k_{max} by K_{act} for each dsDNA length showed that the overall signaling efficiency of cGAS^{cat} (dsDNA binding and maximum output) changes more drastically compared to either parameter alone (Figure 3D, see also Figure 3- figure supplement 2A-C). For instance, the overall signaling efficiency changes by nearly 100-fold between 24 to 339 bp dsDNA, while either binding or maximal activity alone changes only up to 10-fold (Figure 3D, see also Figure 3- figure supplement 2A-D). Together, our observations suggest that cGAS discriminates against short dsDNA not only at the initial recognition step, but again at the signal transduction step, resulting in two-stage dsDNA length discrimination.

dsDNA length regulates formation of the enzyme-substrate complex (K_M) and the turnover efficiency (k_{cat}) of cGAS

We next determined substrate turnover kinetics in the presence of various dsDNA lengths. Without dsDNA, cGAS^{cat} showed slow, but measurable NTase activities (Figure 3- figure supplement 1B). With saturating dsDNA longer than 300 bps, the K_M of cGAS^{cat} for ATP/GTP was near 100 μM, and the k_{cat} was 5 min^{-1} (Figures 3E and Figure 3-figure supplement 2D). The observed K_M for ATP/GTP is comparable to previously reported values measured using Surface Plasmon Resonance (SPR) and rapid-fire Mass-Spec for both human and mouse enzymes (Hall, Ralph, et al. 2017a; Vincent et al. 2017). Moreover, the relatively slow k_{cat} is consistent with a report indicating that human cGAS is considerably slower than mouse cGAS (~20 min^{-1}) (Vincent et al. 2017). Considering intracellular concentrations of ATP and GTP are > 1 mM and ~500 μM, respectively (Traut 1994; Chen, Freinkman, et al. 2016), our result suggests that once cGAS encounters cytoplasmic dsDNA, one cGAMP would be generated in less than 20 sec, compared to about one per 15 min in the absence of dsDNA. With shorter dsDNA, the K_M increased about 2-fold, and the k_{cat} decreased up to 4-fold (Figures 3-figure supplement 3D). Combined, our results indicated that the overall catalytic efficiency of cGAS can change up to 8-fold (k_{cat}/K_M) by the length of bound dsDNA (Figure 3F and Figure 3-figure supplement 3D). On another note, the fitted Hill constants in these experiments were near two for all dsDNA lengths (Figure 3-figure supplement 2D), consistent with the observation from mouse cGAS^{cat} (Vincent et al. 2017). Because most cGAS^{cat} populations would be dimeric with saturating long dsDNA, the observed cooperativity is likely from substrate-substrate interactions (i.e. ATP binding enhances GTP binding or *vice versa*; (Vincent et al. 2017)). Overall, these results further support that dsDNA length can grade the enzymatic activity of cGAS.

Figure 3

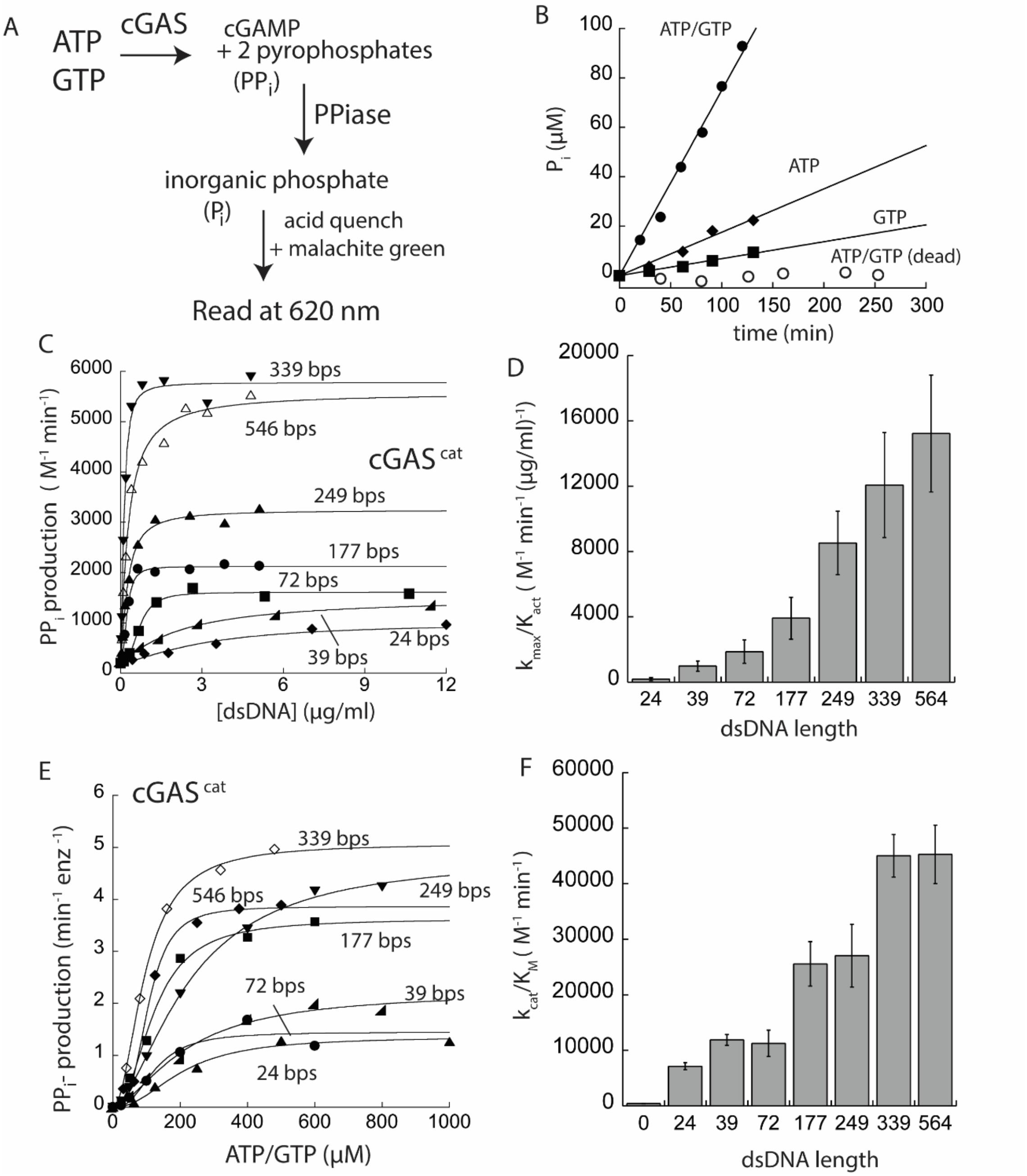

Figure 3. dsDNA length can grade the activity of cGAS

(A) PPiase-coupled assay scheme.

(B) A plot of time-dependent P$_i$ production of cGAS^{cat} (125 nM) at various conditions (dead: E225A-D227A).

(C) A plot of the dsDNA concentration-dependent NTase activity of cGAS^{cat} (25 nM) and 1 mM ATP/GTP with various duplex lengths. Lines are fits to a Hill form of the Michaelis-Menten equation.

(D) A plot of dsDNA-affinity normalized maximal activities of cGAS^{cat} vs. dsDNA lengths (n = 3; ± SD).

(E) Substrate dependence of the steady-state rate of NTase activity by cGAS^{cat} (125 nM) with saturating amounts of each dsDNA (6X K_{act}). Lines are fits to a Hill form of the Michaelis-Menten equation.

(F) A plot of catalytic efficiencies (k_{cat}/K_M) vs. dsDNA lengths (n = 3; ± SD).

Figure 3 Supplements 1

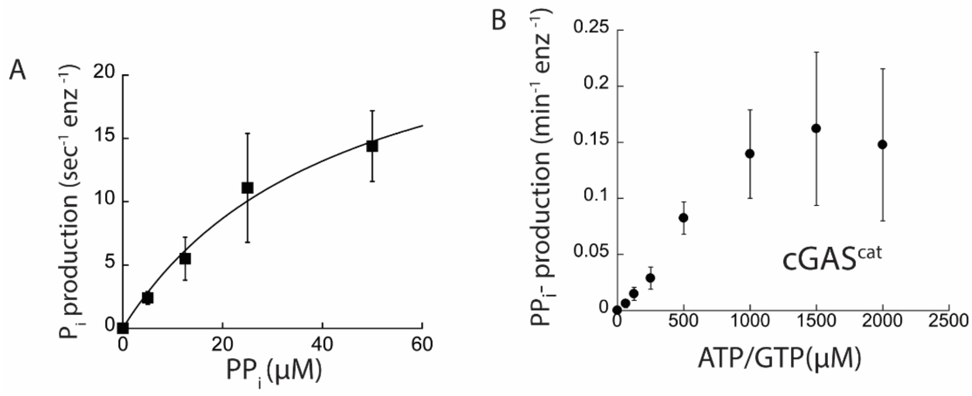

(Figure 3 figure supplement 1A) Steady-state kinetics of PPiase. Calculated k_{cat}/K_M is ~ 675,000$M^{-1}sec^{-1}$, which is about 1,000-fold faster than that of cGAS in the presence of saturating 564-bp dsDNA (~750 $M^{-1}sec^{-1}$).

(Figure 3 figure supplement 1B) Steady-state NTase rates of dsDNA free cGAS$^{\mathrm{cat}}$ (estimated $k_{\mathrm{cat}}/K_M \approx 800$ $M^{-1}min^{-1}$)

Figure 3 Supplements 2

A

dsDNA_n (bps)	M^{-1} min^{-1}	K_{act} (ug/ml)	Hill Constant
24	880 ± 330	4.68 ± 2.95	1.44 ± 0.50
39	1760 ± 530	1.78 ± 0.59	1.55 ± 0.25
72	2150 ± 740	1.15 ± 0.48	1.47 ± 0.52
177	3020 ± 820	0.82 ± 0.33	1.21 ± 0.35
249	3300 ± 290	0.34 ± 0.09	1.28 ± 0.23
339	6100 ± 1100	0.53 ± 0.19	1.35 ± 0.53
564	6700 ± 800	0.43 ± 0.15	1.31 ± 0.21

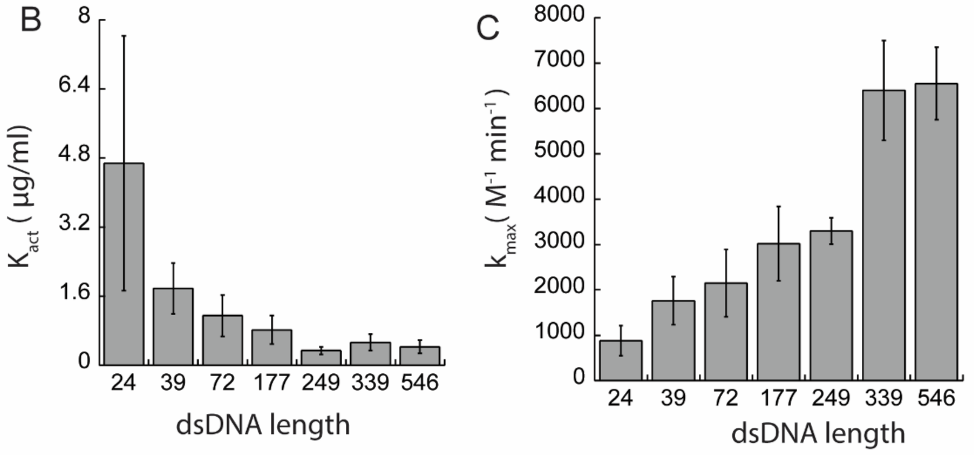

D

dsDNA (bps)	k_{cat} (enz^{-1} min^{-1})	K_M ATP/GTP (μM)	Hill Constant
24	1.3 ± 0.2	204 ± 26	1.94 ± 0.29
39	2.2 ± 0.5	222 ± 16	1.97 ± 0.14
72	1.9 ± 0.6	167 ± 23	1.82 ± 0.22
177	3.3 ± 0.8	129 ± 29	1.98 ± 0.31
249	4.6 ± 0.7	169 ± 24	2.04 ± 0.32
339	5.0 ± 0.8	111 ± 14	2.08 ± 0.38
564	4.8 ± 0.6	106 ± 13	2.44 ± 0.44

(Figure 3 figure supplement 2A) Table summarizing activation parameters.

(Figure 3 figure supplement 2B) A plot of the half-maximal dsDNA concentrations (K_{act}) required to activate cGAS (i.e. apparent binding affinity) vs. dsDNA lengths.

(Figure 3 figure supplement 2C) A plot of the maximal dsDNA induced NTase activity of cGAS (k_{max}) vs. dsDNA lengths.

(Figure 3 figure supplement 2D) Table summarizing steady-state kinetic parameters.

The N-domain potentiates cGAS dimerization

It was recently reported that the N-domain of cGAS (residues 1-156) plays an important role *in vivo* by providing an additional nonspecific dsDNA binding site (Tao et al. 2017; Wang, Ning, et al. 2017). Moreover, it was proposed that the N-domain reduces the requirement for long dsDNA, because it facilitates the activation of monomeric, mouse cGAS (Lee et al. 2017). To test whether our findings with cGAS^{cat} apply to the full-length enzyme, we generated recombinant cGAS^{FL}. The full-length protein eluted as two peaks in SEC (Figure 4A), exhibited monomer-dimer behavior by SAXS (Figure 4B, and Figure 4-figure supplements 1B-C), and was free from nucleic acid contamination (Figure 4-figure supplement 1A). Of note, it appeared that cGAS^{FL} has a higher dimerization propensity compared to cGAS^{cat}, as indicated by broader peak distribution at 15 μM (Figure 4A vs. Figure 1A). Supporting this notion, SAXS analyses also suggested that the dimerization constant of cGAS^{FL} is about 2-fold less than cGAS^{cat} (Figure 4-figure supplement 1B-C; cGAS^{cat} is 48% dimeric at 15 μM; Figure 1C-D). To further test that the N-domain can dimerize, we generated recombinant N-domain (cGAS^{N}). cGAS^{N} migrated as a dimer by SEC, and had a SAXS-estimated molecular weight consistent with a dimer (Figure 4-figure supplement 2A-C). Of note, in our solution equilibrium assay, cGAS^{N} bound dsDNA much more weakly than cGAS^{cat}, which is in contrast to the non-equilibrium mobility assay used by Tao et al. ((Tao et al. 2017); Figure 4-figure supplement-2D-E; $K_D > 10$ μM). These observations suggest a new role of N-domain in assisting the dimerization of cGAS.

cGAS^{FL} still bound dsDNA in a length dependent manner (Figure 4-figure supplement 3A), and displayed dsDNA length-dependent changes in FRET (Figure 4C, Figure 4-figure supplement 3B). K_{FRET}s for dsDNA > 72-bp were roughly equivalent to the lowest enzyme concentration practically accessible in our assays (Figure 4C, Figure 4-figure supplement 3B), indicating that the full-length protein binds and dimerizes more readily on dsDNA. Substrates and their analogues also produced more robust changes in FRET signals for cGAS^{FL} compared to cGAS^{cat} (Figure 4D, Figure 4-figure supplements 3B-C), further corroborating that the full-length enzyme couples substrate binding to dimerization more efficiently due to its enhanced intrinsic dimerization activity. We also found that dsDNA length graded K_{act} and k_{max} of cGAS^{FL}, similar to cGAS^{cat} (Figure 4E, Figure 4-figure supplement 3D); K_M and k_{cat} for cGAS^{FL} were also graded according to dsDNA lengths (Figure 4F, Figure 4-figure supplement 3E-F). Overall, our observations indicate that cGAS^{FL} and cGAS^{cat} operate within the same molecular framework, and reveal a new role for the N-domain in potentiating cGAS dimerization.

Figure 4

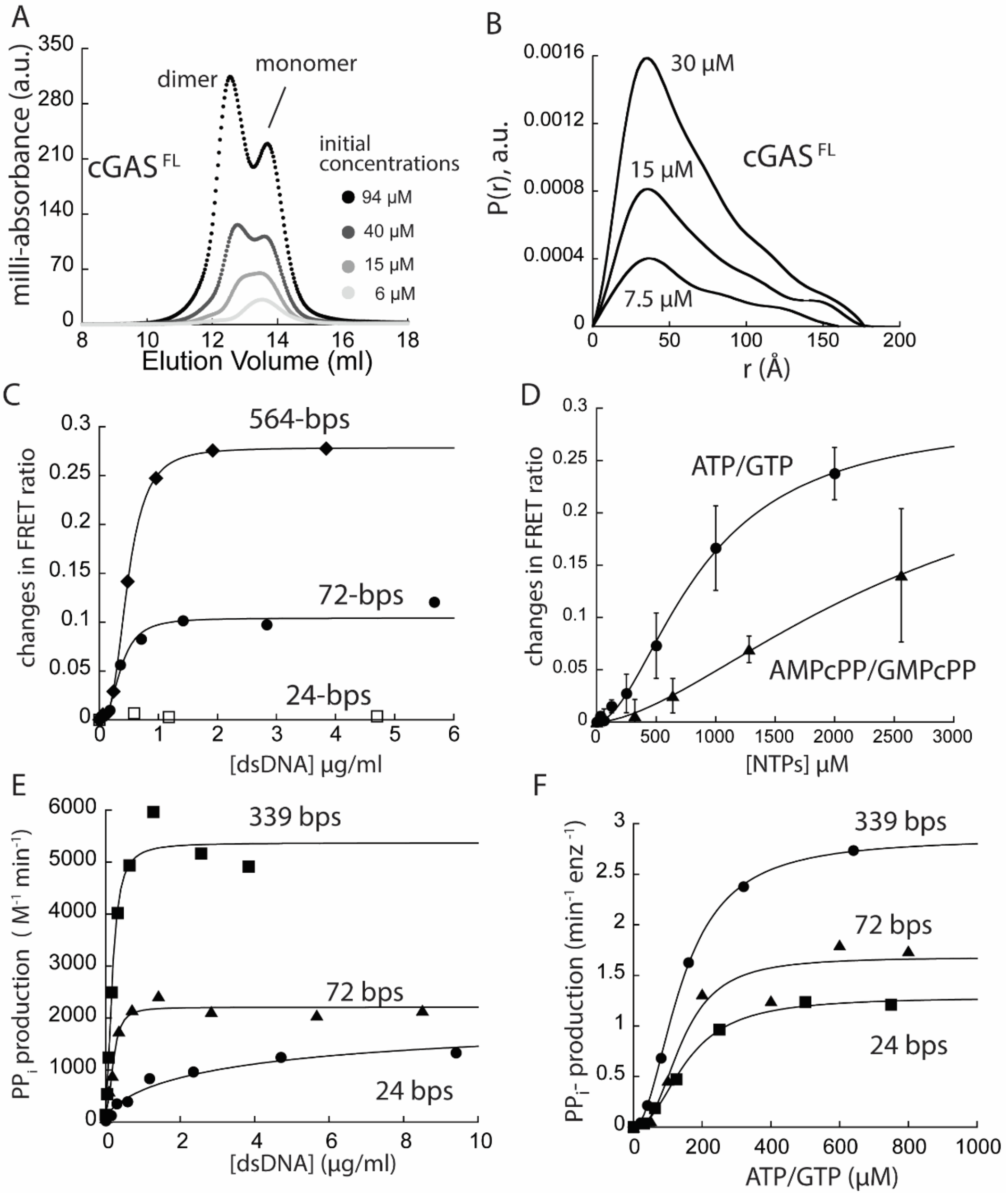

Figure 4. cGAS^{FL} operates within the same allosteric framework as cGAS^{cat}

(A) SEC of cGAS^{FL} (Superdex 200 10/300).

(B) Pair-wise distance distribution function of cGAS^{FL}.

(C) Changes in the ratio between the FRET donor emission (λ_{max}: 578 nm) and the acceptor emission (λ_{max}: 678 nm) of labeled cGAS^{FL} (20 nM each) at indicated dsDNA concentrations.

(D) Changes in the ratio between the FRET donor/acceptor emission ratio of labeled cGAS^{FL} (20 nM each) at indicated NTP pair concentrations.

(E) A plot of the dsDNA concentration-dependent NTase activity of cGAS^{FL} (25 nM) and 800 μM ATP/GTP with various duplex lengths. Lines are fits to a Hill form of the Michaelis-Menten equation.

(F) Substrate dependence of the steady-state rate of NTase activity by cGAS^{FL} (125 nM) with saturating amounts of each dsDNA (6X K_{act}). Lines are fits to a Hill form of the Michaelis-Menten equation.

Figure 4 Supplements 1

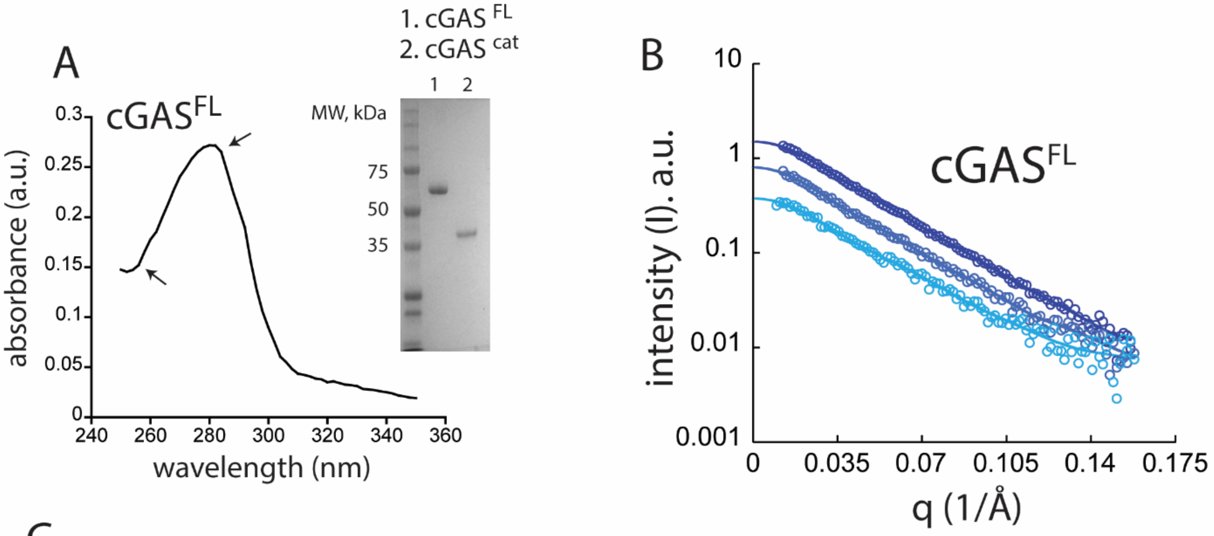

C

protein	method	[ ] (µM)	R_g (Å)$_{primus}$	D_{max}(Å)$_{primus}$	MW_{calc} (kDa)	$MW_{est,avg}$ (kDa)	% dimer
cGAS^{FL}	SAXS	30	50.9 ± 3.2	177	59	121 ± 2	105
cGAS^{FL}	SAXS	15	50.1 ± 4.5	185	59	112 ± 6	90
cGAS^{FL}	SAXS	7.5	45.4 ± 6.7	160	59	88 ± 1	50

(Figure 4 figure supplement 1A) Uv-vis spectra of cGAS^{FL} showing no significant nucleic acid contamination, and SDS-PAGE of cGAS^{cat} and cGAS^{FL}. SDS-PAGE gel shows > 95% pure cGAS^{FL} and cGAS^{cat}.

(Figure 4 figure supplement 1B) SAXS scattering profile of cGAS^{FL}.

(Figure 4 figure supplement 1C) Table summarizing SAXS analyses of cGAS^{FL}.

Figure 4 Supplements 2

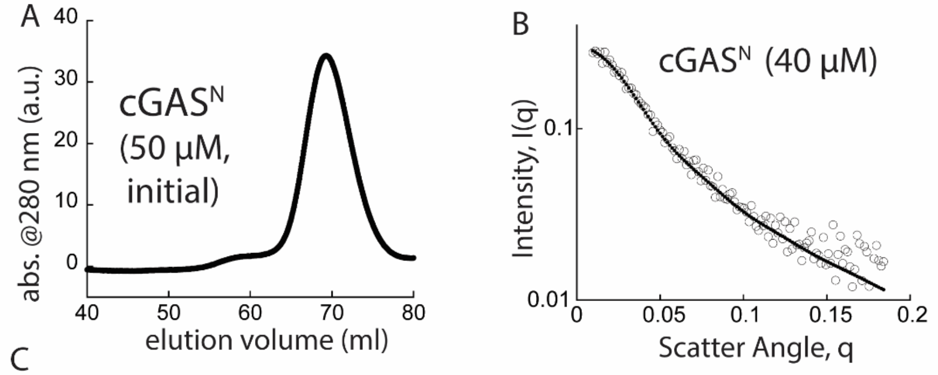

C

protein	method	[ ] (µM)	R_g (Å)$_{primus}$	D_{max}(Å)$_{primus}$	MW_{calc} (kDa)	$MW_{est,avg}$ (kDa)	% dimer
cGAS^N	SAXS	40	43.4	140	16	30.1	94

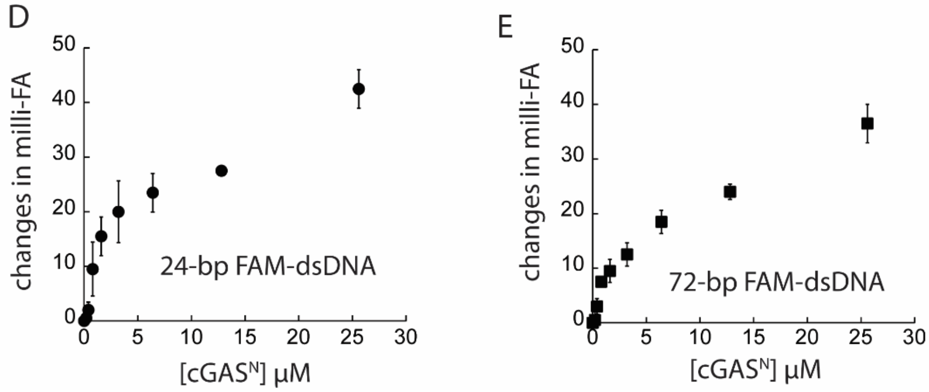

(Figure 4 figure supplement 2A) SEC of cGAS^N (Superdex 75 16/600).

(Figure 4 figure supplement 2B) SAXS scattering profile of cGAS^N.

(Figure 4 figure supplement 2C) Table summarizing SAXS analyses of cGAS^{FL}.

(Figure 4 figure supplement 2D-E) Binding of cGAS^N to each FAM-labeled dsDNA (5 nM) was monitored via FA.

Figure 4 Supplements 3

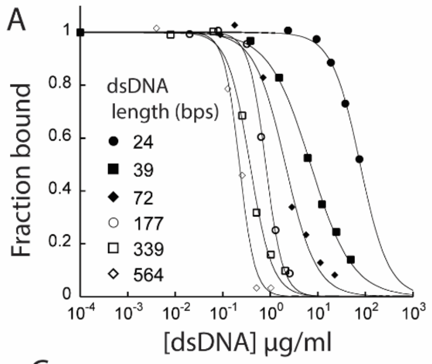

B

dsDNA$_n$ (bps)	ΔFRET	K_{FRET} (μg/ml)	Hill Constant*
24	0.028 ± 0.011	34.83 ± 27.06	1.56 ± 0.59
72	0.147 ± 0.033	0.38 ± 0.04	2.96 ± 0.52
339	0.249 ± 0.026	0.46 ± 0.11	3.66 ± 0.98
564	0.241 ± 0.011	0.63 ± 0.04	4.32 ± 0.24
ATP/GTP	0.284 ± 0.04	909 ± 378 μM	2.16 ± 0.33
ApCpp/GpCpp	0.284*	3360 ± 2206 μM	1.65 ± 0.99

* fixed to be the same as ATP/GTP for estimating K_{FRET}

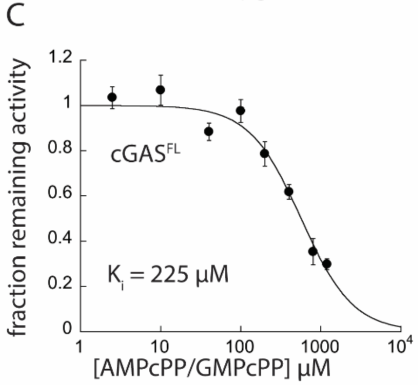

D

dsDNA$_n$ (bps)	M^{-1} min^{-1}	K_{act} (μg/ml)	Hill Constant
0	140 ± 30		
24	2000 ± 800	2.77 ± 1.26	0.99 ± 0.01
72	2500 ± 660	0.22 ± 0.04	1.42 ± 0.28
339	5200 ± 340	0.24 ± 0.05	1.94 ± 0.49
564	6100 ± 1400	0.29 ± 0.11	1.71 ± 0.34

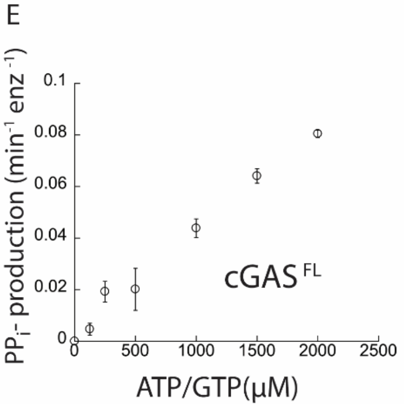

F

dsDNA$_n$ (bps)	k_{cat} (enz^{-1} min^{-1})	K_M (μM)	Hill Constant
24	1.30 ± 0.57	142 ± 6	2.55 ± 0.25
72	1.78 ± 0.11	140 ± 5	2.49 ± 0.06
339	2.90 ± 0.40	116 ± 17	2.34 ± 0.32
564	2.46 ± 0.05	98 ± 11	2.09 ± 0.13

(Figure 4 figure supplement 3A) Competition binding assay using 72-bp FAM-dsDNA (5 nM) and cGAS^{FL} (50 nM) against various dsDNA lengths; the lines are fits to a competition binding equation: $(1/(1+(\text{dsDNAcompetitor})/IC_{50})^{\text{Hill constant}})$.

(Figure 4 figure supplement 3B) Table summarizing the FRET dimerization assay results of cGAS^{FL}.

(Figure 4 figure supplement 3C) Competition activity assay using 339-bp dsDNA (4 μg/ml) and $cGAS^{cat}$ (50 nM) and 150 μM ATP/GTP against increasing concentrations of AMPcPP/GMPcPP; the lines are fits to a competition binding equation: $(1/(1+(\text{competitor})/IC_{50})^{\text{Hill constant}}$. The K_i was calculated using the Cheng-Prusoff equation.

(Figure 4 figure supplement 3D) Table summarizing activation parameters of $cGAS^{FL}$ (25 nM, 800 μM ATP/GTP).

(Figure 4 figure supplement 3E) Steady-state NTase rates of dsDNA free $cGAS^{FL}$ (estimated $k_{cat}/K_M \approx 400\ M^{-1}\ min^{-1}$)

(Figure 4 figure supplement 3F) Table summarizing steady-state kinetic parameters of $cGAS^{FL}$ (125 nM, [dsDNA] = 6 x K_{act}).

Dimerization is required for dsDNA-mediated activation

Although 24-bp dsDNA failed to induce dimerization (Figures 2C and 4C), it activated cGAS to a significant extent (Figures 3C and 4E). Monomeric cGAS can also bind dsDNA, but it is thought to be poorly activated (Andreeva et al. 2017; Li et al. 2013). Moreover, it was proposed that the N-domain enhances the dsDNA binding of monomeric cGAS (Tao et al. 2017), thereby activating the enzyme by lifting the dimerization requirement (Lee et al. 2017). Nonetheless, 24-bp dsDNA bound and activated both cGAS^{cat} and cGAS^{FL} only moderately (Figures 3C and 4E). Thus, our data are most consistent with the allosteric model in which the presence of ATP/GTP increased the dimeric fraction, allowing the short dsDNA to activate cGAS to some extent (Figures 2A-B). To further test this idea, we characterized the activities of a cGAS mutant that binds dsDNA but fails to dimerize, K394E (Li et al. 2013; Zhang et al. 2014); Figure 5A.

Both K394E-cGAS^{cat} and K394E-cGAS^{FL} behaved as single monomeric species in SEC (Figure 5B and Figure 5-figure supplement 1A), consistent with previous reports (Li et al. 2013; Zhang et al. 2014). SAXS and AUC experiments corroborated that K394E-cGAS^{cat} is predominantly monomeric at all tested concentrations (Figure 5-figure supplements 1B-D). Compared to wild-type, not only did K394E-cGAS^{cat} bind dsDNA more weakly, but also without length dependence (Figure 5-figure supplement 2A). The dsDNA length-dependence of K394E-cGAS^{FL} was also less pronounced compared to wild-type cGAS^{FL} (Figure 5-figure supplement 2B-C). We predict that the dsDNA length dependence of K394E-cGAS^{FL} likely arise from the dimerization of the N-domain. Importantly, without dsDNA, K394E-cGAS showed similar activities as wild-type; however, dsDNA failed to stimulate the enzymatic activity of the mutants regardless of duplex length (Figures 5C-F). For instance, dsDNA marginally decreased the K_M of K394E-cGAS, but the k_{cat} did not increase significantly (Figures 5D and 5F). Our results also support the idea that monomeric cGAS can bind substrate and is basally active, yet dimerization is necessary for dsDNA-induced and dsDNA length-dependent activation regardless of the intact N-domain. Furthermore, our observations support the idea that short dsDNA and substrates can synergistically activate cGAS (see also Figure 7 below).

Figure 5

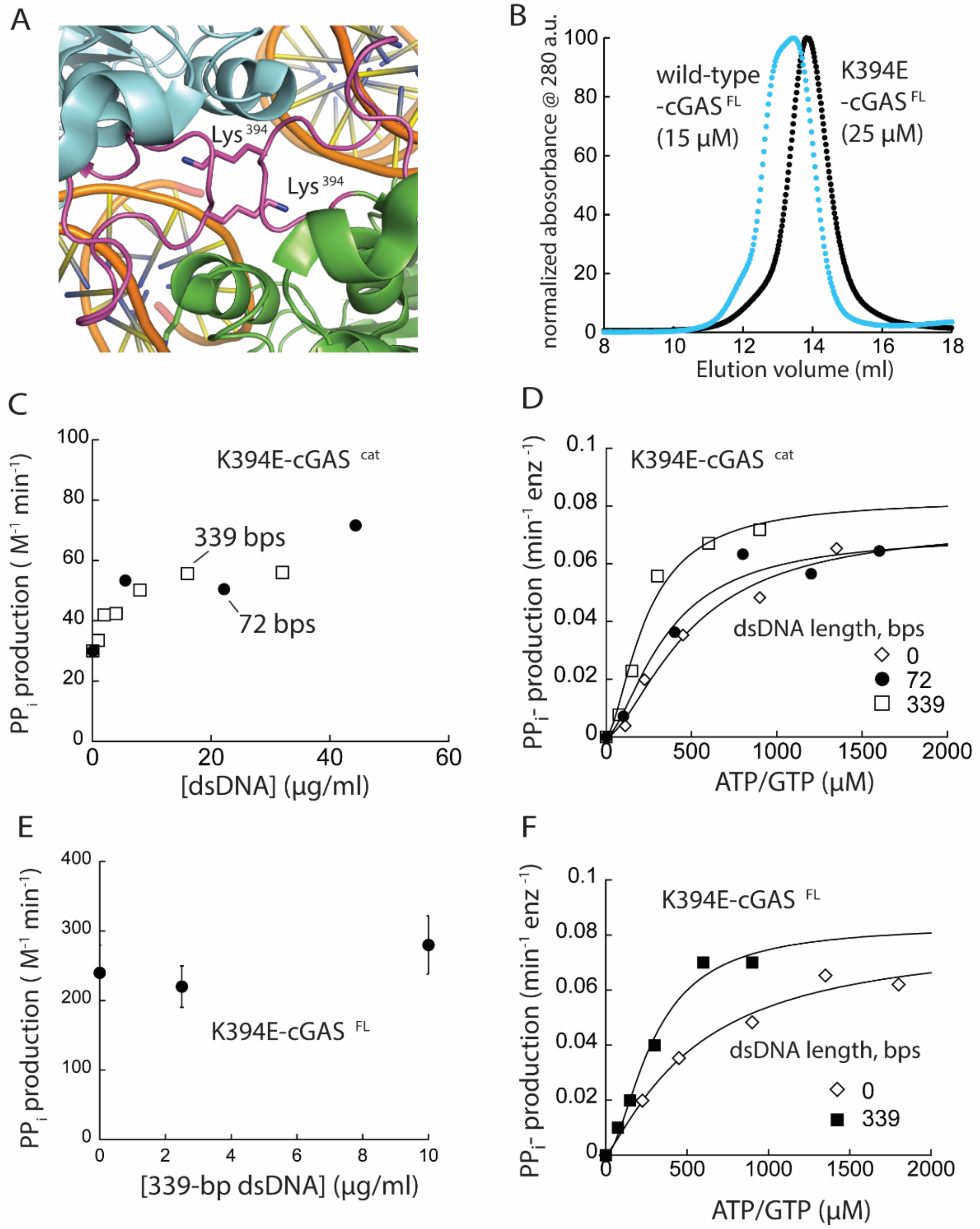

Figure 5. Monomeric cGAS is basally active, but cannot be further activated by dsDNA

(A) Crystal structure of dimeric cGAS^{cat}. The loop important for dimerization is colored in magenta and Lys^{394} is shown in stick representation (PDB ID: 4lez).

(B) SEC (Superdex 200 10/300) of K394E-cGAS^{FL}. WT-cGAS^{FL} is shown for reference (blue).

(C) A plot of the dsDNA-concentration dependent NTase activity of K394E-hcGAS^{cat} (1 μM) and 1 mM ATP/GTP with different duplex lengths.

(D) Substrate dependence of the steady-state rate of NTase activity by K394E-hcGAS^{cat} (1 μM) in the absence or presence of each dsDNA (6X K_{act}). Lines are fits to a Hill form of Michaelis-Menten equation.

(E) A plot of the dsDNA-concentration dependent NTase activity of K394E-cGAS^{FL} (125 nM) and 1 mM ATP/GTP with different duplex lengths.

(F) Substrate dependence of the steady-state rate of NTase activity by K394E-cGAS^{FL} (125 nM) in the absence or presence of each dsDNA (6X K_{act}). Lines are fits to a Hill form of Michaelis-Menten equation.

Figure 5 Supplements 1

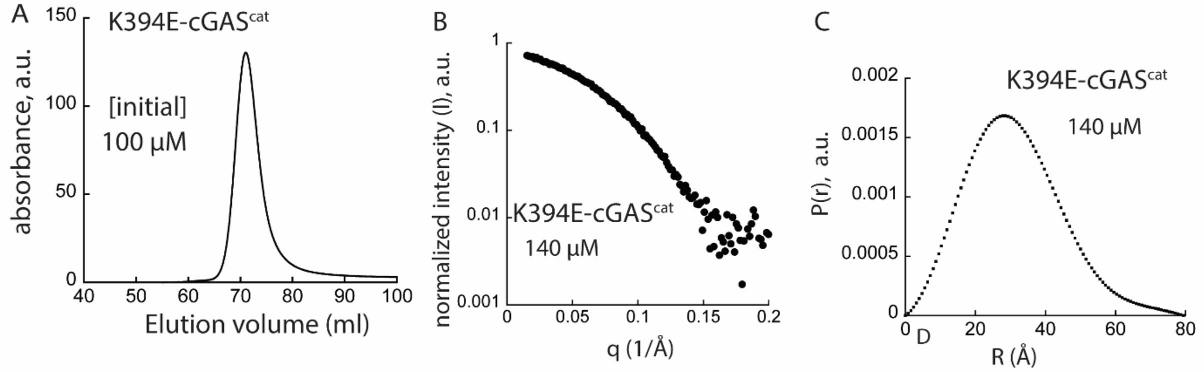

D

protein	method	concentration (μM)	R_g (A)$_{primus}$	D_{max}(A) primus	$MW_{est,avg}$	% dimer
K394E-cGAS^{cat}	SAXS	140	23.8 ± 0.1	80	48.7 ± 4.6	< 5%
K394E-cGAS^{cat}	SAXS	70	24.2 ± 0.2	80	48.2 ± 2.2	< 5%
K394E-cGAS^{cat}	SAXS	35	21.1 ± 0.3	83	47.6 ± 2.5	< 5%

$MW_{est,avg}$ is the average MW estimate determined from datporod, MoW2 and OLIGOMER.

(Figure 5 figure supplement 1A) SEC of K394E-cGAS^{cat} (Superdex75 16/600).

(Figure 5 figure supplement 1B) SAXS scattering profile of K394E-cGAS^{cat}.

(Figure 5 figure supplement 1C) Pair-wise distance distribution function calculated from Figure 5 figure supplement 1B.

(Figure 5 figure supplement 1D) Table summarizing SAXS analyses of K394E-cGAS^{cat}

Figure 5 Supplements 2

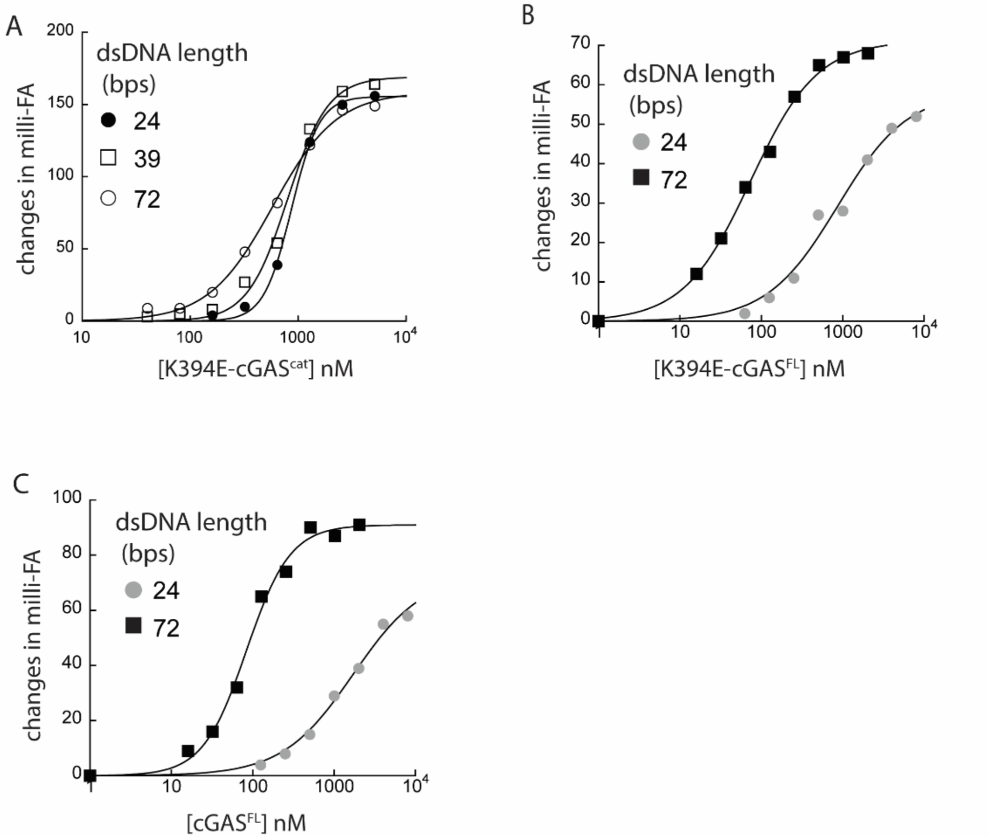

(Figure 5 figure supplement 2A) Binding of K394E-cGAS^{cat} to each FAM-labeled dsDNA (5 nM) was determined by FA. The lines are fits to a standard binding isotherm.

(Figure 5 figure supplement 2B) Binding of K394E-cGAS^{FL} to each FAM-labeled dsDNA (5 nM) was determined by fluorescence anisotropy (FA). The lines are fits to a standard binding isotherm.

(Figure 5 figure supplement 2C) Binding of cGAS^{FL} to each FAM-labeled dsDNA (5 nM) was determined by fluorescence anisotropy (FA). The lines are fits to a standard binding isotherm.

cGAS dimers arrange randomly on dsDNA

cGAS dimers are thought to form a ladder-like array along the length of dsDNA to maximize the stability of its signaling complex (Andreeva et al. 2017). Given that both cGAS monomers and dimers bind dsDNA (Andreeva et al. 2017; Li et al. 2013), our results are better explained by a simpler mechanism in which dsDNA length regulates the fraction of cGAS dimers without requiring an ordered structure beyond the dimeric unit (Figures 2A-B). To further test this idea, we imaged cGAS^{cat} and cGAS^{FL} with dsDNA using nsEM (Figure 6; see also Figure 6- figure supplement 1 for zoom-in images, and additional images in figure 6- figure supplement 2). When proteins were in excess over dsDNA, we observed large clusters likely reflecting multiple cGAS dimers binding to several different dsDNA strands (Figure 6A and 6E). It is possible that these clusters reflect the recently observed phase-shifting condensates of cGAS•dsDNA (Du and Chen 2018a). With excess dsDNA over protein, which more likely resembles *in vivo* events when dsDNA breaches the cytoplasm, it appeared that cGAS dimers randomly decorated dsDNA (Figures 6B and 6F), with the particle sizes corresponding to the dimeric species of cGAS^{cat} and cGAS^{FL}, respectively (i.e. the D_{max} for these constructs are ~10 and 18 nm, respectively; Figure 1). Importantly, the ladder-like arrangement of cGAS particles was rare for both cGAS^{cat} and cGAS^{FL} (Figure 6B and F, Figure 6-figure supplement 2D-E), suggesting that cGAS•dsDNA does not form an ordered supra-structure.

On the other hand, the size of particles resulting from excess K394E-cGAS^{cat} with dsDNA appeared smaller and corresponded to the D_{max} of cGAS monomers (Figure 6C; see also Figure 5-figure supplement 1), likely reflecting monomeric cGAS randomly bound on dsDNA. For K394E-cGAS^{FL}, we observed dsDNA-bound clusters somewhat similar to wild-type (these clusters are likely mediated by the intact N-domain that promotes dimerization). However, the clusters were not as expansive as those formed by wild-type (Figure 6E vs. G). Moreover, we did not observe any significant decoration of dsDNA when the K394E mutants were present in sub-stoichiometric amounts (Figures 6D and 6H; the particle size observed in Figure 6H also corresponds to the monomeric full-length cGAS). Overall our nsEM experiments support the allosteric framework of cGAS (Figure 2A-B) in which the role of dsDNA length is to simply bias the fraction of active dimers without necessitating supramolecular assemblies. Nevertheless, given the intrinsic, low-resolution imaging of nsEM, future structural studies are warranted to more fully understand the nature of these cGAS•DNA macromolecular complexes.

Figure 6

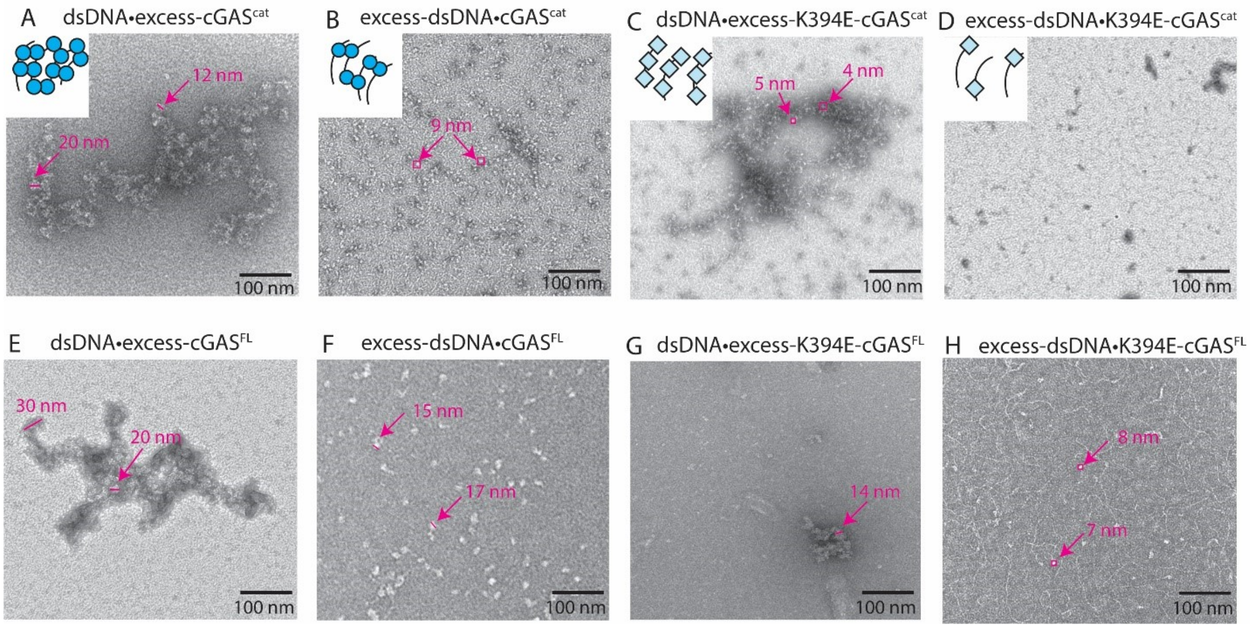

Figure 6. cGAS dimers assume various configurations on dsDNA

Negative-stain electron micrographs of cGAS•dsDNA complexes. (A, E) 3-fold excess cGAS over dsDNA, (B, F) 3-fold excess dsDNA over cGAS, (C, G) 3-fold excess K349E-cGAS over dsDNA, (D, H) 3-fold excess dsDNA over K394E-cGAS. Ratios of protein to dsDNA or dsDNA to protein are binding site normalized; 18 bp per binding site. The particle sizes in B and F are consistent with the D$_{max}$ of cGAS^{cat} and cGAS^{FL}, respectively (Figures 1 and 4). Particle sizes in C and H are consistent with the D$_{max}$ of K394E-cGAS variants (Figure 5-figure supplement 1).

Figure 6 supplement 1

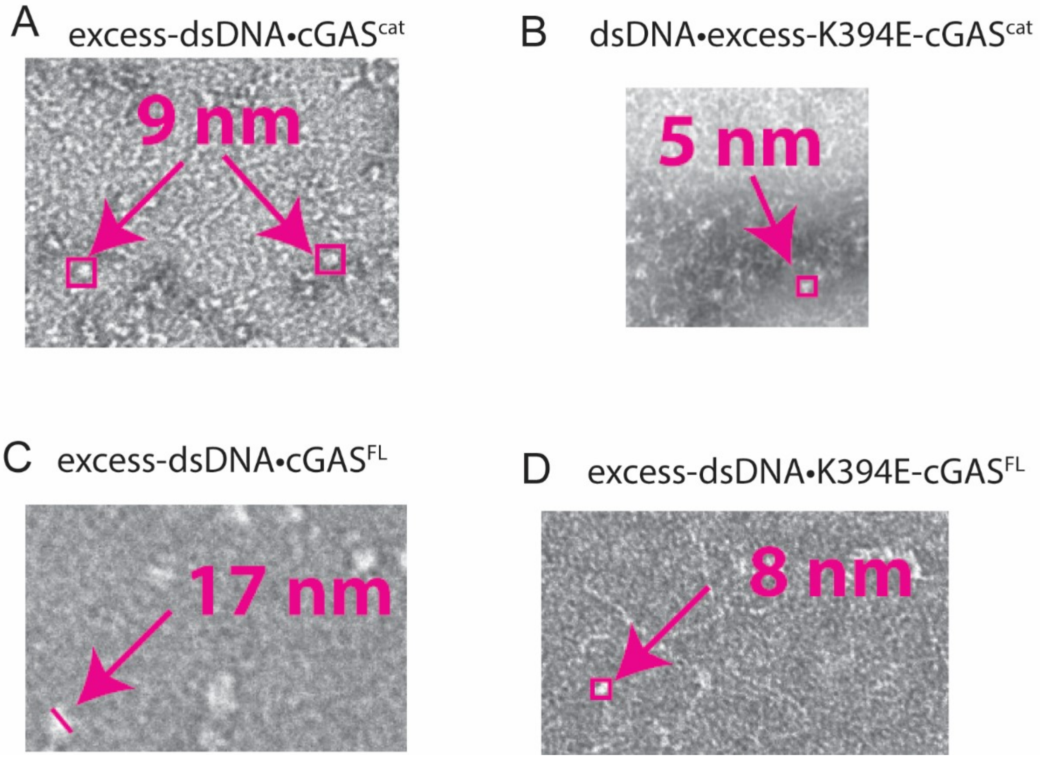

(Figure 6 figure supplement 1A-E) Zoomed-in images from Figures 6B, C, F, and H showing the measured particles.

Figure 6 supplement 2

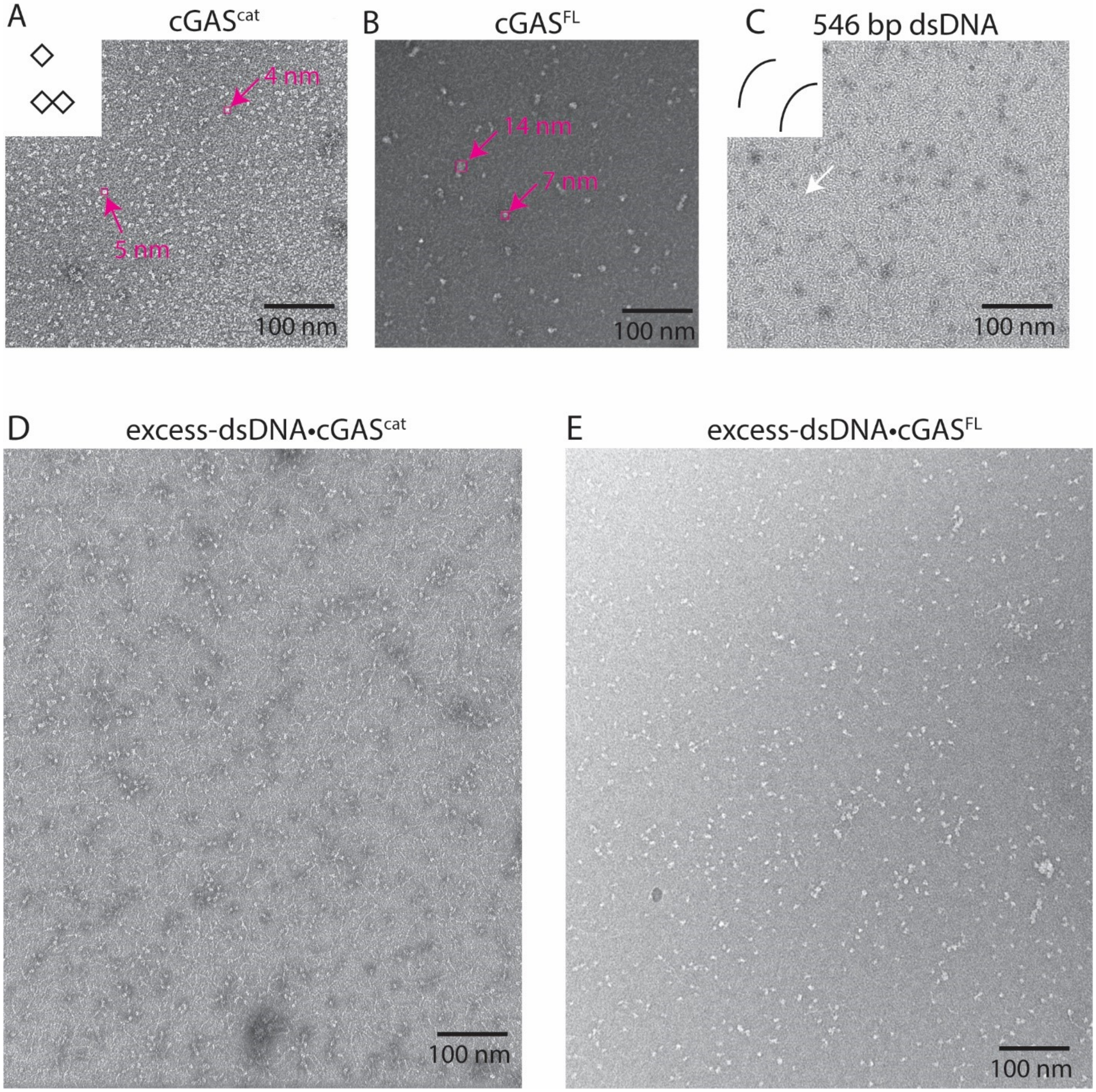

(Figure 6 figure supplement 2A-E) Additional negative-stain electron micrograph images.

The context-dependent, allosteric activation of cGAS

It was initially proposed that dsDNA length does not play a significant role in regulating the activation of cGAS (Gao, Ascano, et al. 2013; Kranzusch et al. 2013; Li et al. 2013); however, two recent studies have contested this model (Andreeva et al. 2017; Luecke et al. 2017b). The reason for this discrepancy is still unclear. Our results suggest that raising enzyme and substrate concentrations will increase the dimeric fraction of cGAS, while binding of short dsDNA will not (e.g. 24-bp). Given the vastly different cGAS and substrate concentrations used in previous studies (Gao, Ascano, et al. 2013; Kranzusch et al. 2013; Li et al. 2013; Andreeva et al. 2017; Luecke et al. 2017b), we speculated that the apparent or lack of dsDNA length-dependence is caused by the fraction of cGAS dimers formed without dsDNA (Figure 2A). To test this idea, we monitored the steady-state NTase activity of cGAS^{cat} and cGAS^{FL} with saturating amounts of various dsDNA lengths and a permutation of high and low concentrations of enzyme and ATP/GTP (Figure 7A-D). Increasing substrate and enzyme concentrations did not eliminate the need for dsDNA. However, the dependence on dsDNA length progressively decreased with increasing protein and substrate concentrations. For instance, with low cGAS^{cat} and sub-K_M ATP/GTP concentrations (cGAS is predominantly monomeric), we observed strong dsDNA length-dependent activities, with a difference of 8-fold between 24-bp and 564-bp dsDNA (Figure 7A). With low cGAS and high ATP/GTP, the difference between short and long dsDNA was 4-fold (Figure 7B). With high cGAS and low ATP/GTP, the difference was again reduced to 2.5-fold (Figure 7C). Finally, with high cGAS^{cat} and high ATP/GTP (the dimer population is significant), the differential activity caused by various dsDNA lengths was merely 1.5-fold, with short dsDNA molecules robustly activating cGAS^{cat} (Figure 7D). Furthermore, we observed the same trend from cGAS^{FL} except the effect of raising substrate and enzyme concentrations was more pronounced than cGAS^{cat} (Figure

7-figure supplement 1). These observations uncover the reason for conflicting observations regarding dsDNA length-dependence (Andreeva et al. 2017; Li et al. 2013; Kranzusch et al. 2013; Luecke et al. 2017b). That is, the dependence on dsDNA length can either manifest or diminish by different reaction contexts that dictate the fraction of dsDNA-free cGAS dimers. Our results in turn indicate that cGAS is primed to generate a graded signaling output depending on the overall reaction condition (e.g. the length of cytoplasmic dsDNA, cGAS expression level, and available ATP/GTP), providing a molecular framework for its context-dependent and diverse stress responses (Gulen et al. 2017; Larkin et al. 2017; Li and Chen 2018; Li et al. 2016; Tang et al. 2016)

Figure 7

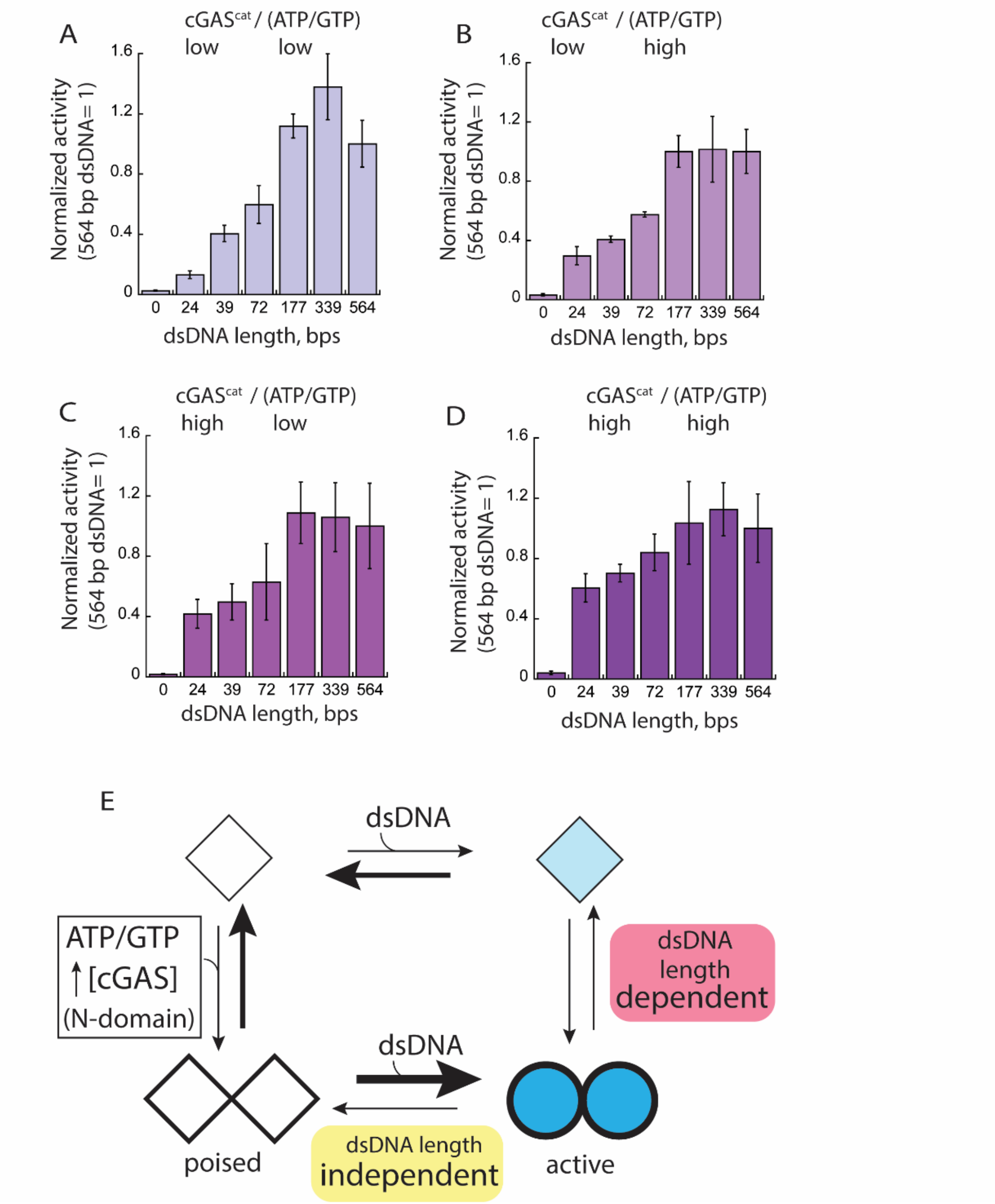

Figure 7. Context-dependent activation of cGAS

(A-D) Plots of the NTase activity of cGAS^{cat} vs. dsDNA length (6X-K$_{act}$) at various enzyme and substrate concentrations (low cGAS: 50 nM, High cGAS: 1 µM; low ATP/GTP: 250 µM, high ATP/GTP: 6X-K$_M$ for each dsDNA). The NTase activity of cGAS^{cat} induced by 564-bp dsDNA was normalized by enzyme and substrate concentrations, and used as the reference to calculate the fraction activity for each dsDNA length (*n* = 3; ± SD).

(E) The equilibrium-based activation model of cGAS. Diamonds represent basally active cGAS and circles indicate active cGAS. Filled shapes and thicker lines indicate dsDNA binding and substrate binding, respectively. Thicker lines and darker shades indicate stronger interactions.

Figure 7 Supplements 1

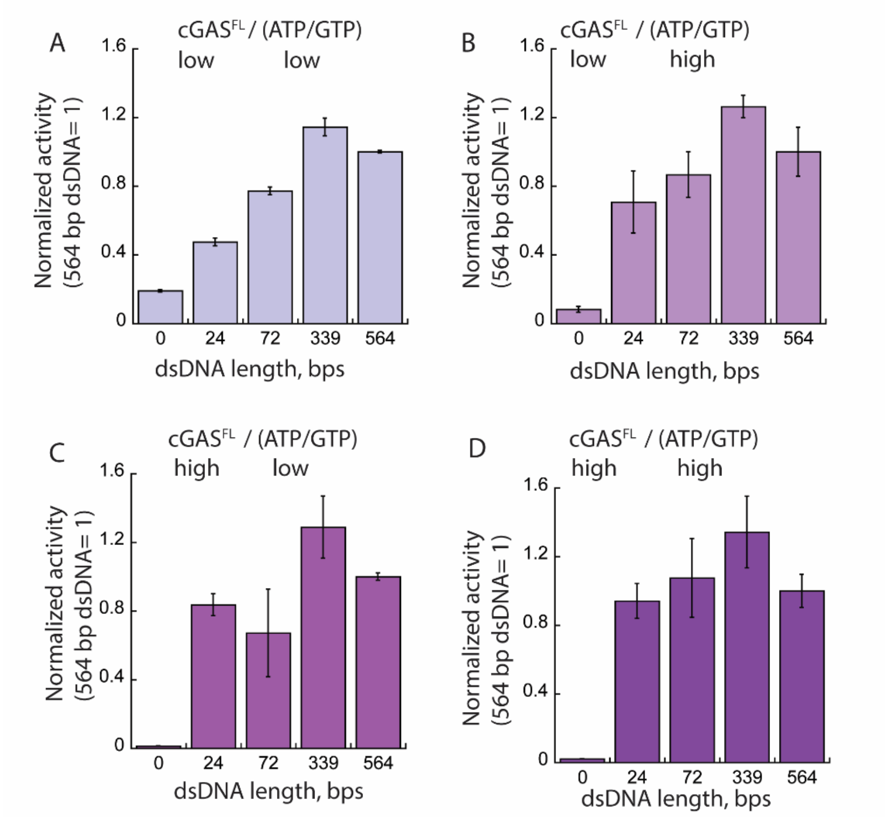

(Figure 7 figure supplement 1A-D) Plots of the NTase activity of $cGAS^{FL}$ vs. dsDNA length (6X-K_{act}) at various enzyme and substrate concentrations (low cGAS: 25 nM, High cGAS: 1 µM; low ATP/GTP: 150 µM, high ATP/GTP: 6X-K_M for each dsDNA). The NTase activity of $cGAS^{FL}$ induced by 564-bp dsDNA was normalized by enzyme and substrate concentrations, and used as the reference to calculate the fraction activity for each dsDNA length (*n* = 3; ± SD).

Discussion

The activation of IFN-1 leads to diverse stress responses (antiviral gene expression, cellular senescence, autophagy, or apoptosis; (Gulen et al. 2017; Larkin et al. 2017; Li and Chen 2018; Li et al. 2016; Tang et al. 2016; Liang et al. 2014; Yang et al. 2017)). cGAS contributes significantly to this complex signaling landscape by generating variable amounts of cGAMP (Li and Chen 2018). Here, building upon the framework shown in Figure 2A, we set forth a unifying allosteric activation mechanism of cGAS, which explains how this cytoplasmic dsDNA sensor could dynamically tune its signaling activity in a switch-like fashion according to reaction (cellular) contexts (Figure 7E). In this model, cGAS is subject to an intrinsic, monomer-dimer equilibrium, with its N-domain potentiating the dimerization propensity. dsDNA can drive the monomer-dimer equilibrium toward the dimeric state, with duplex length determining the fraction of active dimers (Figure 7E upper right-hand path). Importantly, given the active unit of cGAS is a dimer, we propose that longer dsDNA simply increases the probability of forming dimers without invoking an ordered configuration. We also find here that cGAS allosterically couples its dimeric population to factors other than dsDNA, such as cGAS expression level and ATP/GTP availability (Figure 7E, left path). We propose that this coupling mechanism would allow the dimer population to be in constant flux, providing a molecular framework for its dynamic signaling activity. Indeed, cGAS is subject to overexpression by multiple factors including its downstream product IFN-1 (Ma et al. 2015). Intracellular ATP/GTP concentrations also vary depending on cell age, cell-cycle progression, and stress conditions (Traut 1994; Huang, Zhang, and Chen 2003; Corton, Gillespie, and Hardie 1994; Wang et al. 2003; Marcussen and Larsen 1996). Moreover, post-translational modification (e.g. mono-ubiquitination) promotes dimerization of cGAS (Seo et al. 2018). Of note, given that pathogen infection increases host NTP levels (Ogawa et al. 2015; Chang et al. 2009), it is tempting to speculate that cGAS takes advantage of the higher intracellular NTP levels to increase its dimer population, potentiating its activation. Importantly, increasing the dimeric fraction in the absence of dsDNA would not elicit significant spurious activity, but would instead prime the enzyme for facile activation by reducing the dependence on dsDNA length (Figure 7E lower left-hand corner). Another key feature of our equilibrium-based allosteric model is that dsDNA length-dependence is conditional, reconciling conflicting claims regarding the dependence on dsDNA length in activating cGAS (Andreeva et al. 2017; Gao, Ascano, et al. 2013; Kranzusch et al. 2013; Li et al. 2013; Luecke et al. 2017b; Zhang et al. 2014).

Molecular framework for the dsDNA length-dependent response of cGAS

As the initial receptor in a major inflammatory signaling pathway (Chen, Sun, and Chen 2016), it is critical for cGAS to possess a very stringent noise filtering mechanism. Although cGAS binds dsDNA in a sequence-independent manner (Gao, Ascano, et al. 2013; Li et al. 2013; Zhang et al. 2014), it uses dsDNA length to distinguish signal from noise (Andreeva et al. 2017; Luecke et al. 2017b). After all, dsDNAs arising from catastrophic conditions are significantly longer than 300 bps (e.g. mitochondrial, chromosomal, and viral dsDNA), while short dsDNAs likely indicate minor genome repair and/or resolution of infection (i.e. the viral genome has been degraded). Here, we find that the allosteric coupling mechanism allows cGAS to generate a two-stage noise filter against short dsDNA. For instance, as others have reported (Andreeva et al., 2017), we recapitulate here that cGAS binds and dimerizes on dsDNA in a length-dependent manner. We also found that dsDNA length-dependent dimerization and binding *in vitro* only gradually changes (Figures 2-4; (Andreeva et al., 2017)). However, dsDNA length also grades the enzymatic activity of cGAS (Figures 3-4). Thus, combined with the length-dependent complex formation of cGAS dimers (signal recognition), the length-dependent enzymatic activity (signal transduction) would allow cGAS to further differentiate correct pathogenic dsDNA from noise (short dsDNA). Of note, given that dsDNA length-dependence subsides with high concentrations of cGAS, our new model also provides an avenue for how improper clearance of pathogenic or self-dsDNA can induce spurious activity of cGAS leading to auto-inflammatory conditions (Gao et al. 2015; Li and Chen 2018).

The role of cooperativity in initiating and terminating the cGAS pathway

The interactions between cGAS and its ligands (dsDNA and ATP/GTP) display positive cooperativity, a hallmark of allosteric enzymes (Figures 2-4). One key feature of a cooperative system is its capacity to amplify and attenuate the output in a switch-like manner (Sohn and Sauer 2009; Monod, Wyman, and Changeux 1965). For instance, when the concentrations of cGAS, dsDNA, and ATP/GTP change by a factor of two, a non-cooperative system would yield a total 8-fold increase in output (2x2x2 = 8). However, because cGAS requires dimerization for activity and displays a Hill constant near two in its interaction with both dsDNA and ATP/GTP, the same two-fold change would be further amplified by the exponent of two, leading to a 64-fold amplification in output ($2^2 x 2^2 x 2^2 = 64$). Conversely, the same cooperative mechanism would allow cGAS to attenuate its signaling output by the same magnitude with decreasing enzyme and ligand concentrations. Together with the dsDNA-length dependent activity, the cooperativity would enable cGAS to dramatically alter its output according to the changes in input parameters, allowing the initial receptor to dynamically regulate its signaling pathway in a switch-like manner.

The role of N-domain and human vs. mouse cGAS

Although cGAS^{cat} is sufficient to bind dsDNA and generate cGAMP *in vitro*, the intact N-domain is crucial for augmenting its function in cells (Tao et al. 2017; Wang, Ning, et al. 2017). It has been presumed that the major role of the N-domain is to enhance dsDNA binding (Lee et al. 2017; Tao et al. 2017). Furthermore, it was proposed that the N-domain promotes the activation of monomeric mouse cGAS by dsDNA (Lee et al. 2017). Here, we found that N-domain potentiates the dimerization of cGAS. Our results also indicate that dimerization is necessary for dsDNA-mediated activation by both cGAS^{cat} and cGAS^{FL} (Figure 5). It is possible that mouse cGAS operates in a different mechanism than human cGAS. Indeed, it was recently proposed that mouse-cGAS would not depend on dsDNA length as much as human-cGAS for activation, as the former binds short dsDNA more tightly (Zhou et al. 2018). However, it was previously shown that both human and mouse-cGAS exhibit similar dsDNA length dependent activation (Andreeva et al. 2017). Considering that dsDNA-mediated dimerization is critical for both human and mouse cGAS variants for activation (Andreeva et al. 2017; Li et al. 2013; Zhang et al. 2014; Zhou et al. 2018), we propose that our findings are likely general phenomena across different species, and different intrinsic affinity constants caused by diverse primary sequences (Zhou et al. 2018) would dictate species-specific experimental observations.

Comparison with other nucleic acid sensors

Absent-in-melanoma-2 (AIM2) is another major cytoplasmic dsDNA sensor in mammals (Fernandes-Alnemri et al. 2009; Hornung et al. 2009; Roberts et al. 2009). The single most important goal of the AIM2-mediated dsDNA sensing pathway is to induce cell-death, a digital (not tunable) process that does not require a new equilibrium (Liu et al. 2014; Roberts et al. 2009). Indeed, once assembled on dsDNA, the AIM2 inflammasome does not disassemble and multiple positive feedback loops reinforce the assembly, consequently generating a binary signaling response (Matyszewski, Morrone, and Sohn 2018). By contrast, the cGAS signaling pathway elicits various stress-responses ranging from viral replication restriction to apoptosis, with the signal strength and cellular contexts determining the type of outcome (Gulen et al. 2017; Larkin et al. 2017; Li and Chen 2018; Li et al. 2016; Tang et al. 2016; Liang et al. 2014; Yang et al. 2017). Unlike AIM2, we find here that cGAS can dial its own activity (tunable), providing a molecular framework for eliciting various cGAMP-dependent outcomes. Furthermore, although both AIM2 and cGAS are activated in a dsDNA length-dependent manner, the former assembles into filaments (Matyszewski, Morrone, and Sohn 2018; Morrone et al. 2015), while the latter only requires dimerization. Likewise, although cytoplasmic dsRNA sensors preferentially target long duplexes (> 500 bps), MDA5 assembles into filaments while RIG-I does not require polymerization for activation (Sohn and Hur 2016; Linehan et al. 2018; Peisley et al. 2011; Ramanathan et al. 2016; Peisley et al. 2013). Thus, we propose that the assembly of supra-structures is not universal to host nucleic acid sensors. Rather, it appears that each sensor has evolved unique mechanisms to utilize the length of nucleic acids as a molecular ruler to distinguish self (noise) from nonself (signal).

Extended discussion

Not surprisingly, human and mouse cGAS share many structural and functional properties. Based on sequence alone, the catalytic domain is >65% identical, while the N-terminal extension is less conserved (<25%). Both proteins share a nucleotidyl transferase fold and a flexible N-terminal extension. From a functional perspective, human and mouse cGAS are the primary drivers of interferon signaling in cells when challenged by microbes, viruses or dsDNA. Both require dsDNA for activation, and, when activated, they perform two, sequential nucleotidyl transfer reactions to create cGAMP from ATP and GTP. Lastly, both homologs inherently discriminate against stimulatory dsDNAs based on length, albeit to different extents, at least in vitro. No direct comparison has/can be made in cells.

Despite their similarities, human and mouse cGAS appear to achieve the same end goal through slightly different means. Human cGAS can dimerize in the absence of dsDNA, while mouse cGAS appears to do so only in the crystalline state. Mouse cGAS binds more tightly to short dsDNA and is more active when bound to short dsDNA. Lastly, mouse cGAS is significantly more efficient with respect to NTase activity relative to human cGAS. This phenomenon is primarily manifested by relatively tighter functional binding of substrates and an elevated k_{cat} (Zhou et al. 2018).

Crystal structures of human* and mouse cGAS in the presence and absence of dsDNA have been solved. All crystallographic forms of cGAS are dimeric, enabling an accurate molecular comparison of the two homologs. Close inspection of the dimerization interface reveals a potential clue as to why human cGAS dimerizes more efficiently than mouse cGAS. The loop sandwiched between the dimeric interface and Zn-binding motif, residues N399-E402 (human), referred to as the bridging loop hereafter, is noticeably dissimilar between human and mouse cGAS (Figure). Notably, the human loop orients the acidic side chain of E402 to point towards K392. This electrostatic interaction is not capable of forming in the mouse dimer due to the different loop conformer preference and residue substitutions at both E402 and K392 (A390 and I380 in mouse, respectively). Moreover, symmetry at the dimerization interface implies that the additional electrostatic interaction occurs twice, thereby doubling the energy contribution towards dimerization.

Multiple studies have shown that mcGAS turns over significantly faster than hcGAS (20 min^{-1} vs 2 min^{-1}). The molecular mechanism for this remains uncertain, but the determinants for this effect appear to hinge, at least, on two key residues, K187 and L195 (human). Curiously, the residues are within the primary dsDNA binding site on the spine helix. Authors of the study claim that the mouse residues, N for K187 and R for L195, enhance DNA binding affinity for short dsDNA while negligibly affecting the binding affinity for long dsDNA. This implies then that the human residues polarize the hcGAS response to favor activation by long dsDNA. However, this model seemingly contradicts published data showing that both mcGAS and hcGAS respond in a dsDNA-length dependent manner in cells. Moreover, the authors did not explain how an increase in dsDNA binding affinity could result in dramatically faster catalytic rates. One possibility is that the residues within the spine helix dictate how the grooves of dsDNA orient within the dsDNA binding site. Shifting the register of the DNA, i.e. location of the major and minor groove, may influence how dsDNA effectively promotes the necessary conformational change at the active site, e.g. ordering the activation loop. It is worth noting that the adjacent dsDNA binding site on the second protomer, site B, may also influence the dsDNA binding register, and that mcGAS and hcGAS also differ in primary sequence at this location. Additional experimentation, perhaps through mutagenesis, is necessary to test these hypotheses.

All structures have captured cGAS in the dimeric state. Thus, it remains unclear if the crystalline form of cGAS biases the conformation of key structural features, such as the bridging loop. If the bridging loop of apo, monomeric cGAS can adopt alternative conformations, this would indicate that dsDNA binding and dimerization are also linked by the bridging loop. Evidence for this is seen from a mutant that disrupts the adjacent Zn-binding motif. The mutant phenocopies the dimerization-null mutant K394E, suggesting that, in addition to disrupting dsDNA contacts, the Zn-binding mutant lacks the structural integrity to dimerize; the Zn-binding motif constrains the bridging loop, potentiating the conformer required for dimerization.

In closing, our study reconciles the conflicting views on the roles of dsDNA length and the N-domain in activating cGAS. We also provide a mechanistic framework for understanding how cGAS can shape a complex signaling landscape depending on cellular reaction contexts. Future studies will be directed in understanding how this dynamic enzyme operates in conjunction with its downstream and regulatory components to regulate host innate immune responses against cytoplasmic dsDNA.

Materials and Methods

Reagents

dsDNA substrates and oligonucleotides shorter than 100 bps were purchased from Integrated DNA Technologies (IDT). Longer dsDNAs (≥ 150 bps) were generated by PCR. The human cGAS cDNA was kindly provided by Dr. Dinshaw Patel. *E. coli* pyrophosphatase was a gift from Dr. James Stivers. The SortaseA (SortA) enzyme was a gift from Dr. Hidde Ploegh. Purity and length of each dsDNA was confirmed by agarose gel electrophoresis. TAMRA- and Cy5-labeled peptides were purchased from Lifetein. ATP and GTP were purchased from Sigma. GMPcPP and AMPcPP were purchased from Jena Biosciences

Recombinant cGAS purification

Protein preparation. Recombinant cGAS constructs were cloned into the pET28b vector (Novagen) with an N-terminal 6xHis-MBP-tag and a TEV protease cleavage site. Proteins were expressed using 200 μM IPTG at 16°C for overnight in *E. coli* BL21 Rosetta 2. Cells were lysed in Buffer A by sonication (Buffer A: 25mM Tris HCl pH 7.5, 1mM DTT, 5% glycerol, 500mM NaCl, PMSF, lysozyme, benzamidine, DNaseI). Clarified lysate was applied to amylose resin, and then washed with 4CV of Buffer B before eluting with Buffer B supplemented with maltose (Buffer B: 25mM Tris HCl pH 7.5, 1mM DTT, 5% glycerol, 500mM NaCl). The eluted fraction was dialyzed with TEV protease overnight at 4°C in buffer containing 25mM Tris HCl pH 7.5, 125mM NaCl, 10mM β-ME. After dialysis, the dialysate was adjusted to include 5% glycerol and supplemented to 300mM NaCl (Buffer C). Recombinant cGAS constructs were then bound to heparin resin (GE Healthcare), washed extensively and flash eluted with Buffer C supplemented to 800mM NaCl. The eluted fractions were applied to a Superdex 75 16/60 (cGAS^{cat} and cGAS^{NT}) or Superdex 200 16/60 (cGAS^{FL}) in buffer containing 25mM Tris HCl, 300mM NaCl, 1mM DTT and 2% glycerol (Buffer D). Monomer and dimer peaks were combined and applied to amylose resin to remove residual, uncleaved protein. The flow through was concentrated then frozen and stored at -80°C in buffer containing 20 mM Tris HCl at pH 7.5, 300 mM NaCl, 10% glycerol, 5 mM DTT. The preparation of cGAS for sortase A labeling was performed as above, with the following exceptions: clarified lysate was applied to amylose, washed, and eluted then applied to Ni-NTA, then washed and eluted. The elutions were applied to a Superdex 200 16/60, and the recombinant cGAS fractions were concentrated, frozen and stored in at -80°C. Mutagenesis was confirmed by sequencing.

Fluorophore labeling. The labeling procedure was adapted from (Guimaraes et al. 2013). 20 μM MBP-TEV-cGAS-LPETGG-6xHis was incubated with 30 μM SortA, 250 μM fluorophore-peptide in Sortase reaction buffer (50mM Tris HCl pH 7.5, 150 mM NaCl, 10 mM $CaCl_2$, 5% glycerol, 2 mM DTT) at 25 ± 2 °C for 3 hrs on a rotator. Reactions were directly applied to

Superdex 200 10/300 GL (20 mM Tris HCl pH 8.0, 300 mM NaCl, 2% glycerol, 10 mM BME). Fractions containing cGAS were applied to Ni-NTA. Flow-through was applied to heparin resin and washed with Sizing Buffer (Buffer D). Protein was eluted with Sizing buffer supplemented with 600 mM NaCl. Eluted fractions were adjusted to 20 mM Tris HCl pH 7.5, 300 mM NaCl, 10 % glycerol, 5 mM DTT and concentrated.

Biochemical Assays

All experiments were performed at least three times. The fits to data were generated using Kaleidagraph (synergy). Reported values are averages of at least three independent experiments and reported errors are standard deviations. All reactions were performed under 25 mM Tris acetate pH 7.4, 125 mM potassium acetate pH 7.4, 2 mM DTT, 5 mM $Mg(acetate)_2$ pH 7.4, and 5% glycerol at 25 ± 2 °C.

dsDNA binding assays. Increasing concentrations of cGAS were added to a fixed concentration of fluorescein-amidite-labeled (FAM) dsDNA (5-10 nM final). Changes in fluorescence anisotropy were plotted as a function of cGAS concentration and fit to the Hill equation. For competition-based experiments, unlabeled dsDNA was titrated against a fixed population of FAM-$dsDNA_{72}$ and cGAS ([protein] = $K_{D,dsDNA72}$). Changes in fluorescence anisotropy (FA) was plotted against competitor dsDNA concentration and fit to yield IC_{50}s.

FRET-based oligomerization assays. 60 nM Cy5- and TAMRA-labeled MBP-TEV-cGAS-LPET-GGGQC/K-fluorophore were incubated with TEV protease in cGAS reaction buffer at 25 ± 2 °C for 2 hrs. Increasing amounts of dsDNAs of different lengths or equimolar concentrations of nucleotides were added to 20 nM cleaved FRET pair, and FRET efficiency was recorded until equilibrium was reached.

Pyrophosphatase-coupled cGAS activity assay. cGAS activity was assayed using the pyrophosphatase-coupled assay developed by Stivers and colleagues (Seamon and Stivers 2015) with modifications. Briefly, cGAS was incubated with 50 nM *E. coli* pyrophosphatase, equimolar concentrations of ATP and GTP plus dsDNAs (where indicated) in the reaction buffer. At indicated time points, an aliquot was taken and mixed with an equal volume of quench solution (Reaction buffer minus Mg^{++} plus 25 mM EDTA). Quenched solutions were then mixed with 10 µl malachite green solution and incubated for 45 min at RT. Absorbance at ~620 nm was compared to an internal standard curve of inorganic phosphate to determine the concentration of phosphate in each well. Phosphate concentrations of control reactions devoid of recombinant cGAS were subtracted from reactions containing recombinant cGAS. Apparent catalytic rates were calculated from the slopes of control-subtracted phosphate concentrations over time. Reported rates were halved to reflect pyrophosphate production. Average values are listed in Tables.

nsEM. Experiments were conducted using a Philips BioTwin CM120 (FEI) as described previously (Morrone et al. 2015).

SAXS data collection and analysis

SAXS data was collected on the BIOSAXS 2000 (Rigaku) at the X-ray facility of the Department of Biophysics and Biophysical Chemistry at Johns Hopkins School of Medicine. Data was collected on at least three different concentrations for each sample. Samples with scatter showing significant inter-particle effects were omitted from data analysis. Buffer-subtracted scatter was processed in Scatter (Petoukhov and Svergun 2013; Petoukhov et al. 2012; Mylonas and Svergun 2007) and with the ATSAS package (Petoukhov and Svergun 2013; Petoukhov et al. 2012; Mylonas and Svergun 2007). Particle dimensions were compared between guinier analysis and real-space fitting of the scatter to ensure internal consistency of the data and fits. Estimates of average and relative molecular weights of each sample were estimated using porod volumes (Petoukhov and Svergun 2013; Petoukhov et al. 2012; Mylonas and Svergun 2007) and mass-normalized I_0 values. The distribution of monomeric and dimeric species was calculated using SAXS-estimated molecular weights and OLIGOMER. IN OLIGOMER, crystal structures of monomeric cGAS and dimeric cGAS were used as a reference (PDB ID: 4LEV).

References:

Abe, T., Harashima, A., Xia, T., Konno, H., Konno, K., Morales, A., Ahn, J., Gutman, D., and Barber, G.N. (2013). STING recognition of cytoplasmic DNA instigates cellular defense. Mol Cell *50*, 5-15.

An, J., Durcan, L., Karr, R.M., Briggs, T.A., Rice, G.I., Teal, T.H., Woodward, J.J., and Elkon, K.B. (2017). Expression of Cyclic GMP-AMP Synthase in Patients With Systemic Lupus Erythematosus. Arthritis Rheumatol *69*, 800-807.

Andreeva, L., Hiller, B., Kostrewa, D., Lassig, C., de Oliveira Mann, C.C., Jan Drexler, D., Maiser, A., Gaidt, M., Leonhardt, H., Hornung, V.*, et al.* (2017). cGAS senses long and HMGB/TFAM-bound U-turn DNA by forming protein-DNA ladders. Nature *549*, 394-398.

Chang, C.W., Li, H.C., Hsu, C.F., Chang, C.Y., and Lo, S.Y. (2009). Increased ATP generation in the host cell is required for efficient vaccinia virus production. J Biomed Sci *16*, 80.

Chen, Q., Sun, L., and Chen, Z.J. (2016a). Regulation and function of the cGAS-STING pathway of cytosolic DNA sensing. Nat Immunol *17*, 1142-1149.

Chen, W.W., Freinkman, E., Wang, T., Birsoy, K., and Sabatini, D.M. (2016b). Absolute Quantification of Matrix Metabolites Reveals the Dynamics of Mitochondrial Metabolism. Cell *166*, 1324-1337 e1311.

Corton, J.M., Gillespie, J.G., and Hardie, D.G. (1994). Role of the AMP-activated protein kinase in the cellular stress response. Curr Biol *4*, 315-324.

Denais, C.M., Gilbert, R.M., Isermann, P., McGregor, A.L., te Lindert, M., Weigelin, B., Davidson, P.M., Friedl, P., Wolf, K., and Lammerding, J. (2016). Nuclear envelope rupture and repair during cancer cell migration. Science *352*, 353-358.

Du, M., and Chen, Z.J. (2018). DNA-induced liquid phase condensation of cGAS activates innate immune signaling. Science.

Fernandes-Alnemri, T., Yu, J.W., Datta, P., Wu, J., and Alnemri, E.S. (2009). AIM2 activates the inflammasome and cell death in response to cytoplasmic DNA. Nature *458*, 509-513.

Gao, D., Li, T., Li, X.D., Chen, X., Li, Q.Z., Wight-Carter, M., and Chen, Z.J. (2015). Activation of cyclic GMP-AMP synthase by self-DNA causes autoimmune diseases. Proc Natl Acad Sci U S A *112*, E5699-5705.

Gao, D., Wu, J., Wu, Y.T., Du, F., Aroh, C., Yan, N., Sun, L., and Chen, Z.J. (2013a). Cyclic GMP-AMP synthase is an innate immune sensor of HIV and other retroviruses. Science *341*, 903-906.

Gao, P., Ascano, M., Wu, Y., Barchet, W., Gaffney, B.L., Zillinger, T., Serganov, A.A., Liu, Y., Jones, R.A., Hartmann, G.*, et al.* (2013b). Cyclic [G(2',5')pA(3',5')p] is the metazoan second messenger produced by DNA-activated cyclic GMP-AMP synthase. Cell *153*, 1094-1107.

Guimaraes, C.P., Witte, M.D., Theile, C.S., Bozkurt, G., Kundrat, L., Blom, A.E., and Ploegh, H.L. (2013). Site-specific C-terminal and internal loop labeling of proteins using sortase-mediated reactions. Nat Protoc *8*, 1787-1799.

Gulen, M.F., Koch, U., Haag, S.M., Schuler, F., Apetoh, L., Villunger, A., Radtke, F., and Ablasser, A. (2017). Signalling strength determines proapoptotic functions of STING. Nat Commun *8*, 427.

Hall, J., Ralph, E.C., Shanker, S., Wang, H., Byrnes, L.J., Horst, R., Wong, J., Brault, A., Dumlao, D., Smith, J.F.*, et al.* (2017). The catalytic mechanism of cyclic gmp-amp synthase (cGAS) and implications for innate immunity and inhibition. Protein Sci.

Hansen, K., Prabakaran, T., Laustsen, A., Jorgensen, S.E., Rahbaek, S.H., Jensen, S.B., Nielsen, R., Leber, J.H., Decker, T., Horan, K.A.*, et al.* (2014). Listeria monocytogenes induces IFNbeta expression through an IFI16-, cGAS- and STING-dependent pathway. EMBO J *33*, 1654-1666.

Hornung, V., Ablasser, A., Charrel-Dennis, M., Bauernfeind, F., Horvath, G., Caffrey, D.R., Latz, E., and Fitzgerald, K.A. (2009). AIM2 recognizes cytosolic dsDNA and forms a caspase-1-activating inflammasome with ASC. Nature *458*, 514-518.

Huang, D., Zhang, Y., and Chen, X. (2003). Analysis of intracellular nucleoside triphosphate levels in normal and tumor cell lines by high-performance liquid chromatography. J Chromatogr B Analyt Technol Biomed Life Sci *784*, 101-109.

Ishii, K.J., Suzuki, K., Coban, C., Takeshita, F., Itoh, Y., Matoba, H., Kohn, L.D., and Klinman, D.M. (2001). Genomic DNA released by dying cells induces the maturation of APCs. J Immunol *167*, 2602-2607.

Koshland, D.E., Jr., Nemethy, G., and Filmer, D. (1966). Comparison of experimental binding data and theoretical models in proteins containing subunits. Biochemistry *5*, 365-385.

Kranzusch, P.J., Lee, A.S., Berger, J.M., and Doudna, J.A. (2013). Structure of human cGAS reveals a conserved family of second-messenger enzymes in innate immunity. Cell Rep *3*, 1362-1368.

Larkin, B., Ilyukha, V., Sorokin, M., Buzdin, A., Vannier, E., and Poltorak, A. (2017). Cutting Edge: Activation of STING in T Cells Induces Type I IFN Responses and Cell Death. J Immunol *199*, 397-402.

Lee, A., Park, E.B., Lee, J., Choi, B.S., and Kang, S.J. (2017). The N terminus of cGAS de-oligomerizes the cGAS:DNA complex and lifts the DNA size restriction of core-cGAS activity. FEBS Lett *591*, 954-961.

Li, T., and Chen, Z.J. (2018). The cGAS-cGAMP-STING pathway connects DNA damage to inflammation, senescence, and cancer. J Exp Med.

Li, T., Cheng, H., Yuan, H., Xu, Q., Shu, C., Zhang, Y., Xu, P., Tan, J., Rui, Y., Li, P., *et al.* (2016). Antitumor Activity of cGAMP via Stimulation of cGAS-cGAMP-STING-IRF3 Mediated Innate Immune Response. Sci Rep *6*, 19049.

Li, X., Shu, C., Yi, G., Chaton, C.T., Shelton, C.L., Diao, J., Zuo, X., Kao, C.C., Herr, A.B., and Li, P. (2013). Cyclic GMP-AMP synthase is activated by double-stranded DNA-induced oligomerization. Immunity *39*, 1019-1031.

Liang, Q., Seo, G.J., Choi, Y.J., Kwak, M.J., Ge, J., Rodgers, M.A., Shi, M., Leslie, B.J., Hopfner, K.P., Ha, T., *et al.* (2014). Crosstalk between the cGAS DNA sensor and Beclin-1 autophagy protein shapes innate antimicrobial immune responses. Cell Host Microbe *15*, 228-238.

Linehan, M.M., Dickey, T.H., Molinari, E.S., Fitzgerald, M.E., Potapova, O., Iwasaki, A., and Pyle, A.M. (2018). A minimal RNA ligand for potent RIG-I activation in living mice. Sci Adv *4*, e1701854.

Liu, T., Yamaguchi, Y., Shirasaki, Y., Shikada, K., Yamagishi, M., Hoshino, K., Kaisho, T., Takemoto, K., Suzuki, T., Kuranaga, E., *et al.* (2014). Single-cell imaging of caspase-1 dynamics reveals an all-or-none inflammasome signaling response. Cell Rep *8*, 974-982.

Luecke, S., Holleufer, A., Christensen, M.H., Jonsson, K.L., Boni, G.A., Sorensen, L.K., Johannsen, M., Jakobsen, M.R., Hartmann, R., and Paludan, S.R. (2017). cGAS is activated by DNA in a length-dependent manner. EMBO Rep.

Ma, F., Li, B., Liu, S.Y., Iyer, S.S., Yu, Y., Wu, A., and Cheng, G. (2015). Positive feedback regulation of type I IFN production by the IFN-inducible DNA sensor cGAS. J Immunol *194*, 1545-1554.

Mackenzie, K.J., Carroll, P., Martin, C.A., Murina, O., Fluteau, A., Simpson, D.J., Olova, N., Sutcliffe, H., Rainger, J.K., Leitch, A., *et al.* (2017). cGAS surveillance of micronuclei links genome instability to innate immunity. Nature *548*, 461-465.

Marcussen, M., and Larsen, P.J. (1996). Cell cycle-dependent regulation of cellular ATP concentration, and depolymerization of the interphase microtubular network induced by elevated cellular ATP concentration in whole fibroblasts. Cell Motil Cytoskeleton *35*, 94-99.

Matyszewski, M., Morrone, S.R., and Sohn, J. (2018). Digital signaling network drives the assembly of the AIM2-ASC inflammasome. Proc Natl Acad Sci U S A.

Monod, J., Wyman, J., and Changeux, J.P. (1965). On the Nature of Allosteric Transitions: A Plausible Model. J Mol Biol *12*, 88-118.

Morrone, S.R., Matyszewski, M., Yu, X., Delannoy, M., Egelman, E.H., and Sohn, J. (2015). Assembly-driven activation of the AIM2 foreign-dsDNA sensor provides a polymerization template for downstream ASC. Nat Commun *6*, 7827.

Mylonas, E., and Svergun, D.I. (2007). Accuracy of molecular mass determination of proteins in solution by small-angle X-ray scattering. Journal of Applied Crystallography *40*, S245-S249.

Ng, K.W., Marshall, E.A., Bell, J.C., and Lam, W.L. (2017). cGAS-STING and Cancer: Dichotomous Roles in Tumor Immunity and Development. Trends Immunol.

Ogawa, M., Takemoto, Y., Sumi, S., Inoue, D., Kishimoto, N., Takamune, N., Shoji, S., Suzu, S., and Misumi, S. (2015). ATP generation in a host cell in early-phase infection is increased by upregulation of cytochrome c oxidase activity via the p2 peptide from human immunodeficiency virus type 1 Gag. Retrovirology *12*, 97.

Paludan, S.R., and Bowie, A.G. (2013). Immune sensing of DNA. Immunity *38*, 870-880.

Peisley, A., Lin, C., Wu, B., Orme-Johnson, M., Liu, M., Walz, T., and Hur, S. (2011). Cooperative assembly and dynamic disassembly of MDA5 filaments for viral dsRNA recognition. Proc Natl Acad Sci U S A *108*, 21010-21015.

Peisley, A., Wu, B., Yao, H., Walz, T., and Hur, S. (2013). RIG-I forms signaling-competent filaments in an ATP-dependent, ubiquitin-independent manner. Mol Cell *51*, 573-583.

Petoukhov, M.V., Franke, D., Shkumatov, A.V., Tria, G., Kikhney, A.G., Gajda, M., Gorba, C., Mertens, H.D., Konarev, P.V., and Svergun, D.I. (2012). New developments in the ATSAS program package for small-angle scattering data analysis. J Appl Crystallogr *45*, 342-350.

Petoukhov, M.V., and Svergun, D.I. (2013). Applications of small-angle X-ray scattering to biomacromolecular solutions. Int J Biochem Cell Biol *45*, 429-437.

Pokatayev, V., Hasin, N., Chon, H., Cerritelli, S.M., Sakhuja, K., Ward, J.M., Morris, H.D., Yan, N., and Crouch, R.J. (2016). RNase H2 catalytic core Aicardi-Goutieres syndrome-related mutant invokes cGAS-STING innate immune-sensing pathway in mice. J Exp Med *213*, 329-336.

Ramanathan, A., Devarkar, S.C., Jiang, F., Miller, M.T., Khan, A.G., Marcotrigiano, J., and Patel, S.S. (2016). The autoinhibitory CARD2-Hel2i Interface of RIG-I governs RNA selection. Nucleic Acids Res *44*, 896-909.

Reinert, L.S., Lopusna, K., Winther, H., Sun, C., Thomsen, M.K., Nandakumar, R., Mogensen, T.H., Meyer, M., Vaegter, C., Nyengaard, J.R*., et al.* (2016). Sensing of HSV-1 by the cGAS-STING pathway in microglia orchestrates antiviral defence in the CNS. Nat Commun *7*, 13348.

Roberts, T.L., Idris, A., Dunn, J.A., Kelly, G.M., Burnton, C.M., Hodgson, S., Hardy, L.L., Garceau, V., Sweet, M.J., Ross, I.L*., et al.* (2009). HIN-200 proteins regulate caspase activation in response to foreign cytoplasmic DNA. Science *323*, 1057-1060.

Seamon, K.J., and Stivers, J.T. (2015). A High-Throughput Enzyme-Coupled Assay for SAMHD1 dNTPase. J Biomol Screen *20*, 801-809.

Seo, G.J., Kim, C., Shin, W.J., Sklan, E.H., Eoh, H., and Jung, J.U. (2018). TRIM56-mediated monoubiquitination of cGAS for cytosolic DNA sensing. Nat Commun *9*, 613.

Shen, Y.J., Le Bert, N., Chitre, A.A., Koo, C.X., Nga, X.H., Ho, S.S., Khatoo, M., Tan, N.Y., Ishii, K.J., and Gasser, S. (2015). Genome-derived cytosolic DNA mediates type I interferon-dependent rejection of B cell lymphoma cells. Cell Rep *11*, 460-473.

Sohn, J., Grant, R.A., and Sauer, R.T. (2007). Allosteric activation of DegS, a stress sensor PDZ protease. Cell *131*, 572-583.

Sohn, J., and Hur, S. (2016). Filament assemblies in foreign nucleic acid sensors. Curr Opin Struct Biol *37*, 134-144.

Sohn, J., and Sauer, R.T. (2009). OMP peptides modulate the activity of DegS protease by differential binding to active and inactive conformations. Mol Cell *33*, 64-74.

Stetson, D.B., and Medzhitov, R. (2006). Recognition of cytosolic DNA activates an IRF3-dependent innate immune response. Immunity *24*, 93-103.

Sun, L., Wu, J., Du, F., Chen, X., and Chen, Z.J. (2013). Cyclic GMP-AMP synthase is a cytosolic DNA sensor that activates the type I interferon pathway. Science *339*, 786-791.

Tang, C.H., Zundell, J.A., Ranatunga, S., Lin, C., Nefedova, Y., Del Valle, J.R., and Hu, C.C. (2016). Agonist-Mediated Activation of STING Induces Apoptosis in Malignant B Cells. Cancer Res *76*, 2137-2152.

Tao, J., Zhang, X.W., Jin, J., Du, X.X., Lian, T., Yang, J., Zhou, X., Jiang, Z., and Su, X.D. (2017). Nonspecific DNA Binding of cGAS N Terminus Promotes cGAS Activation. J Immunol *198*, 3627-3636.

Traut, T.W. (1994). Physiological concentrations of purines and pyrimidines. Mol Cell Biochem *140*, 1-22.

Tsai, C.J., and Nussinov, R. (2014). A unified view of "how allostery works". PLoS Comput Biol *10*, e1003394.

Unterholzner, L., Keating, S.E., Baran, M., Horan, K.A., Jensen, S.B., Sharma, S., Sirois, C.M., Jin, T., Latz, E., Xiao, T.S*., et al.* (2010). IFI16 is an innate immune sensor for intracellular DNA. Nat Immunol *11*, 997-1004.

van Boxel-Dezaire, A.H., Rani, M.R., and Stark, G.R. (2006). Complex modulation of cell type-specific signaling in response to type I interferons. Immunity *25*, 361-372.

Vincent, J., Adura, C., Gao, P., Luz, A., Lama, L., Asano, Y., Okamoto, R., Imaeda, T., Aida, J., Rothamel, K*., et al.* (2017). Small molecule inhibition of cGAS reduces interferon expression in primary macrophages from autoimmune mice. Nat Commun *8*, 750.

Wang, W., Yang, X., Lopez de Silanes, I., Carling, D., and Gorospe, M. (2003). Increased AMP:ATP ratio and AMP-activated protein kinase activity during cellular senescence linked to reduced HuR function. J Biol Chem *278*, 27016-27023.

Wang, Y., Ning, X., Gao, P., Wu, S., Sha, M., Lv, M., Zhou, X., Gao, J., Fang, R., Meng, G*., et al.* (2017). Inflammasome Activation Triggers Caspase-1-Mediated Cleavage of cGAS to Regulate Responses to DNA Virus Infection. Immunity *46*, 393-404.

West, A.P., Khoury-Hanold, W., Staron, M., Tal, M.C., Pineda, C.M., Lang, S.M., Bestwick, M., Duguay, B.A., Raimundo, N., MacDuff, D.A*., et al.* (2015). Mitochondrial DNA stress primes the antiviral innate immune response. Nature *520*, 553-557.

West, A.P., and Shadel, G.S. (2017). Mitochondrial DNA in innate immune responses and inflammatory pathology. Nat Rev Immunol *17*, 363-375.

Yang, H., Wang, H., Ren, J., Chen, Q., and Chen, Z.J. (2017). cGAS is essential for cellular senescence. Proc Natl Acad Sci U S A *114*, E4612-E4620.

Zhang, X., Wu, J., Du, F., Xu, H., Sun, L., Chen, Z., Brautigam, C.A., Zhang, X., and Chen, Z.J. (2014). The cytosolic DNA sensor cGAS forms an oligomeric complex with DNA and undergoes switch-like conformational changes in the activation loop. Cell Rep *6*, 421-430.

Zhou, W., Whiteley, A.T., de Oliveira Mann, C.C., Morehouse, B.R., Nowak, R.P., Fischer, E.S., Gray, N.S., Mekalanos, J.J., and Kranzusch, P.J. (2018). Structure of the Human cGAS-DNA Complex Reveals Enhanced Control of Immune Surveillance. Cell *174*, 300-311 e311.

Chapter 4

Defining the molecular mechanism by which divalent manganese sensitizes cGAS to DNA

Introduction

Cytosolic double-stranded (ds)DNA is a hallmark of cellular stress. For instance, genomic instability, microbial infection and organelle failure can all result in release of dsDNA into the cytoplasm (Mackenzie et al. 2017; Harding et al. 2017; White et al. 2014; West et al. 2015; Riley et al. 2018; Ishikawa, Ma, and Barber 2009). Cyclic GMP-AMP synthase (cGAS), a pattern recognition receptor of the innate immune system, is the primary initiator of the cellular stress response to cytosolic dsDNA, and triggers induction of type-I interferons (IFN-I) upon dsDNA detection (Sun et al. 2013). Binding of dsDNA enables cGAS to cyclize ATP and GTP into the unique second messenger, cyclic GMP-AMP (cGAMP), bearing mixed-linkage phosphodiester bonds (Ablasser et al. 2013; Diner et al. 2013; Gao, Ascano, et al. 2013). cGAMP binds and activates STING, which facilitates TBK1 recruitment and activation of transcription factors, IRF3 and NF-κB. The strength of cGAS signaling varies with stimulus which results in diverse cellular outcomes highlighting a need to understand how cGAS activity is regulated (Gluck et al. 2017; Gulen et al. 2017; Andreeva et al. 2017)

The mechanistic link between dsDNA binding and cGAS activity is well established. Structural studies of cGAS in the presence and absence of dsDNA illustrate how dsDNA binding orients the active site for catalysis (Civril et al. 2013; Li et al. 2013; Shu, Li, and Li 2014; Zhang et al. 2014). dsDNA is also crucial for promoting cGAS dimerization, a requisite for cGAS activity (Li et al. 2013; Zhang et al. 2014). Importantly, the ease of cGAS dimerization is directly linked to dsDNA length, which manifests in graded cGAS activity both in cells and *in vitro* (Andreeva et al. 2017; Luecke et al. 2017a; Hooy and Sohn 2018). Although some evidence suggests that the dsDNA length-dependence spawns from formation of higher-order structural arrangements (Andreeva et al. 2017), it remains controversial whether ordered structures beyond the dimeric unit are needed to achieve dsDNA length-dependent activity (Hooy and Sohn 2018).

Additional studies have recently revealed that the degree of dsDNA length-dependent activity is tunable depending on reaction context. Substrate and cGAS concentrations toggle the sensitivity of cGAS to dsDNA length (Hooy and Sohn, 2018). It is also known that post-translational modifications can render resident cGAS populations to be less, or more active depending on the modification (Chen, Meng, et al. 2016; Hu et al. 2016; Wang, Huang, et al. 2017; Liu et al. 2018; Seo et al. 2018; Xia et al. 2016; Seo et al. 2015; Wang, Ning, et al. 2017). Extrinsic factors, such as protein co-sensors, can also aid or repress dsDNA sensing by cGAS (Almine et al. 2017; Biolatti et al. 2018; Shannon et al. 2018; Lian et al. 2018). More recently, zinc and manganese, divalent cations found ubiquitously in nature, were proposed to enhance cGAS activity. Zinc is thought to promote inter-strand crosslinking of cGAS-dsDNA complexes, which facilitates phase-separation and condensate formation, but in a dsDNA length-dependent manner (Du and Chen 2018b). Manganese was also shown to improve the cGAS-mediated response to viral challenge and dsDNA stimulation, but whether the manganese effect was dependent on dsDNA length was unclear (Wang, Guan, et al. 2018).

Manganese, like magnesium, is a cofactor for various enzymes, including nucleotidyl transferases (NTases), and, in the +2 oxidation state, typically serves as a general Lewis acid to polarize phosphoryl groups and/or activate nucleophiles. Enzymes that use magnesium for catalysis oftentimes retain function when manganese is substituted as the cofactor (Vashishtha, Wang, and Konigsberg 2016). Although cGAS was shown to be more sensitive to dsDNA in the presence of manganese (Wang, Guan, et al. 2018), it remained unclear whether the effect was due to changes in catalytic activity, or due to changes in the way cGAS interacted with dsDNA. Here we sought to determine the mechanism by which manganese contributes to the allosteric regulation of cGAS signaling in response to dsDNA.

We find that manganese reduces the dsDNA length-dependent response of cGAS in cells and *in vitro*. This phenomenon is not due to a direct effect of manganese on dimerization or dsDNA-induced dimerization, rather manganese increased the catalytic capacity of dsDNA-bound, monomeric and dimeric cGAS. Manganese can substitute for magnesium as the cofactor for catalysis, and in general, Mn^{2+} supports catalysis more efficiently than magnesium. Surprisingly, manganese alone is capable of activating monomeric cGAS, even in the absence of dsDNA, although relatively high concentrations of Mn^{2+} are required to achieve this auto-activation. Importantly, the functional binding affinity of Mn^{2+} is directly coupled to dsDNA binding, and vice versa, and this ultimately reduces the functional binding constant of Mn^{2+} to levels within the physiological range (Bowman and Aschner 2014). Lastly, low levels of manganese are sufficient to specifically accelerate cGAMP production, whereas elevated concentrations of manganese promote significant off-product catalysis. Moreover, we provide evidence that dsDNA binding contributes to the high fidelity coupling of ATP/GTP over other dinucleotide products. Together these data define the mechanistic role of Mn^{2+} in cGAS stress sensing, and bolster the validity of explaining cGAS signaling through an allosteric equilibrium activation model.

Results

Manganese reduces the dsDNA length-dependent activity of cGAS

It was recently demonstrated that lower concentrations of dsDNA were sufficient to stimulate cGAS when manganese was present, yet it remained unclear if the apparent increase in "sensitivity" to dsDNA applied to all lengths of dsDNA (Wang, Guan, et al. 2018). This is important given that cGAS activity in cells is dsDNA-length dependent. To test if dsDNA length-dependence changes with Mn^{2+}, cGAS activity was assayed *in vitro* using recombinant, full-length, human protein, $cGAS^{FL}$ (Figure 1A). Under saturating levels of dsDNA, $cGAS^{FL}$ displayed increased activity as a function of dsDNA length, consistent with previous findings. In the presence of 50uM Mn^{2+}, the difference in rates between short and long dsDNA reduced dramatically. Thus, the reduced difference in dsDNA length-dependent activity in cells is due to a direct effect of Mn^{2+} on cGAS.

cGAS activity that is less dependent on dsDNA length could be explained in two ways (Figure 1B). First, Mn^{2+} could directly influence the ability of cGAS to dimerize. Dimerization is thought to be essential for cGAS to be active (Li et al. 2013; Zhang et al. 2014). Moreover, enhanced dimerization would effectively increase the binding affinity for dsDNA, especially short dsDNA, similar to the effect achieved by the N-terminal extension (Hooy and Sohn 2018; Tao et al. 2017) or post-translational modifications (Seo et al. 2018). Alternatively, Mn^{2+} could serve as a cofactor for catalysis and promote faster turnover of substrate. Mn^{2+} is known to substitute for Mg^{2+} in nucleotidyl transferases, such as polymerases, and generally results in faster catalysis. The following experiments test these hypotheses.

Figure 1

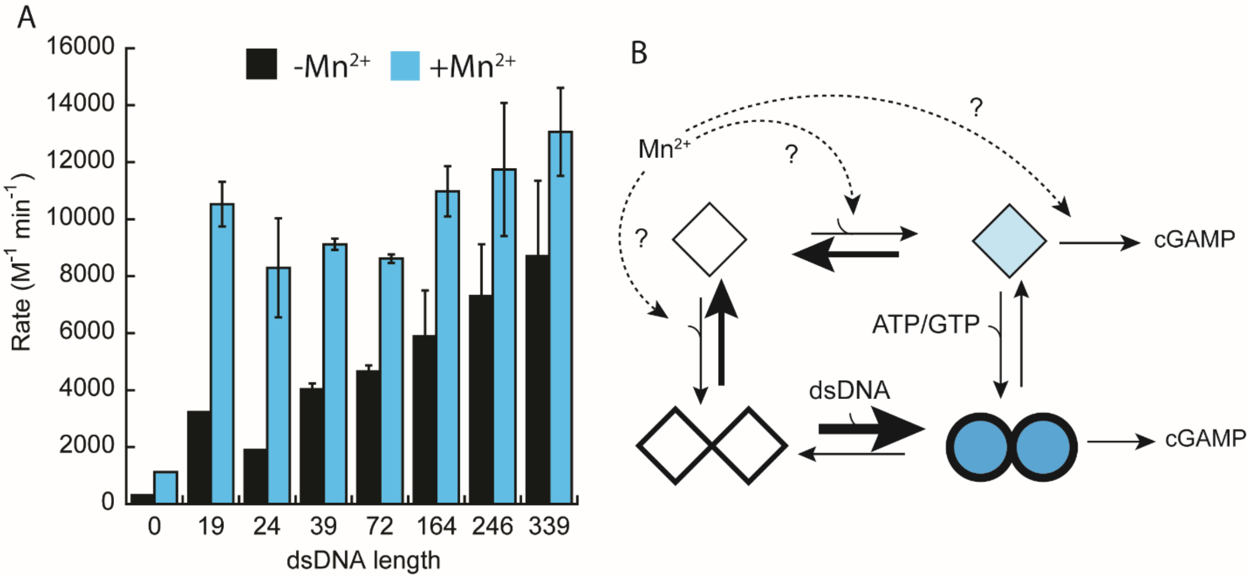

Figure 1. Manganese reduces the dsDNA-length dependent response *in vitro*.

A) recombinant cGAS^{FL} NTase activity was measured under steady state conditions in the presence or absence of 50uM and saturating levels of dsDNA. Reaction conditions: 100uM ATP/GTP, 10nM enzyme, 50nM PP$_i$ase; [dsDNA] = 6x K$_{act}$ (Hooy and Sohn 2018).

B) Hypothetical model of how Mn^{2+} 'sensitizes' cGAS to dsDNA. The allosteric equilibrium model posits that Mn^{2+} could affect auto-dimerization, ligand-induced dimerization, or catalytic rates.

Manganese does not affect cGAS dimerization or its inherent binding affinity for dsDNA

dsDNA length-dependent binding is directly linked to the extent by which a dsDNA stabilizes the dimeric state of cGAS (Hooy and Sohn 2018; Zhou et al. 2018). To test if Mn^{2+} enhances the ability of dsDNA to promote dimerization, different lengths of dsDNA were titrated against FRET-pair-labeled cGAS^{FL} in the presence or absence of Mn^{2+} (Figure 2 – figure supplement 1A). The presence of Mn^{2+} did not significantly affect the concentration required to achieve half maximal

FRET changes, $K_{FRET'}$, nor the overall change in FRET, regardless of dsDNA length, indicating Mn^{2+} does not affect dsDNA-induced dimerization. Titrations of Mn^{2+} against fixed concentrations of dsDNA indicated no dose-dependent link between dsDNA length, dsDNA binding, or dimerization, further supporting this notion (Figure 2 – figure supplement 1B). Mn^{2+} was also incapable of promoting cGAS dimerization in the absence of dsDNA. Consistent with these observations, the binding affinity for FAM-labeled dsDNA was minimally impacted by the presence of Mn^{2+} (Figure 2 – figure supplement 1C). These data indicate that Mn^{2+} does not directly affect cGAS (dsDNA-induced) dimerization, nor the binding affinity for any length of dsDNA.

Substrate binding is also linked to cGAS dimerization, and metals associate with substrates in the active site. Hence, it will be an important to test if Mn^{2+} can affect substrate-induced dimerization. This experiment will be performed in the future, and as described in Chapter 3. Briefly, ATP/GTP and their non-hydrolyzable analogues will be titrated against FRET-pair-labeled cGAS in the presence and absence of Mn^{2+}. Implications of the results are described in the discussion.

Figure 2 - figure supplement 1

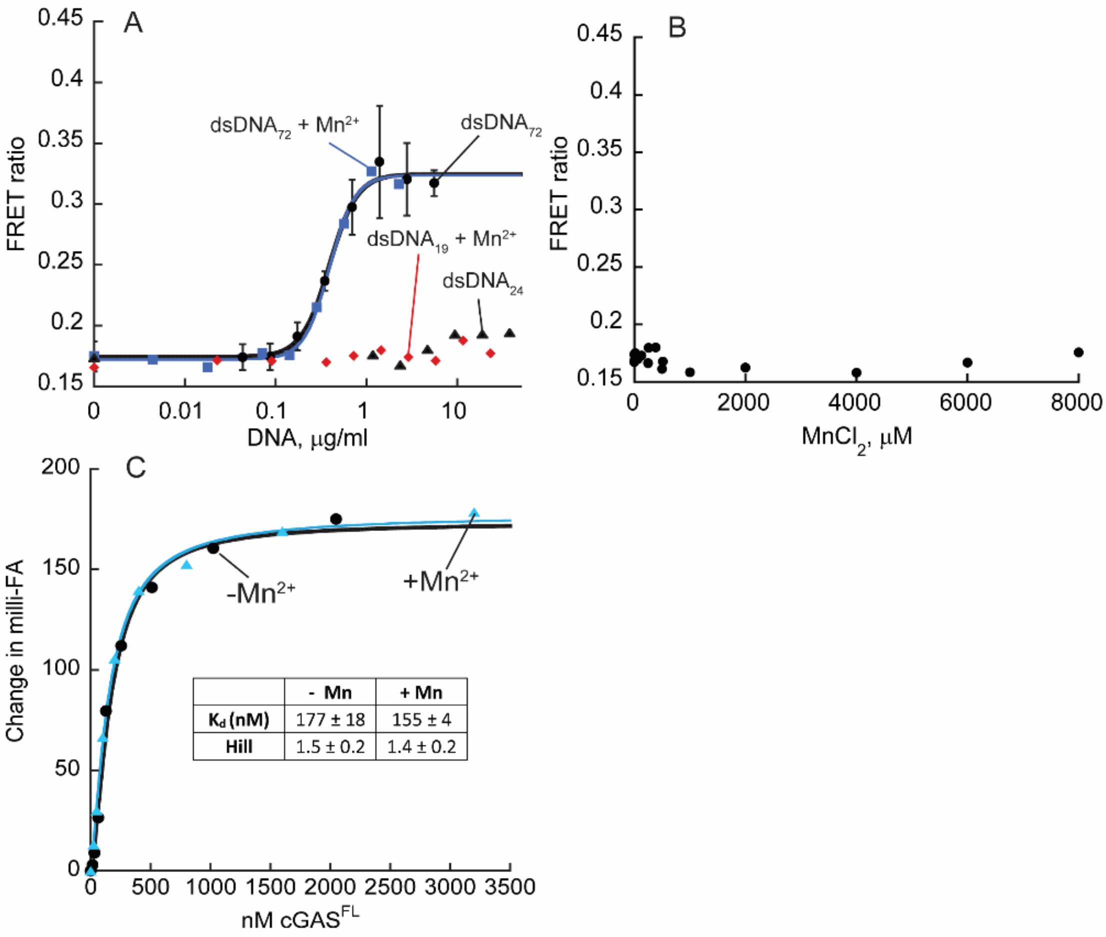

	- Mn	+ Mn
K_d (nM)	177 ± 18	155 ± 4
Hill	1.5 ± 0.2	1.4 ± 0.2

Figure 2 – figure supplement 1. Manganese does not enhance cGAS dimerization or dsDNA binding affinity.

A) FRET of cGAS^{FL} as a function of dsDNA concentration in the presence and absence of 500uM Mn^{2+}.

B) FRET of cGAS^{FL} as a function of Mn^{2+} concentration in the absence of dsDNA.

C) Change in fluorescence anisotropy of FAM-dsDNA$_{19}$ in the presence and absence of 500uM Mn^{2+} as a function of cGAS^{FL} concentration. Data was fit with the Hill form of the binding equation: max / (1+(K$_d$ / [cGAS^{FL}])^{Hill}). Fits to the data are shown in the inset Table.

Manganese increases the catalytic turnover of dsDNA-bound cGAS

Mn^{2+} can substitute for Mg^{2+} as a cofactor in many NTases, including cGAS (Gao, Ascano, et al. 2013), and in several instances, promotes faster turnover of substrates (Frank and Woodgate 2007). To test if Mn^{2+} could affect the maximal turnover rate of cGAS, steady state activity was assayed as a function of Mn^{2+} concentration under saturating levels of short (19-bp, $dsDNA_{19}$), medium (72-bp, $dsDNA_{72}$) and long (339-bp, $dsDNA_{339}$) dsDNA. Apparent rates increased hyperbolically with Mn^{2+} for all dsDNA lengths and produced 2-5-fold increases in maximal turnover, k_{max}, depending on the dsDNA length (Figure 2A, Figure 2 – figure supplement 2). The concentration of Mn^{2+} required to achieve half-maximal stimulation, EC_{50}, was similar for the different dsDNA lengths, and fell within a range of 20-50uM. For comparison, the EC_{50} of Mg^{2+} in the presence of long dsDNA was 3-4mM (Figure 2 – figure supplement 2A), illustrating a clear preference of Mn^{2+} over Mg^{2+}. Moreover, the same Mn^{2+} titrations performed in the absence of free Mg^{2+} (low Mg^{2+}) resulted in similar maximal turnover rates and EC_{50}'s, but a more dramatic fold-change in activity due to reduced basal rates under low Mg^{2+} levels (Figure 2 – figure supplement 2). Interestingly, the maximal rates all peak around the same value, suggesting that under saturating dsDNA concentrations, Mn^{2+} nullifies differences between dsDNA lengths, consistent with the reduction of dsDNA length-dependence in cells.

The observed increase in catalytic activity could result from increased binding affinity for substrates. To test this, steady state rates were measured as a function of ATP/GTP in the presence of saturating dsDNAs, with or without saturating levels of Mn^{2+} (Figure 2C, Figure 2 – figure supplement 2). Substrate utilization was cooperative in the absence of Mn^{2+} and maximal turnover, k_{cat}, and substrate binding affinity, K_m, were tiered with dsDNA length, as previously reported. In the presence of Mn^{2+}, apparent K_ms were similar for each dsDNA activator relative to reactions without Mn^{2+}, but the k_{cat}s were globally elevated. Notably, substrate utilization was not cooperative in the presence of Mn^{2+}. Overall, the catalytic efficiency (k_{cat}/K_m) increased by a factor of 4-5 for each dsDNA, consistent with Figure 2A, and this is primarily achieved by increased turnover rate.

Figure 2

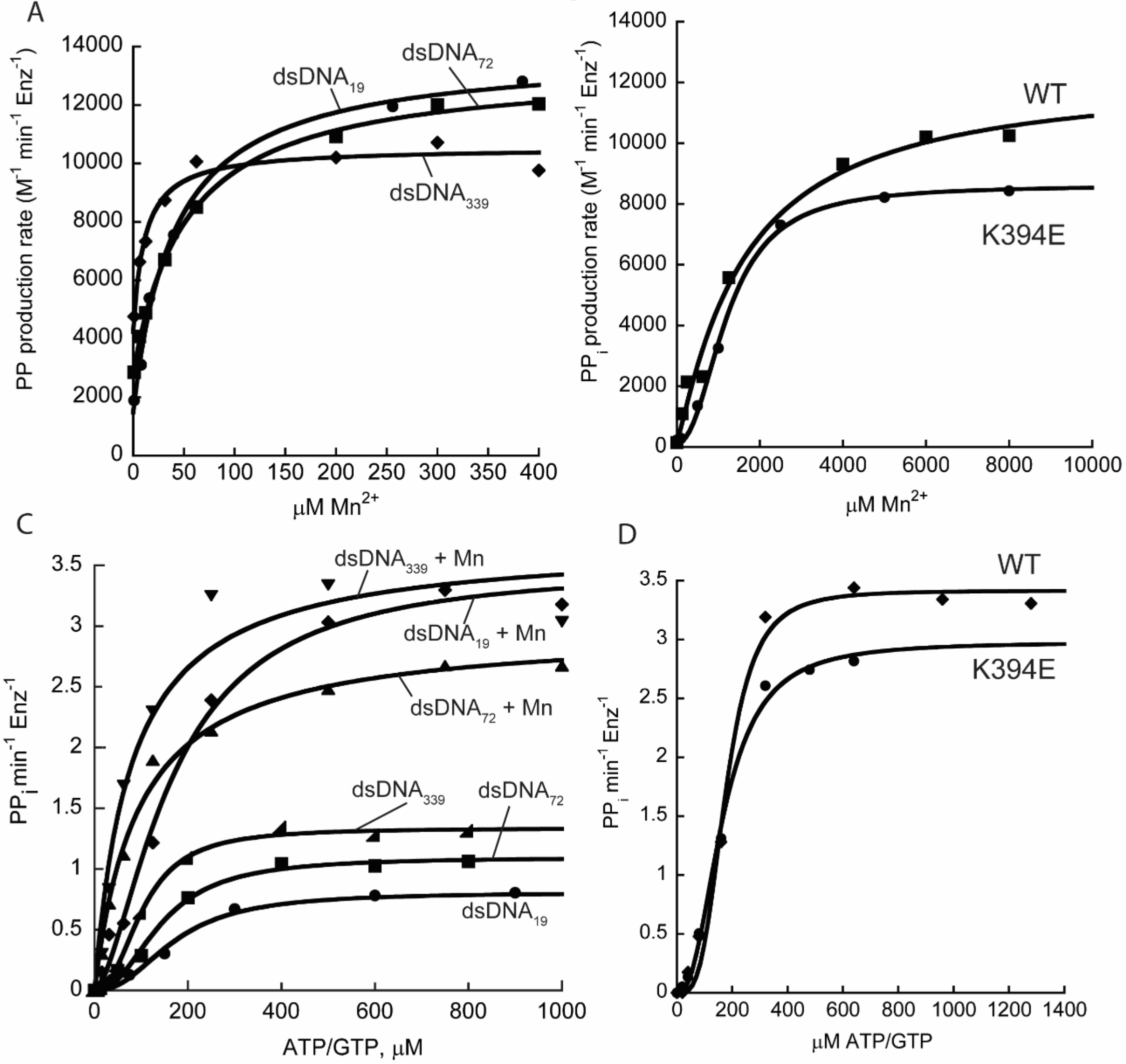

Figure 2. Manganese increases the catalytic turnover of apo and dsDNA-bound cGAS.

A) Steady-state rates of cGAS^{FL} as a function of Mn^{2+} concentration in 5mM Mg^{2+} buffer in the presence of saturating dsDNAs. Reaction conditions: 200uM ATP/GTP : 2 Mg^{2+}, 25nM cGAS^{FL}, 50nM PP$_i$ase; [dsDNA] = 6x K$_{act}$. Data were fit with the Hill form of the Michaelis-Menten equation: $(k_{max}-k_{min}) * (1 / (1+(EC_{50} / [Mn^{2+}])^{Hill}) + k_{min}$.

B) Steady-state rates of cGAS^{FL} and K394E-cGAS^{FL} as a function of Mn^{2+} concentration in 5mM Mg^{2+} buffer in the absence of dsDNAs. Reaction conditions: 200uM ATP/GTP : 2 Mg^{2+}, 25nM cGAS^{FL}, 50nM PP$_i$ase. Data were fit with the Hill form of the Michaelis-Menten equation: (k_{max}-k_{min}) * (1 / (1+(EC$_{50}$ / [Mn^{2+}])^{Hill}) + k_{min}.

C) Steady-state rates of cGAS^{FL} as a function of ATP/GTP concentration in 5mM Mg^{2+} buffer supplemented with or without 250uM Mn^{2+} and saturating levels of dsDNA. Reaction conditions: ATP/GTP : 2 Mg^{2+}, 25nM cGAS, 50nM PP$_i$ase; [dsDNA] = 6x K$_{act}$. Data were fit with the Hill form of the Michaelis-Menten equation: k_{cat} / (1+(K$_m$ / [ATP/GTP])^{Hill}).

D) Steady-state rates of cGAS^{FL} and K394E-cGAS^{FL} as a function of ATP/GTP concentration in 5mM Mn^{2+} buffer in the absence of dsDNA. Reaction conditions: ATP/GTP : 2 Mn^{2+}, 25nM cGAS, 50nM PP$_i$ase. Data were fit with the Hill form of the Michaelis-Menten equation: k_{cat} / (1+(K$_m$ / [ATP/GTP])^{Hill}).

Figure 2 - figure supplement 2

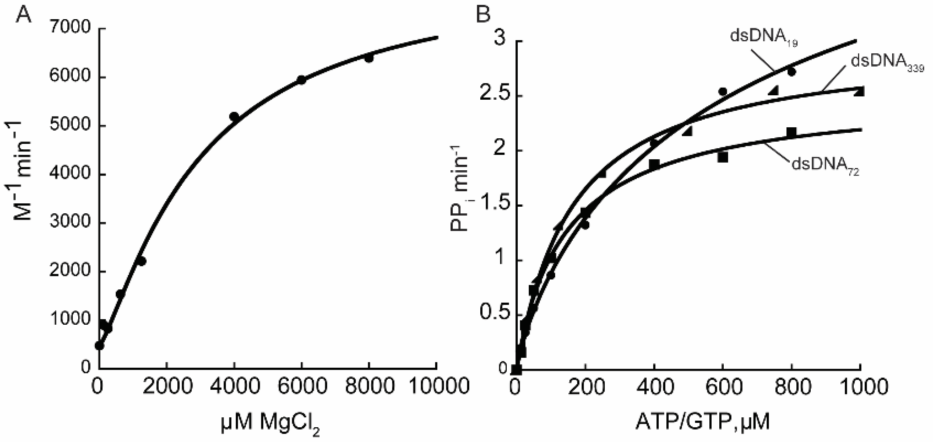

Table 1. Mn^{2+} activation constants

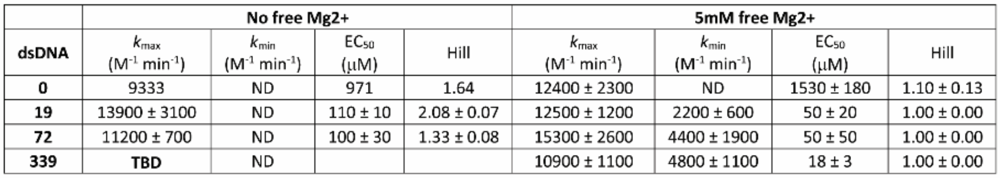

	No free Mg2+				5mM free Mg2+			
dsDNA	k_{max} ($M^{-1}\ min^{-1}$)	k_{min} ($M^{-1}\ min^{-1}$)	EC_{50} (μM)	Hill	k_{max} ($M^{-1}\ min^{-1}$)	k_{min} ($M^{-1}\ min^{-1}$)	EC_{50} (μM)	Hill
0	9333	ND	971	1.64	12400 ± 2300	ND	1530 ± 180	1.10 ± 0.13
19	13900 ± 3100	ND	110 ± 10	2.08 ± 0.07	12500 ± 1200	2200 ± 600	50 ± 20	1.00 ± 0.00
72	11200 ± 700	ND	100 ± 30	1.33 ± 0.08	15300 ± 2600	4400 ± 1900	50 ± 50	1.00 ± 0.00
339	**TBD**	ND			10900 ± 1100	4800 ± 1100	18 ± 3	1.00 ± 0.00

Table 2. Steady-state activity of $cGAS^{FL}$ in the presence and absence of supplemented Mn^{2+}

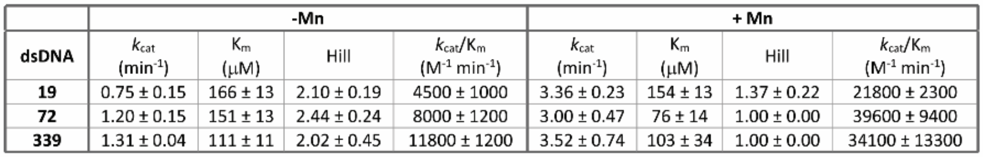

	-Mn				+ Mn			
dsDNA	k_{cat} (min^{-1})	K_m (μM)	Hill	k_{cat}/K_m ($M^{-1}\ min^{-1}$)	k_{cat} (min^{-1})	K_m (μM)	Hill	k_{cat}/K_m ($M^{-1}\ min^{-1}$)
19	0.75 ± 0.15	166 ± 13	2.10 ± 0.19	4500 ± 1000	3.36 ± 0.23	154 ± 13	1.37 ± 0.22	21800 ± 2300
72	1.20 ± 0.15	151 ± 13	2.44 ± 0.24	8000 ± 1200	3.00 ± 0.47	76 ± 14	1.00 ± 0.00	39600 ± 9400
339	1.31 ± 0.04	111 ± 11	2.02 ± 0.45	11800 ± 1200	3.52 ± 0.74	103 ± 34	1.00 ± 0.00	34100 ± 13300

Table 3. Steady-state activity of $cGAS^{FL}$ in Mn^{2+}-only buffer

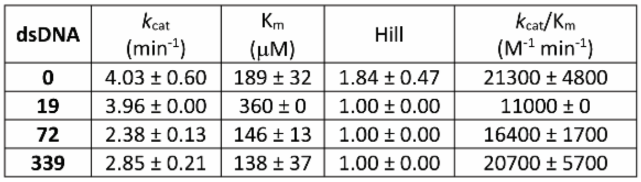

dsDNA	k_{cat} (min^{-1})	K_m (μM)	Hill	k_{cat}/K_m ($M^{-1}\ min^{-1}$)
0	4.03 ± 0.60	189 ± 32	1.84 ± 0.47	21300 ± 4800
19	3.96 ± 0.00	360 ± 0	1.00 ± 0.00	11000 ± 0
72	2.38 ± 0.13	146 ± 13	1.00 ± 0.00	16400 ± 1700
339	2.85 ± 0.21	138 ± 37	1.00 ± 0.00	20700 ± 5700

Figure 2 – figure supplement 2. Steady-state activity constants of $cGAS^{FL}$ under various conditions.

A) Steady-state activity of $cGAS^{FL}$ as a function of Mg^{2+} in the presence of saturating $dsDNA_{339}$. Reaction conditions: 200uM ATP/GTP : 2 Mg^{2+}, 25nM $cGAS^{FL}$, 50nM PP_iase. Data were fit with the Hill form of the Michaelis-Menten equation: $(k_{max}-k_{min}) * (1 / (1+(EC_{50} / [Mn^{2+}])^{Hill}) + k_{min}$.

B) Steady-state rates of $cGAS^{FL}$ as a function of ATP/GTP concentration in 5mM Mn^{2+} buffer and saturating levels of dsDNA. Reaction conditions: ATP/GTP : 2 Mn^{2+}, 25nM cGAS, 50nM PP_iase; [dsDNA] = 6x K_{act}. Data were fit with the Hill form of the Michaelis-Menten equation: $k_{cat} / (1+(K_m / [ATP/GTP])^{Hill})$.

Table 1. Mn^{2+} activation constants in reaction buffer containing no free Mg^{2+} or 5mM free Mg^{2+}; from Figure 2.

Table 2. Steady-state activity constants of $cGAS^{FL}$ in the presence and absence of supplemented Mn^{2+}; from Figure 2.

Table 3. Steady-state activity constants of $cGAS^{FL}$ in buffer containing no Mg^{2+} and 5mM Mn^{2+}; from Figure 2.

Note: The error is standard deviation of individual fits. Each experiment was performed at least three times.

Manganese activates monomeric cGAS even in the absence of dsDNA

The Mn^{2+}-specific increase in catalytic rate for all dsDNA lengths is confounded by the notion that Mn^{2+} does not directly affect cGAS dimerization. For instance, under saturating concentrations of short dsDNA, the fraction of dsDNA-bound dimers is presumed to be the same regardless of whether Mn^{2+} is present, yet the activity levels in the presence of Mn^{2+} increase substantially. Moreover, in the presence of long dsDNA, the dimeric fraction of cGAS is relatively high, yet the observed Mn^{2+}-mediated NTase rate is similar to the value measured for shorter dsDNA activators. Finally, the reduced cooperativity of substrate utilization and Mn^{2+} binding hinted that dsDNA-bound, dimeric cGAS may not be the only active species when Mn^{2+} was present.

Although dsDNA is thought to be essential for cGAS activation, in principle, molecules within the active site can promote the same conformational changes induced by dsDNA binding (Hall, Brault, et al. 2017; Zhang et al. 2014). To test if dsDNA was required for Mn^{2+}-mediated activity, cGAS NTase activity was again assayed as a function of Mn^{2+} concentration, but this time without dsDNA. Unexpectedly, Mn^{2+} alone was capable of inducing significant acceleration of NTase activity, with the EC_{50} resting around 1-2mM in the context of low and high free Mg^{2+} (Figure 2B). As expected, magnesium was unable to achieve activation of cGAS in the absence of dsDNA (Figure 2 – figure supplement 2A). The Hill coefficient was near 2 for Mn^{2+} suggesting the utilization of Mn^{2+} in the absence of dsDNA is cooperative. To test if Mn^{2+} was sufficient to activate cGAS in the complete absence of Mg^{2+}, the steady state activity of cGAS was measured as a function of substrate concentration in buffer containing only Mn^{2+} (Figure 2D). Here, cGAS remained activated with Mn^{2+} alone and displayed rates comparable to those under saturating concentrations of dsDNA. Remarkably, these observations indicate that Mn^{2+} can override the allosteric network, albeit only at concentrations well beyond those found in physiological settings.

If dsDNA was no longer required for activation, it seemed logical to test whether dimerization was also dispensable for activation, given the thermodynamic linkage between dsDNA binding and dimerization. To test this, the NTase activity of dimerization-null mutant, K394E-$cGAS^{FL}$, was assayed. Mn^{2+} titrations showed a near identical trend relative to WT $cGAS^{FL}$ indicating that Mn^{2+} could activate monomeric cGAS (Figure 2C). Substrate titrations in the presence of saturating Mn^{2+} and absence of Mg^{2+} (Figure 2D) also showed marked increases in catalytic efficiency confirming that dimerization is not required for auto-activation by Mn^{2+}.

Mn^{2+} binding is functionally coupled to dsDNA binding

Although Mn^{2+} can auto-activate monomeric and dimeric cGAS, the concentration of Mn^{2+} required to achieve appreciable activity is not physiological (Bowman and Aschner 2014). However, the dramatic difference in functional binding affinity for Mn^{2+} in the presence and absence of dsDNA implied the existence of a thermodynamic linkage between the functional binding affinity of dsDNA and Mn^{2+}. To test if Mn^{2+} could increase the functional binding affinity for dsDNA, the NTase activity of $cGAS^{FL}$ was measured as a function of different dsDNAs in the presence and absence of Mn^{2+}. $cGAS^{FL}$ demonstrated increases in maximal catalytic turnover, k_{max}, in the presence of 50μM Mn^{2+}, consistent with Figure 2, but minimal changes in dsDNA functional binding affinity, K_{act} (Figure 3C, 3D). However, the minimal change in K_{act} could be misleading due to the sub-saturating Mn^{2+} levels and limited accessible range of binding affinities; the lowest practical concentration of $cGAS^{FL}$ is 10nM.

To better quantify the extent by which Mn^{2+} could enhance dsDNA binding, $cGAS^{cat}$ was assayed with saturating levels of Mn^{2+}. $cGAS^{cat}$ has weaker inherent binding affinity for dsDNA and would thus expand the range of experimentally accessible binding affinities, while saturating Mn^{2+} should maximize differences in binding affinity. We confirmed that $cGAS^{cat}$ was activated by Mn^{2+} in a similar manner and extent as $cGAS^{FL}$ (Figure 3 – figure supplement 1A). In the absence of Mn^{2+}, $cGAS^{cat}$ demonstrated dsDNA length-dependent activation; the concentration of dsDNA required to achieve half-maximal activation, K_{act}, was tiered with dsDNA length, consistent with our previous work (Figure 3A and 3B). In the presence of Mn^{2+}, the maximal rates increased and the concentration of dsDNA required to achieve half-maximal activation was severely depressed. These results support the idea that Mn^{2+} binding is functionally coupled to dsDNA binding. The shift in K_{act} was seen for both dsDNA lengths and was similar in magnitude as the change in Mn^{2+} EC_{50}s, suggesting most of the coupling energy is accounted for by dsDNA and Mn^{2+} cooperativity. Together, these data support the hypothesis that cGAS is sensitized by Mn^{2+} due to an intimate coupling between functional dsDNA binding and Mn^{2+} binding.

The shift in K_{act} for short dsDNAs again suggested that monomeric cGAS may also be activated by dsDNA in the presence of Mn^{2+}. Preliminary data with K394E-$cGAS^{FL}$ and K394E-$cGAS^{cat}$ suggests that dsDNA increases the efficiency of Mn^{2+} utilization (EC_{50}) while reducing cooperativity, consistent with wild-type $cGAS^{FL}$ (data not shown). This predicts that Mn^{2+} will reduce the K_{act} of dsDNAs for K394E-cGAS. This will be tested in the future.

Figure 3

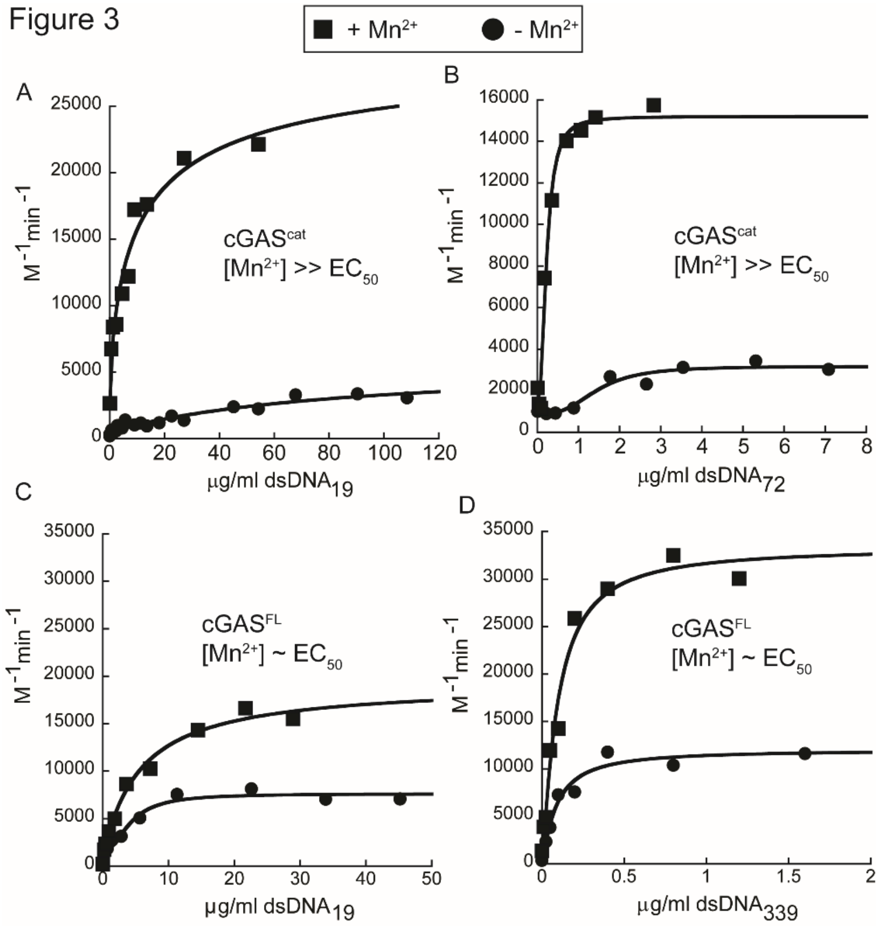

Figure 3. Mn^{2+} enhances the functional binding affinity of dsDNA.

A) Steady-state activity of $cGAS^{cat}$ as a function of $dsDNA_{19}$ or B) $dsDNA_{72}$ in 5mM Mg^{2+} buffer in the presence and absence of 250µM Mn^{2+}. Reaction conditions: 100µM ATP/GTP : 2 Mg^{2+}, 25nM cGAS, 50nM PP_iase. Data were fit with the Hill form of the Michaelis-Menten equation: $(k_{max}\text{-}k_{min}) * (1 / (1+(EC_{50} / [Mn^{2+}])^{Hill}) + k_{min}$. Parameters to the fits are shown in tables below each graph; n = 1.

C) Steady-state activity of $cGAS^{FL}$ as a function of $dsDNA_{19}$ or D) $dsDNA_{339}$ in 5mM Mg^{2+} buffer in the presence and absence of 50µM Mn^{2+}. Reaction conditions: 150□M ATP/GTP : 2 Mg^{2+}, 25nM cGAS, 50nM PP_iase. Data were fit with the Hill form of the Michaelis-Menten equation: $(k_{max}\text{-}k_{min}) * (1 / (1+(EC_{50} / [Mn^{2+}])^{Hill}) + k_{min}$.

Figure 3 - figure supplement 1

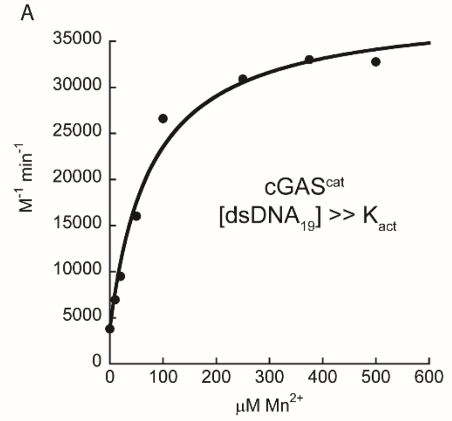

Table 4. cGAS^{cat} activation parameters in the presence and absence of 250μM supplemented Mn^{2+}

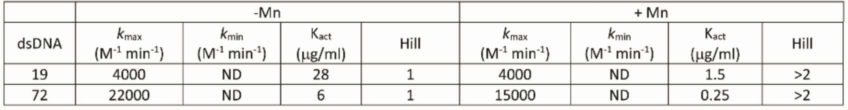

	-Mn				+ Mn			
dsDNA	k_{max} (M^{-1} min^{-1})	k_{min} (M^{-1} min^{-1})	K_{act} (μg/ml)	Hill	k_{max} (M^{-1} min^{-1})	k_{min} (M^{-1} min^{-1})	K_{act} (μg/ml)	Hill
19	4000	ND	28	1	4000	ND	1.5	>2
72	22000	ND	6	1	15000	ND	0.25	>2

Table 5. cGAS^{FL} activation parameters in the presence and absence of 50μM supplemented Mn^{2+}

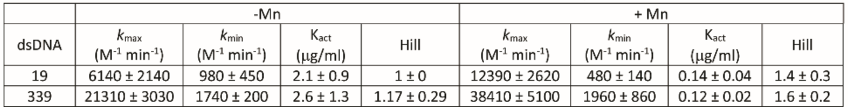

	-Mn				+ Mn			
dsDNA	k_{max} (M^{-1} min^{-1})	k_{min} (M^{-1} min^{-1})	K_{act} (μg/ml)	Hill	k_{max} (M^{-1} min^{-1})	k_{min} (M^{-1} min^{-1})	K_{act} (μg/ml)	Hill
19	6140 ± 2140	980 ± 450	2.1 ± 0.9	1 ± 0	12390 ± 2620	480 ± 140	0.14 ± 0.04	1.4 ± 0.3
339	21310 ± 3030	1740 ± 200	2.6 ± 1.3	1.17 ± 0.29	38410 ± 5100	1960 ± 860	0.12 ± 0.02	1.6 ± 0.2

Figure 3 – figure supplement 1. Physiological concentrations of Mn^{2+} enhances catalytic turnover of cGAS^{FL}.

A) Steady-state rates of cGAS^{cat} as a function of Mn^{2+} concentration in 5mM Mg^{2+} buffer in the presence of saturating dsDNA$_{19}$. Reaction conditions: 200uM ATP/GTP : 2 Mg^{2+}, 25nM cGAS^{FL}, 50nM PP$_i$ase; [dsDNA] = 6x K$_{act}$. Data were fit with the Hill form of the Michaelis-Menten equation: (k_{max}-k_{min}) * (1 / (1+(EC$_{50}$ / [Mn^{2+}])^{Hill}) + k_{min}; n = 1.

Table 4. Steady-state activity constants of cGAS^{cat} in the presence and absence of 250□M Mn^{2+} as a function of dsDNA concentration; from Figure 3. The error is standard deviation of individual fits. Each experiment was performed at least three times.

Table 5. Steady-state activity constants of cGAS^{FL} in the presence and absence of 50μM Mn^{2+} as a function of dsDNA concentration; from Figure 3. n = 1.

Manganese accelerates cGAMP production

Enzymes that typically utilize Mg^{2+} as a Lewis acid often retain activity when Mg^{2+} is replaced with Mn^{2+}. In the case of nucleotidyl transferases, Mn^{2+} substitution can result in faster turnover, but can also cause a reduction in product fidelity (Vaisman et al. 2005; Frank and Woodgate 2007; Vashishtha, Wang, and Konigsberg 2016; Crespan et al. 2016). Our PP_iase-coupled assay demonstrates that Mn^{2+} supports faster turnover of substrate by cGAS, but it remained unclear whether cGAMP was the primary product of catalysis. To identify and quantify the products of catalysis, cGAS reactions were fractionated by HPLC. Synthetic standards and purified reaction products were used to determine the identity of individual species by matching retention times (Figure 4A). Exact mass will be used in the future to aid in peak identification. Consistent with previous literature, $cGAS^{FL}$ stimulated by dsDNA under steady state conditions produced primarily two products in the presence of ATP/GTP, namely cGAMP and (likely) pppGpA (Figure 4A) (Hall, Ralph, et al. 2017b). In the absence of dsDNA, $cGAS^{FL}$ showed no detectable activity. Interestingly, the amount of cGAMP increased with dsDNA length (Figure 4B), while the pppGpA intermediate level was constant (Figure 4C). This observation highlights another key finding in cGAS dsDNA-length dependent signaling in that cGAMP production is tiered by the length of activating dsDNA. Importantly, the differences in cGAMP levels between dsDNA lengths was reduced under conditions of high enzyme concentration (Figure 4D), reiterating the idea that dsDNA length-dependent activity is context-specific (Hooy and Sohn 2018). Of note, at higher cGAS concentrations, a pppGpG peak was present only for the short dsDNA activator (Figure 5 – figure supplement 1A). This may suggest that product fidelity may also be linked to dsDNA length.

Figure 4

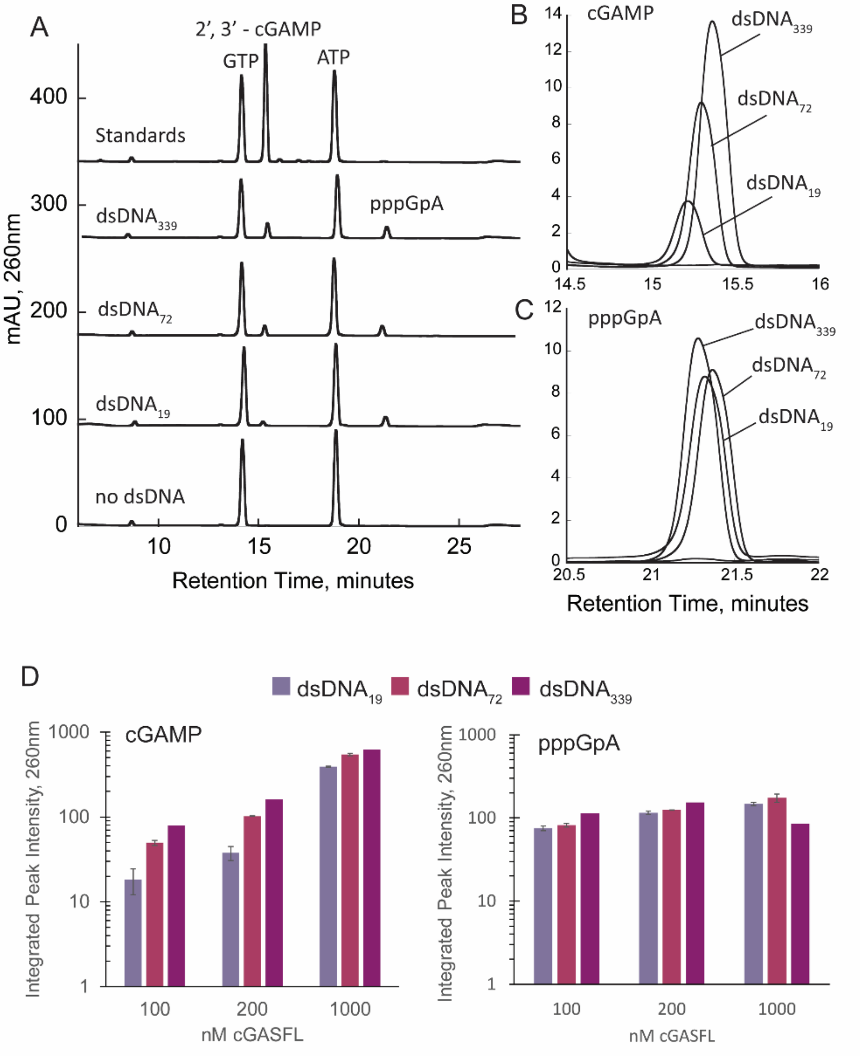

Figure 4. In the absence of Mn^{2+}, cGAMP levels tier with dsDNA length.

A) Reverse phase HPLC fractionation of cGAS reaction components. Raw absorbance traces are shown for $cGAS^{FL}$ in the presence and absence of saturating dsDNA. Standards of ATP, GTP and synthetic 2', 3' – cGAMP indicate respective retention times. Reaction conditions: 250µM ATP/GTP : 2 Mg^{2+}, 200nM $cGAS^{FL}$; [dsDNA] = 6x K_{act}, where indicated; reactions were run for 2 hours prior to quenching, filtering and fractionation by HPLC.

B) Zoom-in and overlay of the cGAMP peak and C) pppGpA peak for each of the reactions in a).

D) Integrated peak intensities of cGAMP (left) and pppGpA (right) for various reaction conditions. All reactions were run for 2 hours. Error bars indicate standard deviation of technical replicates.

Next, we tested how Mn^{2+} affected the distribution of reaction products. $cGAS^{FL}$ reactions supplemented with 50uM Mn^{2+} had a global increase in cGAMP and pppGpA levels for all dsDNA lengths (Figure 5A), in agreement with results obtained from the PP_iase-coupled assay. For lower cGAS concentrations, this reduced the difference in cGAMP levels between long and short dsDNA from four-fold to two-fold. Importantly, this reduced length-dependence would imply that any residual dsDNA length dependence would result almost exclusively from differences in dsDNA binding affinity. Also of note, the pppGpG peak observed at high cGAS concentrations was reduced with Mn^{2+} present, suggesting that low levels of Mn^{2+} may also increase substrate stringency (see below) (Figure 5 – figure supplement 1).

Although low levels of Mn^{2+} did not negatively skew the product fidelity, it remained unclear if high Mg^{2+} or dsDNA could be biasing substrate selection. Thus, reactions with and without dsDNA under auto-activating levels of Mn^{2+} were tested. $cGAS^{FL}$ and K394E-$cGAS^{FL}$ produced primarily on-pathway products without dsDNA, reiterating that cGAS preferentially couples ATP and GTP (Vincent et al. 2017) and that dsDNA is not required for cGAMP production (Figure 5). Reactions with dsDNA, however, did produce greater amounts of pppGpA (on-pathway) without greatly inflating total off-product synthesis (Figure 5 – figure supplement 1 Table). This suggests that dsDNA enhances the fidelity of substrate selection even under auto-activating conditions, e.g high Mn^{2+}.

dsDNA and Mn^{2+} promote ATP/GTP coupling under physiological conditions

Thus far, our assays were performed with equimolar concentrations of ATP and GTP. However, in the cell, ATP outnumbers GTP by several fold (Traut 1994). Hence, even though cGAS demonstrated strong ATP/GTP coupling, it remained to be tested how Mn^{2+}, cGAS concentration and dsDNA length affected substrate selection under more physiological conditions. Reactions with a 4:1 ratio of ATP to GTP were assessed for relative product distribution in the presence and absence of 50□M Mn^{2+} (Figure 5C). In the absence of Mn^{2+} cGAS produced primarily pppGpA and cGAMP, and some pppApA. When compared to Mn^{2+}-supplemented reactions, despite elevated catalytic rates and relatively high ATP, only on-pathway products, pppGpA and cGAMP, were significantly elevated in the presence of Mn^{2+}; pppApA levels were virtually unaffected by the addition of Mn^{2+}. In contrast, under auto-activating levels of Mn^{2+}, pppApA contributed significantly to the product pool (Figure 5D). However, the addition of dsDNA selectively promoted on-pathway catalysis, by reducing ATP/ATP coupling and increasing ATP/GTP pairing. These data emphasize that allosteric control of cGAS activity ensures high fidelity signaling by providing a robust threshold for substrate selection and catalysis.

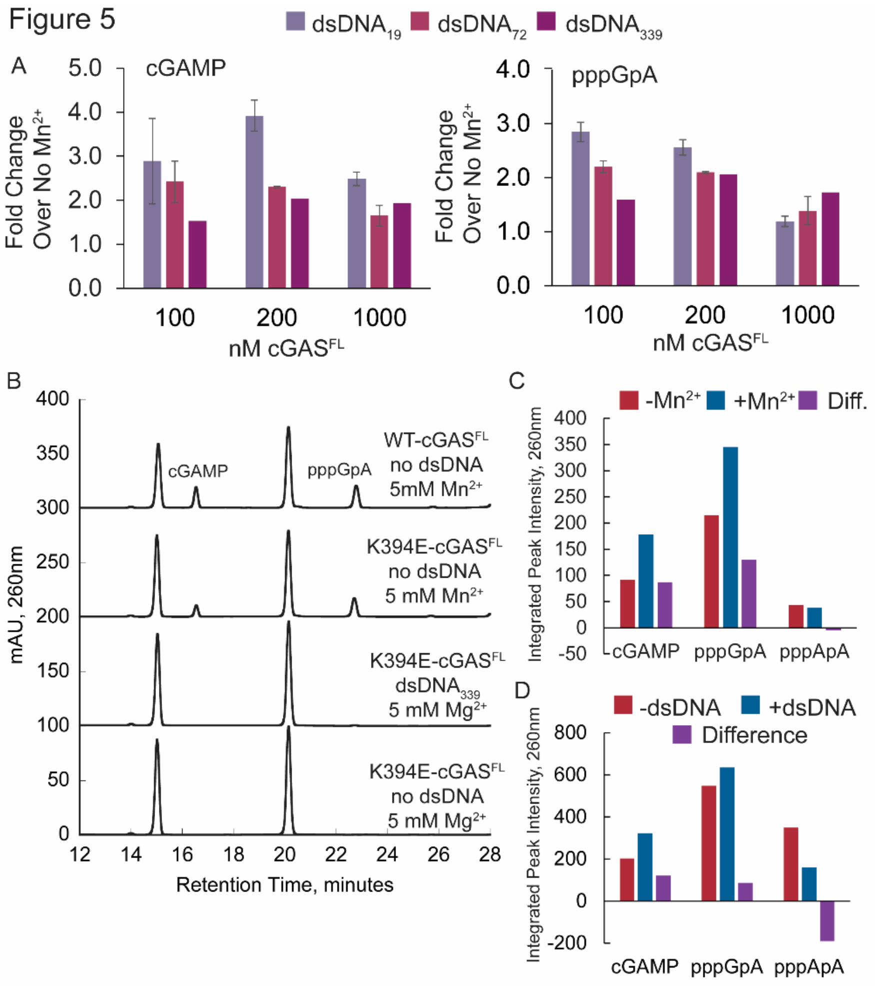

Figure 5. Mn^{2+} and dsDNA specifically enhance on-pathway catalysis.

A) Normalized integrated peak intensities of cGAMP (left) and pppGpA (right) from reactions supplemented with or without 50µM Mn^{2+}. All reactions were run for 2 hours. Error bars indicate standard deviation of technical replicates.

B) Raw absorbance traces of fractionated reaction components of K394E-cGAS^{FL} and cGAS^{FL} reactions under various conditions. Reaction conditions: 250µM ATP/GTP : 2 Mg^{2+}(lower two traces) or Mn^{2+} (upper two traces), 200nM cGAS; 5 µg/ml dsDNA, where indicated; reactions were run for 2 hours prior to quenching, filtering and fractionation by HPLC.

C) Integrated peak intensities of cGAMP, pppGpA and pppApA for reactions supplemented with or without 50μM Mn^{2+} in 5mM Mg^{2+} buffer. Reaction conditions: 1mM ATP : Mg^{2+}, 250□M GTP : Mg^{2+}, 200nM cGAS; 5 μg/ml dsDNA, where indicated. Reactions were run for 2 hours.

d) Integrated peak intensities of cGAMP, pppGpA and pppApA for reactions with or without $dsDNA_{339}$ in 5mM Mn^{2+} buffer. Reaction conditions: 1mM ATP : Mg^{2+}, 250μM GTP : Mg^{2+}, 200nM cGAS; 5 μg/ml dsDNA, where indicated. Reactions were run for 2 hours.

Figure 5 - figure supplement 1

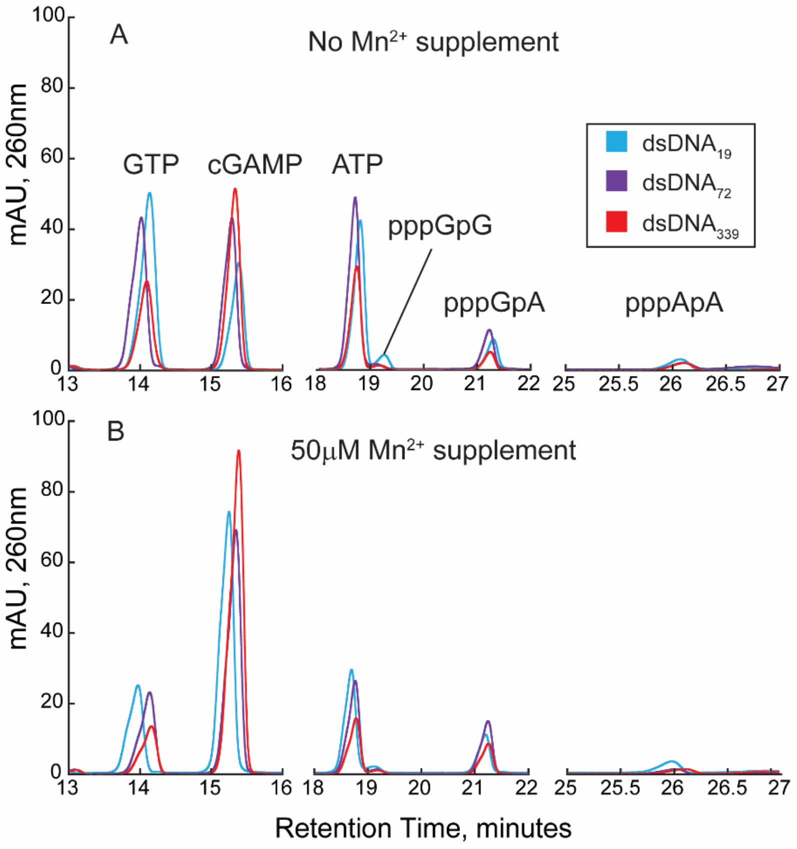

Table 6. Integrated Intensities of reaction products under auto-activating levels of Mn^{2+}

	- dsDNA	+ dsDNA	Change
cGAMP	383.9	334	-49.9
pppGpA	267.6	453	185.4
pppApA	71.2	37	-34.2
pppGpG	25.1	77	51.9

Figure 5 – figure supplement 1. Mn^{2+} and dsDNA affect substrate selection.

A) Raw absorbance traces of fractionated $cGAS^{FL}$ reactions. Reactions contained different lengths of dsDNA in 5mM Mg^{2+} buffer in the presence and b) absence of 50µM Mn^{2+}. Reaction conditions: 250µM ATP/GTP : 2 Mg^{2+}, 1µM cGAS; dsDNA binding sites were in molar excess of cGAS by 1.5-fold (1 binding site is equivalent to 18bps); reactions were run for 2 hours prior to quenching, filtering and fractionation by HPLC.

Table 6. Integrated peak intensities of reaction products under auto-activating levels of Mn^{2+} for $cGAS^{FL}$ in the presence and absence of dsDNA. Reaction conditions: 250μM ATP/GTP : 2 Mn^{2+}, 200nM cGAS, 5μg/ml $dsDNA_{339}$ where indicated; where indicated; reactions were run for 2 hours prior to quenching, filtering and fractionation by HPLC.

Discussion

Wang, *et al.* 2018 discovered an unidentified role of manganese in the innate immune response to pathogen challenge, and more generally, to cytosolic dsDNA. Although a clear relationship between the dsDNA sensor, cGAS, and manganese was established, the molecular mechanism by which manganese exerted its effects was ill-defined. Here, we determined the mechanism by which Mn^{2+} 'sensitizes' cGAS towards dsDNA.

The effect of Mn^{2+}-mediated activation

We first established that Mn^{2+} enhances the activity of cGAS towards all lengths of dsDNA *in vitro* (Figure 1A). Moreover, cell-based experiments have shown that this effect can essentially eliminate the dsDNA length-dependent response in cells (data not shown; Chattergoon Lab). In principle, cGAS dsDNA length-dependent activity would be dictated by the concentration of cGAS and substrates in the cell (Hooy and Sohn 2018). cGAS is only marginally upregulated by interferon signaling (Ma et al. 2015), and our *in vitro* assays indicated that the effect of Mn^{2+} is achieved even with fixed levels of substrate (Figure 1A). This suggested then that Mn^{2+} likely affected an alternative aspect of the allosteric system, such as dimerization and/or catalytic states (Figure 1B). Mn^{2+} did not affect dimerization (Figure 2 – figure supplement 1). Instead, at high concentrations, Mn^{2+} was found to auto-activate monomeric and dimeric cGAS. This was somewhat surprising, given Wang, *et al.* 2018, failed to observe IRF3 phosphorylation in permeabilized THP-1 dual cells treated with cGAS reactions supplemented with auto-activating levels of Mn^{2+}. Notably, the discrepancy is not due to an inability of auto-activated cGAS to produce cGAMP (Figure 5B). It is possible that the higher enzyme concentrations and elevated reaction temperatures used in the previous study had adverse effect on cGAS stability, that only dsDNA (the cognate activator) could otherwise provide (Waldron and Murphy 2003; Cimmperman et al. 2008; Rupesh, Smith, and Boehmer 2014). It is worth noting, however, that HeLa cells significantly depleted of mitochondrial DNA still produced a Mn^{2+}/cGAS-dependent response. This potentially suggests that auto-activation of cGAS can be achieved in cells, although it remains unclear if other sources of dsDNA contributed to the observed activity. Moreover, Mn^{2+} is a known mutagen (Demerec and Hanson 1951), and induction of the DNA-damage response could provide a source of cytosolic dsDNA, independent of reactive oxygen species (Wang, Guan, et al. 2018; Rodier et al. 2009; Hartlova et al. 2015; Yu et al. 2015).

Although Mn^{2+} can auto-activate cGAS, the concentrations required to achieve meaningful activity are well-beyond those seen in physiology. However, we observed a strong functional coupling between dsDNA and Mn^{2+} supporting the idea that dsDNA may still be required to activate cGAS in cells. This coupled relationship also revealed that Mn^{2+} has a profound effect on the functional binding affinity for dsDNA, perhaps indicating how Mn^{2+} sensitizes cGAS to dsDNA. It remains unclear if the pronounced functional coupling occurs strictly in the dimer, or also within the monomer. One key experiment that will help answer this question is determining whether Mn^{2+} affects substrate-induced dimerization. Depending on the outcome, my data could support one of two models. If Mn^{2+} negligibly affects substrate-induced dimerization, it is likely that dsDNA-bound monomeric cGAS is activated in the presence of Mn^{2+}. If Mn^{2+} does positively affect substrate-induced dimerization, it is likely then that the Mn^{2+}-substrate complex biases the allosteric equilibrium towards the dimeric state. In either case, each model would predict the following: a) in the presence of Mn^{2+} and saturating dsDNA, short dsDNAs activate cGAS as well as long dsDNAs, and b) cGAS displays Mn^{2+}-dependent loss of cooperativity in substrate utilization *and* dsDNA binding. The ‘active monomer’ model would also predict that a dimerization-null mutant would functionally couple dsDNA binding to Mn^{2+} utilization, whereas the ‘Mn^{2+}-dimer’ model would predict that the mutant’s activity would be minimally impacted by the presence of dsDNA.

Manganese as a cofactor

Nucleotidyl transferases typically use magnesium as a cofactor for catalysis, but in many instances, manganese is a serviceable substitute (Vashishtha, Wang, and Konigsberg 2016), if not the preferential cofactor (Jiang et al. 2011). Many enzymes likely evolved to use magnesium as a cofactor due to its chemical properties and shear abundance in the cell. Cellular Mg^{2+} concentrations rest in the 5-20mM range (Romani and Scarpa 1992), whereas Mn^{2+} is rarely observed above 50□M. From the physical chemistry perspective, Mg^{2+} orbitals preferentially adopt the octahedral arrangements ideal for Lewis acid catalysis within the active site of polymerases. In contrast, Mn^{2+} can adopt alternative geometries and is more malleable with respect to ligand bond distances (Vashishtha, Wang, and Konigsberg 2016). Thus, despite its similar effectiveness as a Lewis acid, it can reduce substrate restrictions, leading to misincorporation of cognate nucleotides by polymerases, for instance. cGAS produced significant amounts of pppApA when ATP was in excess over GTP. However, under low manganese concentrations, product fidelity was preserved even with excess ATP over GTP and faster overall catalytic rates. These observations indicate that the allosteric framework maintains the highest threshold for substrate selection.

Manganese as an auto-activator

cGAS is unique in that its allosteric activator, dsDNA, regulates the spatial arrangement of its active site. In principle, molecules bound within the active site can promote the same re-arrangement. Indeed, this effect likely contributes to the observed cooperativity between substrate and dsDNA binding. However, the observed auto-activation by Mn^{2+} suggests that Mn^{2+}, in the presence of nucleotide, possesses the ability to not only stabilize the active, structured conformer of the activation loop, but also to trigger catalysis. It remains unclear if this effect is due to novel structural differences promoted by Mn^{2+} or discrepancies in substrate:metal binding kinetics.

Efficient and effective signaling

Here, we provide evidence to suggest that cGAS preferentially pairs ATP and GTP over either homo-dinucleotide pair, even in the presence of excess ATP and physiological levels of Mn^{2+}. The proper selection of nucleotide pairs is paramount for cGAS for two main reasons. First, due to the relatively slow rate of catalysis, cGAS must perform high fidelity reactions to avoid wasted catalytic cycles. Second, human STING and its natural variants are hyper selective towards the identity of nucleobases and linkage within the cyclic dinucleotide (Ablasser et al. 2013; Diner et al. 2013; Zhang et al. 2013). Improper coupling of nucleotides by cGAS would impinge on its ability to effectively communicate the presence of stress. However, it remains unclear if cGAS actually maintains high levels of product fidelity in vivo, or if 'sloppy' catalysis is naturally built into the stress sensor. Evidence supporting this hypothesis is provided by the notable differences between mouse and human homologs of cGAS and STING. The mouse homolog of cGAS (mcGAS) turns over roughly ten-times faster than its human counterpart (Vincent et al. 2017; Zhou et al. 2018), and its downstream adaptor, mSTING, is activated by a broader range of cyclic dinucleotides (Zhang et al. 2013; Wang, Sinn, et al. 2017). This could imply that mcGAS produces molecules other than 2', 3' cGAMP. Moreover, recent data suggests that mcGAS is less stringent towards short dsDNAs (Zhou et al. 2018). Thus, although speculative, it is possible that human cGAS and human STING co-evolved to be a more stringent signaling axis relative to its mouse ancestor. Future studies will reveal just how different the mouse and human systems are.

The molecular basis of substrate selection

Future work aims to more quantitatively determine the means by which ATP/GTP is preferentially selected for catalysis over alternative dinucleotide pairs. Based on our current knowledge, it is likely that substrate selection occurs at multiple steps within the allosteric network.

Substrate-induced dimerization. cGAS FRET experiments have already begun to reveal that individual nucleotides differentially stabilize the cGAS dimeric state. For instance, ATP appears to be more ambivalent towards binding monomeric or dimeric cGAS relative to ATP/GTP. The same is not true for GTP. However, GTP is known to self-associate, especially at high concentrations and in the presence of potassium, and accurate interpretation of this data will require additional controls.

Coupling to dsDNA binding. In reactions containing Mg^{2+}, dsDNA length dictates the fraction of dimeric cGAS, which then dictates the apparent binding affinity for ATP/GTP, e.g. the apparent K_m tiers with dsDNA length. It remains possible that the K_m for ATP or GTP alone is dsDNA length-<u>in</u>dependent, which would skew the catalytic efficiency in favor of ATP/GTP. In reactions with high Mn^{2+}, preliminary evidence suggests that ATP and GTP can be consumed on their own, albeit at relatively slower rates compared to ATP/GTP. Under low Mn^{2+} concentrations, the relative difference in catalytic efficiencies will be dictated by how well dsDNA couples Mn^{2+} binding in the presence of ATP or GTP. For instance, when ATP/GTP is present, the EC_{50} of Mn^{2+} drops by over an order of magnitude under conditions of saturating dsDNA. The same may not be true for ATP or GTP alone.

Catalytic turnover. It is clear from pilot experiments that turnover of GTP is slower than ATP which is slower than ATP/GTP. What remains unclear is by how much. Moreover, how alternative linear dinucleotide pairs affect the synthesis of cognate, pppGpA, remains untested.

Cyclization of dinucleotide intermediates. Reactions containing auto-activating levels of Mn^{2+} and ATP were found to produce almost exclusively pppApA as product. This was surprising as the same reaction with GTP produced a more heterogeneous product distribution that included cyclized diGMP. This implies that cGAS has an intrinsic ability to stymie off-product pathways by reducing cyclization of off-pathway intermediates.

Cyclic dinucleotide phosphodiester linkages. Although the synthetic 2’, 3’-cGAMP standard shares a similar retention time with the cGAMP molecules produced in reactions shown here, it remains to be seen whether the cGAMP molecules produced in the presence of Mn^{2+} are primarily 2’, 3’-linked. Enzymatic digestion and analysis of purified cGAMP molecules will easily determine whether the linkage specificity is subject to manipulation by the metal cofactor.

Concluding remarks

Metals play an essential role in biology. Dietary consumption provides the requisite intake of numerous cations that ultimately contribute to the maintenance of healthy tissues, cells, and a multitude of chemical processes. Unsurprisingly, metal deficiency or excess can lead to serious health issues. Moreover, proper usage, storage and disposal of metals is key for maintaining homeostasis. The results shown here reveal how metal selection can dictate how an enzyme is allosterically regulated. For cGAS, this could affect whether a cell commits to the antiviral response, senescence or cell death. It will be interesting to see if this phenomenon spans to other NTases, and more generally to other magnesium-utilizing enzymes.

Materials and Methods

Reagents

See previous Chapter. Also, $MnCl_2$ was purchased from Sigma. Tetrabutlyammonium hydrogen sulfate was from TCI America. Tris(2-carboxytheyl) phosphine (Tcep) was from Sigma. 2’,3’ cGAMP was from Invitrogen.

Recombinant cGAS purification

Protein preparation. See previous Chapter.

Fluorophore labeling. See previous Chapter.

Biochemical Assays

All experiments were performed at least three times. The fits to data were generated using Kaleidagraph (synergy). Reported values are averages of at least three independent experiments and reported errors are standard deviations. All reactions were performed under 25 mM Tris acetate pH 7.4, 125 mM potassium acetate pH 7.4, 0.5mM Tcep, 5 mM $MgCl_2$, and 5% glycerol at 25 ± 2 °C. cGAS concentrations are noted in the figure legends.

dsDNA binding assays. See previous Chapter. Where indicated, experiments were performed in reaction buffer supplemented with $MnCl_2$.

FRET-based oligomerization assays. See previous Chapter. Where indicted, $MnCl_2$ was supplemented into the reaction buffer. For Mn^{2+} titration experiments, dsDNA was included at concentrations equivalent to its K_{FRET}.

Pyrophosphatase-coupled cGAS activity assay. See previous Chapter and Chapter 2 for full description. Average values and standard deviations are listed in Tables.

Analytical fractionation of cGAS reactions by HPLC

HPLC experiments were performed on the Agilent Technologies 120 Infinity II system using a Poroshell EC-C18 column (2.7µm; 4.6x100mm). cGAS reactions were filtered with 10KDCO spin columns prior to loading onto the column. Reactions were fractionated by the following scheme: 0% B from 0-1min, linear increase to 50% B from 1-27min, linear increase to 100% B from 27-28min. Buffer A: 100mM potassium phosphate monobasic, 5mM TBA, pH 6.0; Buffer B: 100mM potassium phosphate monobasic, 5mM TBA, pH 6.0, 30% acetonitrile. Integrated peak intensities were calculated by the Agilent Technologies ChemStation software. Synthetic and purified compounds were used as standards for peak identification.

References

Ablasser, A., M. Goldeck, T. Cavlar, T. Deimling, G. Witte, I. Rohl, K. P. Hopfner, J. Ludwig, and V. Hornung. 2013. 'cGAS produces a 2'-5'-linked cyclic dinucleotide second messenger that activates STING', *Nature*, 498: 380-4.

Almine, J. F., C. A. O'Hare, G. Dunphy, I. R. Haga, R. J. Naik, A. Atrih, D. J. Connolly, J. Taylor, I. R. Kelsall, A. G. Bowie, P. M. Beard, and L. Unterholzner. 2017. 'IFI16 and cGAS cooperate in the activation of STING during DNA sensing in human keratinocytes', *Nat Commun*, 8: 14392.

Andreeva, L., B. Hiller, D. Kostrewa, C. Lassig, C. C. de Oliveira Mann, D. Jan Drexler, A. Maiser, M. Gaidt, H. Leonhardt, V. Hornung, and K. P. Hopfner. 2017. 'cGAS senses long and HMGB/TFAM-bound U-turn DNA by forming protein-DNA ladders', *Nature*, 549: 394-98.

Biolatti, M., V. Dell'Oste, S. Pautasso, F. Gugliesi, J. von Einem, C. Krapp, M. R. Jakobsen, C. Borgogna, M. Gariglio, M. De Andrea, and S. Landolfo. 2018. 'Human Cytomegalovirus Tegument Protein pp65 (pUL83) Dampens Type I Interferon Production by Inactivating the DNA Sensor cGAS without Affecting STING', *J Virol*, 92.

Bowman, A. B., and M. Aschner. 2014. 'Considerations on manganese (Mn) treatments for in vitro studies', *Neurotoxicology*, 41: 141-2.

Chen, M., Q. Meng, Y. Qin, P. Liang, P. Tan, L. He, Y. Zhou, Y. Chen, J. Huang, R. F. Wang, and J. Cui. 2016. 'TRIM14 Inhibits cGAS Degradation Mediated by Selective Autophagy Receptor p62 to Promote Innate Immune Responses', *Mol Cell*, 64: 105-19.

Cimmperman, P., L. Baranauskiene, S. Jachimoviciute, J. Jachno, J. Torresan, V. Michailoviene, J. Matuliene, J. Sereikaite, V. Bumelis, and D. Matulis. 2008. 'A quantitative model of thermal stabilization and destabilization of proteins by ligands', *Biophys J*, 95: 3222-31.

Civril, F., T. Deimling, C. C. de Oliveira Mann, A. Ablasser, M. Moldt, G. Witte, V. Hornung, and K. P. Hopfner. 2013. 'Structural mechanism of cytosolic DNA sensing by cGAS', *Nature*, 498: 332-7.

Crespan, E., A. Furrer, M. Rosinger, F. Bertoletti, E. Mentegari, G. Chiapparini, R. Imhof, N. Ziegler, S. J. Sturla, U. Hubscher, B. van Loon, and G. Maga. 2016. 'Impact of ribonucleotide incorporation by DNA polymerases beta and lambda on oxidative base excision repair', *Nat Commun*, 7: 10805.

Demerec, M., and J. Hanson. 1951. 'MUTAGENIC ACTION OF MANGANOUS CHLORIDE', *Cold Spring Harb Symp Quant Biol*, 16: 215-28.

Diner, E. J., D. L. Burdette, S. C. Wilson, K. M. Monroe, C. A. Kellenberger, M. Hyodo, Y. Hayakawa, M. C. Hammond, and R. E. Vance. 2013. 'The innate immune DNA sensor cGAS produces a noncanonical cyclic dinucleotide that activates human STING', *Cell Rep*, 3: 1355-61.

Du, M., and Z. J. Chen. 2018. 'DNA-induced liquid phase condensation of cGAS activates innate immune signaling', *Science*, 361: 704-09.

Frank, E. G., and R. Woodgate. 2007. 'Increased catalytic activity and altered fidelity of human DNA polymerase iota in the presence of manganese', *J Biol Chem*, 282: 24689-96.

Gao, P., M. Ascano, Y. Wu, W. Barchet, B. L. Gaffney, T. Zillinger, A. A. Serganov, Y. Liu, R. A. Jones, G. Hartmann, T. Tuschl, and D. J. Patel. 2013. 'Cyclic [G(2',5')pA(3',5')p] is the metazoan second messenger produced by DNA-activated cyclic GMP-AMP synthase', *Cell*, 153: 1094-107.

Gluck, S., B. Guey, M. F. Gulen, K. Wolter, T. W. Kang, N. A. Schmacke, A. Bridgeman, J. Rehwinkel, L. Zender, and A. Ablasser. 2017. 'Innate immune sensing of cytosolic chromatin fragments through cGAS promotes senescence', *Nat Cell Biol*, 19: 1061-70.

Gulen, M. F., U. Koch, S. M. Haag, F. Schuler, L. Apetoh, A. Villunger, F. Radtke, and A. Ablasser. 2017. 'Signalling strength determines proapoptotic functions of STING', *Nat Commun*, 8: 427.

Hall, J., A. Brault, F. Vincent, S. Weng, H. Wang, D. Dumlao, A. Aulabaugh, D. Aivazian, D. Castro, M. Chen, J. Culp, K. Dower, J. Gardner, S. Hawrylik, D. Golenbock, D. Hepworth, M. Horn, L. Jones, P. Jones, E. Latz, J. Li, L. L. Lin, W. Lin, D. Lin, F. Lovering, N. Niljanskul, R. Nistler, B. Pierce, O. Plotnikova, D. Schmitt, S. Shanker, J. Smith, W. Snyder, T. Subashi, J. Trujillo, E. Tyminski, G. Wang, J. Wong, B. Lefker, L. Dakin, and K. Leach. 2017. 'Discovery of PF-06928215 as a high affinity inhibitor of cGAS enabled by a novel fluorescence polarization assay', *PLoS One*, 12: e0184843.

Hall, J., E. C. Ralph, S. Shanker, H. Wang, L. J. Byrnes, R. Horst, J. Wong, A. Brault, D. Dumlao, J. F. Smith, L. A. Dakin, D. C. Schmitt, J. Trujillo, F. Vincent, M. Griffor, and A. E. Aulabaugh. 2017. 'The catalytic mechanism of cyclic GMP-AMP synthase (cGAS) and implications for innate immunity and inhibition', *Protein Sci*, 26: 2367-80.

Harding, S. M., J. L. Benci, J. Irianto, D. E. Discher, A. J. Minn, and R. A. Greenberg. 2017. 'Mitotic progression following DNA damage enables pattern recognition within micronuclei', *Nature*, 548: 466-70.

Hartlova, A., S. F. Erttmann, F. A. Raffi, A. M. Schmalz, U. Resch, S. Anugula, S. Lienenklaus, L. M. Nilsson, A. Kroger, J. A. Nilsson, T. Ek, S. Weiss, and N. O. Gekara. 2015. 'DNA damage primes the type I interferon system via the cytosolic DNA sensor STING to promote anti-microbial innate immunity', *Immunity*, 42: 332-43.

Hooy, R. M., and J. Sohn. 2018. 'The allosteric activation of cGAS underpins its dynamic signaling landscape', *Elife*, 7.

Hu, M. M., Q. Yang, X. Q. Xie, C. Y. Liao, H. Lin, T. T. Liu, L. Yin, and H. B. Shu. 2016. 'Sumoylation Promotes the Stability of the DNA Sensor cGAS and the Adaptor STING to Regulate the Kinetics of Response to DNA Virus', *Immunity*, 45: 555-69.

Ishikawa, H., Z. Ma, and G. N. Barber. 2009. 'STING regulates intracellular DNA-mediated, type I interferon-dependent innate immunity', *Nature*, 461: 788-92.

Jiang, H., L. Weng, N. Zhang, M. Arita, R. Li, L. Chen, and T. Toyoda. 2011. 'Biochemical characterization of enterovirus 71 3D RNA polymerase', *Biochim Biophys Acta*, 1809: 211-9.

Li, X., C. Shu, G. Yi, C. T. Chaton, C. L. Shelton, J. Diao, X. Zuo, C. C. Kao, A. B. Herr, and P. Li. 2013. 'Cyclic GMP-AMP synthase is activated by double-stranded DNA-induced oligomerization', *Immunity*, 39: 1019-31.

Lian, H., J. Wei, R. Zang, W. Ye, Q. Yang, X. N. Zhang, Y. D. Chen, Y. Z. Fu, M. M. Hu, C. Q. Lei, W. W. Luo, S. Li, and H. B. Shu. 2018. 'ZCCHC3 is a co-sensor of cGAS for dsDNA recognition in innate immune response', *Nat Commun*, 9: 3349.

Liu, Z. S., Z. Y. Zhang, H. Cai, M. Zhao, J. Mao, J. Dai, T. Xia, X. M. Zhang, and T. Li. 2018. 'RINCK-mediated monoubiquitination of cGAS promotes antiviral innate immune responses', *Cell Biosci*, 8: 35.

Luecke, S., A. Holleufer, M. H. Christensen, K. L. Jonsson, G. A. Boni, L. K. Sorensen, M. Johannsen, M. R. Jakobsen, R. Hartmann, and S. R. Paludan. 2017. 'cGAS is activated by DNA in a length-dependent manner', *EMBO Rep*, 18: 1707-15.

Ma, F., B. Li, S. Y. Liu, S. S. Iyer, Y. Yu, A. Wu, and G. Cheng. 2015. 'Positive feedback regulation of type I IFN production by the IFN-inducible DNA sensor cGAS', *J Immunol*, 194: 1545-54.

Mackenzie, K. J., P. Carroll, C. A. Martin, O. Murina, A. Fluteau, D. J. Simpson, N. Olova, H. Sutcliffe, J. K. Rainger, A. Leitch, R. T. Osborn, A. P. Wheeler, M. Nowotny, N. Gilbert, T. Chandra, M. A. M. Reijns, and A. P. Jackson. 2017. 'cGAS surveillance of micronuclei links genome instability to innate immunity', *Nature*, 548: 461-65.

Riley, J. S., G. Quarato, C. Cloix, J. Lopez, J. O'Prey, M. Pearson, J. Chapman, H. Sesaki, L. M. Carlin, J. F. Passos, A. P. Wheeler, A. Oberst, K. M. Ryan, and S. W. Tait. 2018. 'Mitochondrial inner membrane permeabilisation enables mtDNA release during apoptosis', *EMBO J*, 37.

Rodier, F., J. P. Coppe, C. K. Patil, W. A. Hoeijmakers, D. P. Munoz, S. R. Raza, A. Freund, E. Campeau, A. R. Davalos, and J. Campisi. 2009. 'Persistent DNA damage signalling triggers senescence-associated inflammatory cytokine secretion', *Nat Cell Biol*, 11: 973-9.

Romani, A., and A. Scarpa. 1992. 'Regulation of cell magnesium', *Arch Biochem Biophys*, 298: 1-12.

Rupesh, K. R., A. Smith, and P. E. Boehmer. 2014. 'Ligand induced stabilization of the melting temperature of the HSV-1 single-strand DNA binding protein using the thermal shift assay', *Biochem Biophys Res Commun*, 454: 604-8.

Seo, G. J., C. Kim, W. J. Shin, E. H. Sklan, H. Eoh, and J. U. Jung. 2018. 'TRIM56-mediated monoubiquitination of cGAS for cytosolic DNA sensing', *Nat Commun*, 9: 613.

Seo, G. J., A. Yang, B. Tan, S. Kim, Q. Liang, Y. Choi, W. Yuan, P. Feng, H. S. Park, and J. U. Jung. 2015. 'Akt Kinase-Mediated Checkpoint of cGAS DNA Sensing Pathway', *Cell Rep*, 13: 440-9.

Shannon, J. L., M. S. Murphy, U. Kantheti, J. M. Burnett, M. G. Hahn, T. J. Dorrity, C. J. Bacas, E. B. Mattice, K. D. Corpuz, and B. R. Barker. 2018. 'Polyglutamine binding protein 1 (PQBP1) inhibits innate immune responses to cytosolic DNA', *Mol Immunol*, 99: 182-90.

Shu, C., X. Li, and P. Li. 2014. 'The mechanism of double-stranded DNA sensing through the cGAS-STING pathway', *Cytokine Growth Factor Rev*, 25: 641-8.

Sun, L., J. Wu, F. Du, X. Chen, and Z. J. Chen. 2013. 'Cyclic GMP-AMP synthase is a cytosolic DNA sensor that activates the type I interferon pathway', *Science*, 339: 786-91.

Tao, J., X. W. Zhang, J. Jin, X. X. Du, T. Lian, J. Yang, X. Zhou, Z. Jiang, and X. D. Su. 2017. 'Nonspecific DNA Binding of cGAS N Terminus Promotes cGAS Activation', *J Immunol*, 198: 3627-36.

Traut, T. W. 1994. 'Physiological concentrations of purines and pyrimidines', *Mol Cell Biochem*, 140: 1-22.

Vaisman, A., H. Ling, R. Woodgate, and W. Yang. 2005. 'Fidelity of Dpo4: effect of metal ions, nucleotide selection and pyrophosphorolysis', *EMBO J*, 24: 2957-67.

Vashishtha, A. K., J. Wang, and W. H. Konigsberg. 2016. 'Different Divalent Cations Alter the Kinetics and Fidelity of DNA Polymerases', *J Biol Chem*, 291: 20869-75.

Vincent, J., C. Adura, P. Gao, A. Luz, L. Lama, Y. Asano, R. Okamoto, T. Imaeda, J. Aida, K. Rothamel, T. Gogakos, J. Steinberg, S. Reasoner, K. Aso, T. Tuschl, D. J. Patel, J. F. Glickman, and M. Ascano. 2017. 'Small molecule inhibition of cGAS reduces interferon expression in primary macrophages from autoimmune mice', *Nat Commun*, 8: 750.

Waldron, T. T., and K. P. Murphy. 2003. 'Stabilization of proteins by ligand binding: application to drug screening and determination of unfolding energetics', *Biochemistry*, 42: 5058-64.

Wang, C., Y. Guan, M. Lv, R. Zhang, Z. Guo, X. Wei, X. Du, J. Yang, T. Li, Y. Wan, X. Su, X. Huang, and Z. Jiang. 2018. 'Manganese Increases the Sensitivity of the cGAS-STING Pathway for Double-Stranded DNA and Is Required for the Host Defense against DNA Viruses', *Immunity*, 48: 675-87 e7.

Wang, C., M. Sinn, J. Stifel, A. C. Heiler, A. Sommershof, and J. S. Hartig. 2017. 'Synthesis of All Possible Canonical (3'-5'-Linked) Cyclic Dinucleotides and Evaluation of Riboswitch Interactions and Immune-Stimulatory Effects', *J Am Chem Soc*, 139: 16154-60.

Wang, Q., L. Huang, Z. Hong, Z. Lv, Z. Mao, Y. Tang, X. Kong, S. Li, Y. Cui, H. Liu, L. Zhang, X. Zhang, L. Jiang, C. Wang, and Q. Zhou. 2017. 'The E3 ubiquitin ligase RNF185 facilitates the cGAS-mediated innate immune response', *PLoS Pathog*, 13: e1006264.

Wang, Y., X. Ning, P. Gao, S. Wu, M. Sha, M. Lv, X. Zhou, J. Gao, R. Fang, G. Meng, X. Su, and Z. Jiang. 2017. 'Inflammasome Activation Triggers Caspase-1-Mediated Cleavage of cGAS to Regulate Responses to DNA Virus Infection', *Immunity*, 46: 393-404.

West, A. P., W. Khoury-Hanold, M. Staron, M. C. Tal, C. M. Pineda, S. M. Lang, M. Bestwick, B. A. Duguay, N. Raimundo, D. A. MacDuff, S. M. Kaech, J. R. Smiley, R. E. Means, A. Iwasaki, and G. S. Shadel. 2015. 'Mitochondrial DNA stress primes the antiviral innate immune response', *Nature*, 520: 553-7.

White, M. J., K. McArthur, D. Metcalf, R. M. Lane, J. C. Cambier, M. J. Herold, M. F. van Delft, S. Bedoui, G. Lessene, M. E. Ritchie, D. C. Huang, and B. T. Kile. 2014. 'Apoptotic caspases suppress mtDNA-induced STING-mediated type I IFN production', *Cell*, 159: 1549-62.

Xia, P., B. Ye, S. Wang, X. Zhu, Y. Du, Z. Xiong, Y. Tian, and Z. Fan. 2016. 'Glutamylation of the DNA sensor cGAS regulates its binding and synthase activity in antiviral immunity', *Nat Immunol*, 17: 369-78.

Yu, Q., Y. V. Katlinskaya, C. J. Carbone, B. Zhao, K. V. Katlinski, H. Zheng, M. Guha, N. Li, Q. Chen, T. Yang, C. J. Lengner, R. A. Greenberg, F. B. Johnson, and S. Y. Fuchs. 2015. 'DNA-damage-induced type I interferon promotes senescence and inhibits stem cell function', *Cell Rep*, 11: 785-97.

Zhang, X., H. Shi, J. Wu, X. Zhang, L. Sun, C. Chen, and Z. J. Chen. 2013. 'Cyclic GMP-AMP containing mixed phosphodiester linkages is an endogenous high-affinity ligand for STING', *Mol Cell*, 51: 226-35.

Zhang, X., J. Wu, F. Du, H. Xu, L. Sun, Z. Chen, C. A. Brautigam, X. Zhang, and Z. J. Chen. 2014. 'The cytosolic DNA sensor cGAS forms an oligomeric complex with DNA and undergoes switch-like conformational changes in the activation loop', *Cell Rep*, 6: 421-30.

Zhou, W., A. T. Whiteley, C. C. de Oliveira Mann, B. R. Morehouse, R. P. Nowak, E. S. Fischer, N. S. Gray, J. J. Mekalanos, and P. J. Kranzusch. 2018. 'Structure of the Human cGAS-DNA Complex Reveals Enhanced Control of Immune Surveillance', *Cell*, 174: 300-11 e11.

Richard Mathew Hooy

Curriculum Vitae

Ph.D. candidate, Chemical-Biology Interface Program
Johns Hopkins University

Tel: (925) 451-2312

Department of Biophysics and Biophysical Chemistry

Email: rhooy1@jhu.edu

616 Wood Basic Science Building
Johns Hopkins School of Medicine
725 N. Wolfe Street
Baltimore, MD 21205

Born February 25th, 1990, Oakland, California

Education

- *Ph.D.*, Chemical Biology, **Johns Hopkins University**, 2012-2018 *(conferral date: May, 2019)*
- *B.S.*, Biological Sciences, **U.C. Irvine**, 2008-2012

Personal Statement and Career Goals

Undergraduate research first sparked my interest in scientific discovery. My research, in the lab of Dr. Gregory A. Weiss, instilled a genuine interest in protein structure and function, while my practical experience with **phage display** brought about a respect for **high-throughput methodology** and **protein engineering.** I joined the **Chemistry-Biology Interface graduate program at Johns Hopkins University** to pursue a deeper understanding of proteins through mechanistic enzymology. My **thesis work**, conducted in the lab of Dr. Jungsan Sohn, focuses on delineating the molecular regulation of **two human enzymes involved in nucleic acid metabolism and stress sensing**, namely **DEAD-box helicase 41 (DDX41) and cyclic GMP-AMP synthase (cGAS)**. I cloned, then expressed and purified recombinant versions of these enzymes from E. *coli* and characterized their interactions with nucleic acids and substrates. I mastered **numerous biophysical techniques**, including small-angle x-ray scattering (SAXS), analytical ultracentrifugation (AUC), circular dichroism (CD), Förster-resonance energy transfer (FRET) and fluorescence anisotropy (FA). I also **developed multiple, quantitative assays** that monitored helicase activity, ATP transaction, and **most notably, a novel phosphate detection assay that tracks cGAS activity**. More recently, I established multiple **chromatographic methods** (HPLC and FPLC) to fractionate and purify cGAS reaction products. My thesis work engrained a deep appreciation for the rigor of quantitative measurement and the perspective of explaining biology using first principles.

I strive to understand biology with precision and accuracy with the intent of contributing meaningfully towards scientific progress and the improvement of human health. I aspire to lead a multi-disciplinary research program focused on determining molecular mechanisms of signaling regulation. In the long term, my goals as a scientist are to broadly impact pursuits of novel antibiotic development and to define immunological determinants of cancer and pathogen detection. My training in biochemistry and biophysics and education in chemical biology position me to discover and innovate at the highest level.

Research Experience

2012-present *Ph.D. Student* with Professor Jungsan Sohn, Johns Hopkins, School of Medicine, Baltimore, MD

2010-2012 *Undergraduate Researcher* with Professor Gregory A. Weiss, University of California, Irvine, Irvine, CA

CONTRIBUTIONS TO SCIENCE

GRADUATE PUBLICATIONS

7. **Hooy, R.M.**, Massaccesi, G., Rousseau, K., Chattergoon, M., Sohn, J. (2019) Noncanonical activation of cGAS by manganese enables robust DNA length-independent signaling. *In preparation.*

Recent evidence suggests that divalent manganese (Mn^{2+}) enhances the cGAS response to dsDNA in-vitro and in cells, but the mechanism for how this occurs remained unknown. Using biochemical activity assays, I determined that micromolar concentrations of Mn^{2+} enhance the catalytic efficiency of cGAS without reducing its ability to selectively couple ATP and GTP to make cGAMP. Mn^{2+} binding positively couples to dsDNA binding which manifests in reduced DNA-length dependent activity in-vitro and in cells. Finally, millimolar concentrations of Mn^{2+} were discovered to be sufficient to activate monomeric and dimeric cGAS in the absence of dsDNA, illustrating that DNA binding reduces the barrier to Mn^{2+} binding and activation of cGAS. These observations reveal how Mn^{2+} potentiates cGAS activity and stimulates that cGAS senses cytosolic Mn^{2+} as a danger signal in concert with DNA.

6. **Hooy, R.M.** and Sohn, J. (2019) A pyrophosphatase-coupled assay to monitor the NTase activity of cGAS. *In preparation. Methods in Enzymology.*

Although numerous methods have been developed to quantitatively measure cGAS activity, most bear pitfalls that limit their utility, especially in the context of steady state kinetic measurements. To circumvent these challenges, I adopted a pyrophosphatase-coupled assay to directly monitor the activity of cGAS by way of its byproduct, pyrophosphate. Each pyrophosphate released per catalytic event is hydrolyzed by the coupling enzyme enabling facile detection of inorganic phosphate by conventional malachite green-phosphomolybdate chemistry. The assay is inexpensive, reproducible and highly amenable for kinetic measurements of cGAS activity.

5. Jiang, H., Xue, X., Panda, S., Kawale, A., **Hooy, R.M.**, Liang, F., Sohn, J., Sung, P., Gekara, N.O. (2019) The innate immune DNA sensor cGAS is a negative regulator of DNA repair hence promotes genome instability and cell death. *Submitted.*

Although cGAS is thought to localize and function predominantly in the cytosol, this report reveals a new role for cGAS in the nucleus. Nuclear cGAS inhibits homologous recombination by compacting DNA and disrupting RAD51-mediated strand invasion. Importantly cGAS achieves this without invoking canonical activation and signaling via STING. The attenuated capacity for homologous recombinatino promotes DNA damage repair by non-homologous end-joining which potentiates genome instability and cancer. My role in the project was to visualize cGAS-mediated DNA compaction by electron microscopy. I also provided recombinant cGAS to the Sung group for in-vitro strand-invasion assays.

4. **Hooy, R.M.** and Sohn, J. (2018) The allosteric activation of cGAS underpins its dynamic signaling landscape. *eLife*. E39984.

In metazoans, cytoplasmic double-stranded (ds)DNA signals severe maladies ranging from pathogen invasion to dysfunctional mitochondria. cyclic GMP-AMP synthase (cGAS) is the primary initiator of type-I interferons in response to cytoplasmic dsDNA. The mechanism by which dsDNA activates cGAS, and how the length of dsDNA tunes cGAS activity levels remained unclear. Using solution-based biophysical techniques, I found that human cGAS can dimerize in the absence of dsDNA or substrate. I then showed that dsDNA and substrate are both capable of manipulating the fraction of dimeric cGAS. Importantly, the length of dsDNA dictated the fraction of dsDNA-bound cGAS dimers, e.g. the state of cGAS that is catalytically active. Through a novel biochemical activity assay, I determined that cGAS activity levels are thermodynamically linked to dsDNA-length dependent binding and substrate transaction. My data supports a model whereby dsDNA length and cellular context (cGAS expression levels, substrate concentrations and dsDNA levels) dynamically tune the signaling activity of cGAS.

3. Morrone, S.R., Wang, T., Constantoulakis, L.M., **Hooy, R.M.**, Delannoy, M.J., Sohn, J. (2014) Cooperative assembly of IFI16 filaments on dsDNA provides insights into host defense strategy. *Proc Natl Acad Sci USA*. **111**: E62-71.

IFI16, a pattern recognition receptor of the innate immune system, senses foreign dsDNA in the nucleus of mammalian cells. This study demonstrated how IFI16 potentially discriminates between self and nonself dsDNA. My role was to quantify differences in IFI16 binding affinity for different lengths of dsDNA. IFI16 bound more tightly to longer dsDNA, which supported a model whereby the length of dsDNA dictated whether IFI16 formed a filamentous signaling platform.

2. Wang. Z., Raines, L.L., **Hooy, R.M.**, Roberson, H., Leahy, D.J., Cole, P.A. (2013) Tyrosine phosphorylation of mig6 reduces its inhibition of the epidermal growth factor receptor. *ACS Chem Biol*. **8**: 2372-2376.

EGFR, a cell-surface receptor tyrosine kinase, promotes cell survival and growth, and, in its oncogenic form, is causally-linked to the progression of cancer. Regulation of EGFR signaling activity is achieved through multiple mechanisms including through the downstream signaling protein, MIG-6. For this study, I synthesized a phosphorylated version of MIG-6 via solid-phase peptide synthesis and expressed protein ligation, and tested its inhibition of the kinase activity of EGFR^{kinase}. Phosphorylated MIG-6 more weakly inhibited EGFR^{kinase} activity relative to its unmodified form suggesting its phospho-state is linked to feedback regulation of EGFR signaling.

UNDERGRADUATE PUBLICATIONS

1. Vithayathil R, **Hooy RM**, Cocco MJ, Weiss GA. (2011) The scope of phage display for membrane proteins. *J Mol Biol.* **414**: 499-510.

The goal of this study was to determine which, if any, membrane protein archetypes (integral, multi-pass, β-barrel, peripheral) could be functionally reconstituted on the surface of bacteriophage as genetic fusions to phage coat proteins. I demonstrated that a 22-strand, β-barrel, ShuA, could be successfully displayed on the surface of phage, and that this protein retained its native ability to bind heme in this context.

MENTORING

Year	Program	Student
Fall, 2014	Graduate student (Chemistry-Biology Interface Program)	Zach Mazanek
Winter, 2014	Undergraduate (Johns Hopkins Underrepresented in Medical Professions Program)	Esteban Urias
Summer, 2016	Undergraduate (Johns Hopkins Underrepresented in Medical Professions Program)	Alina Corona
Fall, 2017	Graduate student (Biochemistry, Cellular and Molecular Biology Program	Claudia Carcamo
Winter, 2017	Undergraduate (Johns Hopkins University)	Josh Garza
Spring, 2018	Graduate student (Chemistry-Biology Interface Program)	Katherine Miller
Summer, 2018	Undergraduate (Johns Hopkins Underrepresented in Medical Professions Program)	Ryan Porell

PROFESSIONAL DEVELOPMENT

2018 (November)	Reviewer, mock F31 review panel; reviewed and scored multiple F31 applications; presented/defended applications at mock review panel (panel comprised 11 professors from various JHU departments, and myself)
2013 - present;	Mentor, Biophysics Research for Baltimore Teens (BRBT)

PRESENTATIONS

Hooy RM and Sohn J. Defining how DDX41 can be an RNA helicase and a foreign DNA sensor. Frontiers in Chemistry and Biology Interface Symposium. Johns Hopkins University. May 14th, 2016

Hooy, RM and Sohn J. Human cGAS couples dimerization to catalytic activity to produce graded responses to dsDNA. Biophysical Society Meeting, San Francisco, CA, February 18th-21st, 2018.

Awards

2011;	Allergan Undergraduate Research Fellow
2011;	Undergraduate Research Opportunity Fellowship, University of California, Irvine
2010;	Undergraduate Research Opportunity Fellowship, University of California, Irvine

Memberships

2016- present;	Biophysical Society

REFERENCES

Dr. Jungsan Sohn (jsohn@jhmi.edu)
Assistant Professor, Department of Biophysics and Biophysical Chemistry, Johns Hopkins School of Medicine

Dr. Scott Bailey (scbailey@jhsph.edu)

Associate Professor, Department of Biochemistry and Molecular Biology, Johns Hopkins Bloomberg School of Public Health

Dr. Mario Amzel (mamzel@jhmi.edu)
Professor and Director, Department of Biophysics and Biophysical Chemistry, Johns Hopkins School of Medicine